

A STUDY OF THE GAMMA RADIATION PRODUCED IN THE
ALPHA PARTICLE BOMBARDMENT OF O^{16}

Thesis by
John Davie Pearson

In Partial Fulfillment of the Requirements
for the Degree of
Doctor of Philosophy

California Institute of Technology
Pasadena, California

1963

ACKNOWLEDGEMENTS

It is a pleasure for the author to acknowledge the discussions and encouragement offered by Professors T. Lauritsen, W. A. Fowler, C. A. Barnes, and R. W. Kavanagh during the course of this experiment. He is particularly indebted to Dr. R. H. Spear of the University of Melbourne, Australia, whose collaboration made this experiment possible, and to J. D. Larson for assistance with the experimental apparatus. The author also wishes to express his appreciation to Professors A. Bohr, B. Mottelson, and R. F. Christy for their advice on the theoretical considerations.

The research was assisted by the joint program of the Office of Naval Research and the U. S. Atomic Energy Commission.

ABSTRACT

This thesis describes an investigation of gamma rays from the reaction $O^{16}(\alpha, \gamma)Ne^{20}$. The excitation function for gamma radiation has been studied for laboratory alpha-particle energies E_{α} from 4.8 to 9.9 Mev. Resonances were observed at $E_{\alpha} = 5.374, 5.94, 6.61, 6.930, 7.94, 8.17, 8.54,$ and 9.40 Mev, corresponding to Ne^{20} states at excitation energies of 9.029, 9.48, 10.02, 10.270, 11.08, 11.27, 11.56, and 12.25 Mev. Gamma-ray angular distribution measurements establish spins and parities of $4^{+}, 2^{+},$ and 4^{+} for the 9.029-, 10.270-, and 11.08-Mev states respectively. The 2^{+} assignment for the 10.270-Mev state is supported by the results of triple angular-correlation studies made on the gamma-ray cascade from this state. Decay schemes have been investigated and estimates made of radiative widths and total widths. It is concluded that the 10.270-Mev state is the first $T = 1$ state of Ne^{20} on the basis of measurements of its excitation energy, spin and parity, total width, and M1 radiative width. The excitation function for 6.13-Mev gamma rays from the reaction $O^{16}(\alpha, \alpha' \gamma)O^{16}$ has been studied for E_{α} from 8.9 to 9.9 Mev. The data indicates a resonance at $E_{\alpha} = 9.57$ Mev corresponding to a state in Ne^{20} at 12.39 Mev. There is some evidence for a weaker resonance at $E_{\alpha} = 9.25$ Mev corresponding to a state at 12.13 Mev.

TABLE OF CONTENTS

PART		PAGE
I	INTRODUCTION	1
II	METHODS AND APPARATUS	4
	Alpha Particle Beams	4
	Target Chambers	4
	Targets	7
	Current Integration	9
	NaI(Tl) Detectors and Associated Electronics	10
	Angular Distribution Equipment	12
	NaI(Tl) Detector Efficiencies and Standard Spectra	16
III	RESULTS	23
	Excitation Function	23
	5.37-Mev Resonance	28
	6.93-Mev Resonance	36
	7.94-Mev Resonance	53
	Other Resonances	66
IV	SUMMARY	79
APPENDIX A. Angular Distribution Considerations		83
APPENDIX B. A Comparison of the F^{20} Ground State β - Decay and the $M1$ γ -Decay of the 10.27-Mev Level in Ne^{20}		94
TABLES		122
REFERENCES		125
FIGURES		130

I. INTRODUCTION

At the time work was commenced on this experiment, information about the energy levels of Ne^{20} in the energy range 9.5 to 11 Mev was practically non-existent. With the development of the 10-Mev tandem Van de Graaff, this region of excitation energy in Ne^{20} became accessible to the close scrutiny that is possible with this type of accelerator. Interest in this energy region stems in part from the fact that the first $T = 1$ level in Ne^{20} , the analog of the F^{20} and Na^{20} ground states, is expected in this region (1). Shortly after the experiment was started, Litherland et al. (2) showed it was possible to group the low-lying states of Ne^{20} into rotational bands. The possibility that higher excited states would be members of these rotational bands gave additional impetus to the experimental work. The general properties of excited states of Ne^{20} are also of astrophysical significance due to the possible role played by this nucleus in the formation of heavier elements in stellar evolution (3).

The technique used in this experiment involves the measurement of gamma-ray transitions in Ne^{20} following the alpha-capture reaction in O^{16} . A rather special group of levels is selected in this fashion. The reaction, which involves a spin zero projectile and a spin zero target nucleus, populates only levels belonging to the natural parity sequence: 0^+ , 1^- , 2^+ , etc. An "after the fact" analysis of the experimental method shows that of the levels above, only those levels that emit gamma rays with energies above 6 Mev were detectable above the background of other reactions. In spite of these limitations, the

technique has been fruitful. Eight resonances have been found in the yield of the capture radiation, and at least one resonance has been found in the inelastic scattering of alpha particles that leave O^{16} in its 6.13-Mev, 3^- second excited state.

Furthermore the high energy gamma-ray transitions that are easily observed in this experiment terminate on low-lying excited states of Ne^{20} with known spins and parities. With the zero channel spin in the entrance channel and a known final state, measurements of a gamma-ray angular distribution can in principle lead to the spin and parity assignment of the initial state, and give the type of gamma-ray multipolarity. Furthermore in the light self-conjugate nuclei (nuclei for which $Z = N$), such as Ne^{20} , a special set of isotopic spin selection rules influences the strength of dipole transitions. For both electric dipole $E1$, and magnetic dipole $M1$ radiation, these rules imply that the stronger transitions can occur only between levels which differ by one unit in the isotopic spin, or simply $\Delta T = 1$. Hence measurement of the radiative width, or strength of a dipole transition can lead to an isotopic spin assignment. The identification and strength measurements of electric quadrupole radiation ($E2$) can also supply useful information about the structure of a nucleus. Litherland et al. used the fact that the first three levels of Ne^{20} were connected by very strong $E2$ transitions as confirming evidence that these levels form a rotational band. While it has not been possible to reach such conclusions from information gained about $E2$ transitions in this experiment, many of these transitions exhibit radiative widths in excess of what would be

calculated on the basis of a simple, single-particle model.

The properties of the gamma rays from one of the eight resonances allowed the identification of a previously unreported level at 10.270-Mev excitation energy as the first $T = 1$ level in Ne^{20} . Precise determination of the resonance energy for the capture reaction as 6.930-Mev located the resonance within 50 kev of the estimated position of the first $T = 1$ level. Angular distribution measurements show the level has spin and parity 2^+ , and the decay is predominantly M1. Measurements of the radiative width for the dipole transition showed that an isotopic spin change is involved.

Attempts to measure the alpha-capture reaction by O^{16} are faced with the experimental difficulty of small cross sections. For this reason, only the three stronger of the eight capture resonances have been investigated in detail, and even for these strong resonances occasionally it has been found necessary to compromise good experimental technique for counting rate. Furthermore the slightest impurity of an element with reactions of the type: alpha particle in, light particle out, followed by a gamma ray, can be a serious source of background in these measurements.

This thesis contains two main parts: the first part describes the experimental apparatus, the second part is a presentation and discussion of the results. In the second section, the three resonances which have received more attention are described in detail.

For easy reference, figure 1 displays a copy of the energy level diagram for Ne^{20} from Lauritsen and Ajzenberg-Selove (4).

II. METHODS AND APPARATUS

ALPHA-PARTICLE BEAMS

The high energy ion beams used as a source of projectiles in this experiment have been obtained from the Office of Naval Research tandem Van de Graaff accelerator. This machine was obtained from the High Voltage Engineering Co. and is described thoroughly in the literature (5-10). In particular the alpha-particle beams used in this experiment were obtained by stripping a He^0 beam at the high voltage terminal of the accelerator. The formation and injection of this He^0 beam is described by Rose et al. (8), and involves neutralizing the He^+ beam from a small Van de Graaff accelerator. The high energy helium ion beams available at the target after magnetic analysis were He^+ with currents up to $3.2 \mu\text{a}$ and energies up to 5.4 Mev, and He^{++} with currents up to $1.3 \mu\text{a}$ and energies up to 10 Mev.

TARGET CHAMBERS

Three target chambers were used during the course of the experiment. The original target chamber arrangement is shown in figure 2. An adjustable bellows preceding the slit system made it possible to place the target chamber on the beam axis. The slits were then adjusted to give a beam spot of approximately $3/16'' \times 3/16''$ as viewed on the quartz in the target chamber. Additional pumping of roughly 90 l/sec was provided by the charcoal trap cooled to liquid nitrogen temperatures. The pressures thus obtained were $2 - 4 \times 10^{-6}$ Torr. at the Penning gauge.

Difficulty was experienced in maintaining a constant beam spot

size on the target. This stemmed in part from the poor angular resolution afforded by the short distance between pairs of slits, and in part from placing the target chamber only 8 ft from the target quadrupole magnetic lens which results in a rapidly diverging beam.

Even though the problem with the beam size could be overcome, the most serious difficulty with this target chamber was carbon build-up on the target during bombardment. The alpha-particle reactions on carbon are listed below (4):

<u>Reaction</u>	<u>Threshold</u>	<u>Excitation energy in Ne²⁰ at threshold</u>
$C^{13}(\alpha, n)O^{16}$	0 Mev	4.73 Mev
$C^{13}(\alpha, n\gamma_{6.13})O^{16}$	5.11	8.82
$C^{13}(\alpha, n\gamma_{6.92})O^{16}$	6.15	9.64
$C^{13}(\alpha, n\gamma_{7.12})O^{16}$	6.40	9.84
$C^{12}(\alpha, \alpha\gamma_{4.43})O^{16}$	5.91	9.46

The last column gives the excitation energy in Ne²⁰ obtained by bombarding O¹⁶ with alpha particles of the threshold energy. As seen in this table, gamma rays from the C¹³ + α reactions have energies close to those of gamma ray transitions in Ne²⁰ to the ground state and first excited state, and therefore C¹³ on the target is a serious source of background. Direct interference with the measurements made in this experiment occurs at higher energies when the 6.13-Mev radiation from C¹³(α, nγ)O¹⁶ is the same as produced in the inelastic scattering from O¹⁶.

The target chamber designed to reduce the problems experienced

with the first target chamber is shown in figure 3. Several features in the "clean system" significantly reduced the carbon build-up on the target. The influx of oil vapors from the low vacuum side is reduced by the 12" in-line cold trap. The 3/8" diameter beam tube of this trap offers sufficient resistance so that the 9 l/sec titanium-getter ion pump is able to reduce the pressure in the target chamber. Demountable vacuum seals are made with "viton" compound "O" rings without lubrication. Pressures as low as 2×10^{-8} Torr. have been obtained at the pump after an outgassing procedure during which the target chamber and pump assembly were heated to 100°C for 30 minutes. Typical pressures obtained with the beam on the target were 1×10^{-7} Torr. A comparison of the carbon deposit on targets during bombardment in this system with that in the original system indicates that the quantity of carbon deposited is proportional to the pressure in the target chamber times the total charge deposited by the beam.

Since a loss or gain of electrons by the target interferes with accurate beam-current measurements, these phenomena are avoided by maintaining the target at +300 volts with a nearby Faraday ring around the beam path at -300 volts. This arrangement was used in the target chamber illustrated in figure 3. Tests of the charge collection efficiency showed that it was necessary to put the target at ground potential and run the Faraday ring at +300 volts before the counts per fixed charge dropped to half the value obtained by the usual potential arrangement.

By placing the target chamber 26.5 ft from the target quadrupole

lens, and by using a larger slit system, the beam size definition was improved. Micrometers on this new slit system allowed reproducible slit settings.

The most serious fault with this system has been the difficulties experienced with the un-lubricated viton "O" rings. For example, the target rod and quartz rod can be moved only after the lid screws have been loosened. Sliding these rods over the un-lubricated "O" rings eventually destroys the "O" ring. Furthermore, with the lid screw loosened, these seals leak. The strong magnet on the ion pump required the magnetic shielding shown in figure 3. Tests on the effectiveness of this shielding are described in "Angular Distribution Equipment" in this section.

In order to check the alpha-capture cross sections obtained from metallic oxide targets, the yield of gamma rays from one resonance was studied by bombarding ice targets in the special target chamber shown in figure 4. Thin ice targets were manufactured by closing the valve to the vacuum system and either warming up the water vial or by allowing both the target rod and water vial to come to room temperature and then cooling both simultaneously.

TARGETS

The targets used in this investigation were primarily metallic oxide targets of tantalum and tungsten. One resonance was studied using ice targets, and the method of manufacture of these ice targets is given in the previous section.

The tungsten oxide targets were obtained from Mr. J. Domingo of this laboratory who produced them by radio-frequency heating of a tungsten blank in an atmosphere of oxygen depleted in O^{18} . While the reduction by a factor of 2.5 in the O^{18} content was beneficial in reducing the number of low energy gamma rays and the neutron continuum observed in the NaI(Tl) detector, these targets had a considerable amount of carbon contamination. Carbon contamination is judged as "serious" in this experiment when the yield of the 6.13-Mev radiation from the $C^{13}(\alpha, n\gamma)O^{16}$ reaction equals the yield of the 8.64-Mev gamma ray from the 6.93-Mev resonance in $O^{16}(\alpha, \gamma)Ne^{20}$. From the known cross sections (11), "serious" contamination amounts to 4.5×10^{16} carbon atoms per cm^2 , or roughly a layer 33 atoms thick. By elastic scattering of protons, Domingo finds $WO_{2.6}$ is the composition of the front surface of the targets with an uncertainty of 10% on the oxygen content. This composition is roughly that of the blue oxide of tungsten, W_4O_{11} (12). However in view of the method of manufacture, the measured atomic ratio, $O/W = 2.6$, is probably more reliable, and this number is used in the calculations of the radiative widths.

The tantalum oxide targets were made by anodizing tantalum in a 3% dibasic ammonium citrate solution. The apparatus used for this process is illustrated schematically in figure 5. The 250 volt power supply and the $10\ k\Omega$ resistor act as a constant current supply which steadily increases the voltage across the growing oxide layer. The smooth increase in voltage is vital since it allows the metal at the edge of the fluid meniscus time to anodize before the meniscus is drawn

over this point by the increasing voltage. Step increases in the voltage across the oxide layer often lead to spark break downs in this vicinity making the sample useless for further anodizing. The voltage drop across the high resistance of the oxide layer can be related to the thickness of the layer, and for a variety of electrolytes the thickness is 15 to 16 Å/volt at 0.1 ma/cm² current density (13). Thicknesses from the interference colors are given by Charlesby et al. (14). The composition of the oxide layer is given by Vermilyea (13) as anhydrous, amorphous Ta₂O₅. The cleanest anodized targets were made from 0.00025" tantalum suture foils obtained from the Ethicon Suture Laboratories. A newly anodized foil put through the "out-gassing" procedure in the clean vacuum system would show no signs of the 6.13-Mev radiation from C¹³(α, nγ)O¹⁶.

CURRENT INTEGRATION

The current collected from the target was integrated with an Eldorado model CI-110 current integrator. A bombardment continued until a predetermined charge had been collected from the target. The value of the charge used in the calculation of the radiative widths was taken as the number indicated by this instrument. Some 29 separate calibrations of the integrator over a period of a year indicate the root-mean-square deviation from the charge indicated and the actual charge is 0.53%. The largest deviation noted was 1.3%. To allow for possible uncertainties in the calibration procedure as well as the possible error in the total charge, a 1% uncertainty has been assigned to the charge

measurement used in the calculation of radiative widths.

NaI(Tl) DETECTORS AND ASSOCIATED ELECTRONICS

The majority of the experimental work has been done with a 4" x 4" NaI(Tl) scintillation spectrometer discussed by Kavanagh (15). Minor changes have been made; a 5" CBS 7819 photomultiplier has been used instead of the equivalent DuMont 6364, and a semi-permanent optical connection between the crystal and photomultiplier has been obtained by the use of a clear silicone gel (Dow Corning QC-2-0057) instead of the high viscosity silicone fluid described by Kavanagh. Occasionally other NaI(Tl) crystals were used. These were a 3" x 3" NaI mounted on a DuMont 6363 photomultiplier, and a 2" x 2" NaI mounted on a RCA 6342-A photomultiplier. Both of these scintillation spectrometers are from the Harshaw "Integral Line" series.

The electronics following the NaI(Tl) detector consisted of an integrating type preamplifier, a Hamner model N328 pulse amplifier with double delay-line clipping, and a Radiation Instrument Development Laboratory model 34-12 400 channel pulse-height analyzer. The linearity of the system was judged to be 0.5% or better, and the gain at a fixed counting rate has been found to be constant to one part in 900 over a period of 40 minutes (see the discussion of "Angular Distribution Equipment" in this section). The 5" CBS 7819 exhibits characteristic gain changes with large changes in the counting rates (16), however such gain changes are of no significance for the low counting rates experienced in this experiment.

Coincidence studies were performed with a fast-slow coincidence system shown in figure 6. Signals accurately defined in time were derived from the zero crossing of the pulse from the Hamner amplifier by the pick-off circuit shown in figure 7. Fast coincidences were detected by a three tunnel diode coincidence mixer designed in this laboratory by R. W. Kavanagh. Outputs from the integral discriminators of the Hamner amplifiers and the output of the fast coincidence mixer were fed to a slow coincidence mixer, which generates an output pulse for a triple coincidence between the inputs, and a pulse for a double coincidence between the fast coincidence mixer input and either of the other two inputs.

Due to the low counting rate, it was desirable to save both the singles spectrum and the coincidence spectrum from one of the counters during a run, by storing the singles spectrum in the first half of the 400 channel analyzer memory and "shifting" to the second half for coincidence pulses. The shifting was performed by resetting the address converters of the analyzer to 200 instead of 0 with a pulse from the two transistor "and gate" shown in figure 6. This pulse was generated by the last part of the reset pulse for the address converters and a pulse from the triple coincidence mixer. Usually the shifting of the coincidence pulses from one detector was done with the requirement that there had been a double coincidence between the fast coincidence mixer and the integral discriminator of the amplifier for the other detector.

ANGULAR DISTRIBUTION EQUIPMENT

The angular distribution table used in conjunction with the clean target chamber is a circular steel table, 4 ft in diameter and standing 55" high, equipped with two carts for carrying NaI(Tl) detectors and their associated lead shielding about its center. The 4" x 4" NaI(Tl) scintillation spectrometer shielding is equipped with wheels and travels along the top of one of the carts between two rails, thus allowing for adjustment of the target-detector distance.

The target chamber, in-line cold trap, and angular distribution table were aligned with respect to the beam axis by a telescope and two reference points that had been established previously. Alignment of the heavy steel table is best approached through successive approximations where the table is first leveled, placed under the beam axis, releveled, and so forth. Unfortunately the glass target chambers are usually skewed, and the final alignment of the target chamber was made by compromising the alignment of the in-line cold trap.

The beam was centered in the target chamber with the aid of the quartz shown in figure 3. The requirement that the beam should not hit the 3/8" beam tube of the in-line cold trap was met by shadowing the beam tube on the quartz and adjusting the slits preceding the cold trap so that the beam was confined within this circle. It was found that this minimum requirement was insufficient to keep the beam spot size from changing as the target quadrupole magnet was varied. Consequently during angular distribution runs, the slits were decreased 100 mils from the settings used for maximum beam. The beam spot size thus obtained was approximately 3/32" x 3/32".

To enhance the angular resolution of the 4" x 4" NaI(Tl) crystal, a 1-5/8" thick lead collimator with a 1-1/2" diameter hole was placed immediately in front of the NaI crystal. The principal effect of this collimator was to keep the gamma rays out of the edges of the crystal. For a typical geometry where the collimator face was 0.85" from the target, Rose's (17) smoothing factors for the collimator and crystal arrangement were ~ 86% for $P_2(\cos \theta)$ and ~ 66% for $P_4(\cos \theta)$ for gamma-ray energies in the 4 to 8 Mev range. These numbers are within a few per cent of the averages of $P_2(\cos \theta)$ and $P_4(\cos \theta)$ over the hole of the collimator. A further discussion of smoothing factors is given in Appendix A.

Several tests were necessary to prove the angular distribution apparatus. Gain changes induced in the photomultiplier by a magnetic field would pose a serious problem in an angular distribution study. Although the 9 lb Alnico magnet of the ion pump was shielded by a series of three mild steel cans shown in figure 3 it was still possible to demonstrate the presence of a magnetic field with a compass. It was hoped that the magnetic shield provided in the photomultiplier mount would be sufficient for the final reduction of this field.

The effectiveness of the magnetic shielding was determined by measuring the gain change of the system as a function of detector angle. The gain change was measured by monitoring the counts from a differential discriminator set on the falling, high energy edge of a gamma-ray full-energy peak. For these measurements, the 2.615-Mev gamma rays from a ThB source were used. The source was attached to the NaI

mount approximately eight hours before use, allowing sufficient time for the photomultiplier gain to reach equilibrium (16), and proper aging of the source.

The gain change may be computed from

$$\frac{\Delta N}{N} = - 2 \frac{S}{W} \left(\frac{n_1 - n_2}{n_1 + n_2} \right)$$

where

N = average number of counts per run

ΔN = deviation from average counts

S = gain change

W = window width

n_1 = counting rate at the low energy side of the window

n_2 = counting rate at the high energy side of the window.

In such a measurement it is convenient to use a multichannel analyzer, in which case

S = gain change in channels

W = window width in channels.

The quantity in parentheses can be derived from a spectrum, and is independent of running time. With a width of 4 channels, centered around channel 100, the sensitivity of a typical run was limited by statistics to changes larger than 3×10^{-2} channels per 100. However random gain changes in the electronics over a period of 40 minutes needed to complete a run amounted to 11×10^{-2} channels per 100, thus providing the basic limitation of the technique. The results of these investigations, corrected for the 10-1/2 hr half-life of the source are presented in figure 8. The gain change, if any, is smaller than 0.1

channels per 100 for a -90° to $+90^{\circ}$ rotation of the NaI detector around the beam direction. In view of other uncertainties in the angular distribution data, this gain change is negligible.

Tests for possible beam misalignment, and other built-in anisotropies in the angular distribution apparatus were made by measuring the angular distribution of the isotropic 3.56-Mev gamma ray produced in the $\text{Be}^9(p, \alpha)\text{Li}^6$ reaction at 2.56 Mev bombarding energy (18). This reaction proceeds from the 2^+ , $T = 1$ level in B^{10} at 8.89 Mev by alpha decay to the 0^+ , $T = 1$, second excited state of Li^6 at 3.56 Mev (19).

A target of 0.05 mil Be foil mounted over a $3/8$ " hole punched in a 10.2 mil piece of tantalum and backed up by another piece of 10.2 mil tantalum in the form of a sandwich was mounted in the clean target chamber and bombarded by protons. The excitation function for gamma rays in the energy range 2.90 to 3.62 Mev is shown in figure 8-B. It is very interesting to note that the value for the resonance energy, $E_r = 2,566$ kev, obtained from the data of this figure by assuming a resonance width of $\Gamma = 40$ kev is surprisingly close to the accepted value of $E_r = 2,562 \pm 4$ kev (19) in view of the fact that no effort was made to obtain precise energy definition of the beam.

A representative angular distribution for the 3.56-Mev gamma ray is shown in figure 8-C. The data, corrected for target absorption ($\sim +2\%$) and background ($\sim -5\%$), has been normalized to unity at 0° . The straight line is the expected behavior for a point source displaced towards the north (the 90° point) from the center of the angular

distribution table by 44 mils.

The final test of the angular distribution apparatus was the experimental determination of a known angular distribution. The results are described in the section on the 5.37-Mev resonance in "Results."

NaI(Tl) DETECTOR EFFICIENCIES AND STANDARD SPECTRA

NaI efficiencies have been calculated after the method of Lazar et al. (20) using the tabulated cross sections (21) for gamma-ray absorption, Compton scattering, and pair production. Calculations similar to those for the NaI efficiency yield the smoothing factors of Rose (17), which are necessary for correcting gamma-ray yields and angular distributions for the finite size of the NaI(Tl) detector. A further discussion of the smoothing factors is given in this section under "Angular Distribution Equipment" and in Appendix A. The calculations have been programmed for the Burroughs computer by Mr. J. D. Larson.

The cross sections used in the efficiency calculations are those that give the initial probability of a gamma-ray interaction in the crystal. The shape of the observed gamma-ray spectra depends on subsequent interactions which are not directly calculable. Since gamma rays observed in the $O^{16}(\alpha, \gamma)Ne^{20}$ reaction are partially obscured by other gamma-rays, it is necessary to relate the counts observed in a fraction of the spectrum to the total number detected by the NaI. This has been done with the aid of gamma-ray spectra obtained from reactions that produce single, or very nearly single, gamma-ray lines.

These "standard spectra" were obtained for gamma-ray energies

of 4.43 Mev, 6.13 Mev, 7.48 Mev and 9.17 Mev, for the variety of distances and collimator configurations used in the $O^{16}(\alpha, \gamma)Ne^{20}$ experiment. Reactions used to produce these lines were resonances in $N^{15}(p, \alpha\gamma)C^{12}$ at 898 kev proton bombarding energy, $F^{19}(p, \alpha\gamma)O^{16}$ at 597 kev, $Be^9(p, \gamma)B^{10}$ at 991 kev, and $C^{13}(p, \gamma)N^{14}$ at 1747 kev respectively. The last two reactions have weak cascade radiations. The 7.48 Mev gamma-ray spectra have been corrected for a 3.1% contribution for cascades in B^{10} to the 2.17 Mev level (22). The 9.17 Mev spectra have been corrected for 10.1% cascade through the 6.44 Mev level in N^{14} (19). A typical standard spectrum for a 6.13 Mev gamma ray is shown in figure 9.

The shape of the low energy tail of the standard spectra has been obtained by two methods of extrapolation. The first method is a horizontal extrapolation based on the calculated shape of the Compton electron energy spectra (23). The second method is based on the techniques of Zerby and Moran (24), who have made Monte Carlo calculations on gamma-ray shapes. They argue that the counts in the first channel of the spectrum, or the "zero energy intercept," are due to Compton scattering events resulting in a forward going gamma-ray that has no further interactions in the crystal. For a cylindrically shaped crystal whose axis of symmetry passes through the target, the number of counts in the first channel is given by the integral

$$N_0 = \frac{N}{2} \Delta E \int_{\text{crystal}} \frac{2\pi R_0^2 m_0 c^2 D}{E^2} l(\theta) e^{-\mu l(\theta)} \sin \theta d\theta$$

where

N_0 = counts in the first channel

N = source strength

ΔE = energy width of the first channel

E = gamma-ray energy

R_0 = classical electron radius

$m_0 c^2$ = electron rest mass

D = electron density in NaI

$l(\theta)$ = path length at angle θ in the crystal

μ = linear attenuation coefficient for the gamma ray
in NaI,

and where the angle θ is the angle between the gamma ray direction and the axis of symmetry. The integrations have been performed with the aid of the Burroughs 220.

The calculated spectral shapes obtained by Zerby and Moran fit the experimental spectra for gamma-ray energies of 1 Mev or less. For the higher gamma-ray energies of interest in this experiment, the fits in the low energy part of the spectra are not as good. This discrepancy they explain as due to a background from gamma-ray back scattering, pair production in the lead shielding for the NaI crystal, true room background, and so forth. While such phenomena are indeed taking place, experience seems to indicate (25) that the zero intercept value is too low.

Similar arguments can be advanced against the validity of the horizontal extrapolation of the low energy tail. For the high energy gamma-rays, there is a definite, downward slope in the spectra. This slope can be seen in the spectrum of the 6.13-Mev gamma-ray shown

in figure 9. Due to these uncertainties, both methods of extrapolation have been carried through, the number of counts in the spectrum has been taken as the average of the two estimates, and an uncertainty has been assigned that encompasses both possibilities. Both methods of extrapolation are illustrated in figure 9, and the difference in the total number of counts is 5%.

CALIBRATIONS

The 90° beam-analyzing magnet is a 34" radius, uniform field device with focussing, corrected to the second order, in the horizontal median plane. The magnetic field is determined from the nuclear magnetic resonance frequency of a proton sample placed close to the beam path in the magnet.

The beam position in the magnet is defined by two slits placed 34.5" from the entrance and exit pole faces, at conjugate focal points of the magnet. This arrangement of slits has the property that the momentum resolution is independent of the entrance angle. For a beam of no lateral extent, the momentum resolution is given by:

$$\frac{\Delta P}{P} = \pm \frac{S_1 + S_2}{4R}$$

where

P = average momentum

ΔP = momentum deviation (maximum)

S₁ = entrance slit width

S₂ = exit slit width

R = magnet radius = 34"

To restrict the possible orbits in the 90° analyzing magnet, a third slit was installed 36" from the exit slit and immediately preceding the switching magnet. The maximum deviation within the magnet from the central ray is given by the smaller of

$$d \approx \pm \frac{1}{2} \left[(S_2 + S_3)^2 + (2S_2 + S_3)^2 \right]^{1/2}$$

$$d = \pm \frac{W}{2}$$

where

d = maximum deviation from central ray

S_3 = switching magnet slit width

W = vacuum box width = 1-1/4"

In the first equation, the distance between the exit and switching magnet slits has been approximated by 34".

This extra slit also provides a possible improvement in the momentum resolution of the system, and the resolution is now given by the smaller of the values

$$\frac{\Delta P}{P} = \pm \frac{S_1 + S_2}{4R}$$

$$\frac{\Delta P}{P} \approx \pm \frac{2(S_3 - S_2) + S_1}{6R}$$

In the latter equation, the 36" distance between the exit slit and the switching magnet slit has been approximated by 34". With slit settings of 0.100", 0.050" and 0.100" for the entrance slit, exit slit, and switching magnet slit respectively, the first equation gives $\Delta P/P = \pm 1.09 \times 10^{-3}$, and the second gives $\Delta P/P = \pm 0.97 \times 10^{-3}$.

While this improvement in the resolution is not really significant, the maximum deviation from the central ray has been reduced to $1/8''$.

The calibration points chosen were the $\text{Na}^{23}(\alpha, n)\text{Al}^{26}$ resonance at 3492 ± 3 kev, and the $\text{Al}^{27}(\text{p}, n)\text{Si}^{27}$ threshold at 5798 ± 4 kev. The $\text{Na}^{23}(\alpha, n)\text{Al}^{26}$ resonance energy value is from the compilation of Marion (26), and the $\text{Al}^{27}(\text{p}, n)\text{Si}^{27}$ threshold value is the weighted mean of the values given by Bromley et al. (10).

Thick targets of high purity NaCl evaporated on a tungsten blank and spectroscopic grade aluminum were bombarded with alpha particles and protons respectively. Neutrons were detected by a NE - 402, B^{10} loaded, ZnS scintillator, mounted on a DuMont 6392 photomultiplier, placed $1.78''$ from the target. Counts due to thermal neutrons in the target room were reduced by $1/8''$ thick cadmium shield. Runs were made with and without a $1''$ thick paraffin moderator.

Typical results are given in figure 10. In general it was found that the reproducibility of the measurements for a given arrangement of the controls on the tandem was far better than the estimates of the reproducibility obtained from the slit settings. This is illustrated by runs #2 and #4 on the $\text{Al}^{27}(\text{p}, n)\text{Si}^{27}$ threshold made January 12. However the reproducibility of the measurements after the beam controls had been changed was not quite as good. This fact is illustrated by the comparison of run #1 made on January 16 with the runs made earlier on the $\text{Al}^{27}(\text{p}, n)\text{Si}^{27}$ threshold. Similar results have been observed with the $\text{Na}^{23}(\alpha, n)\text{Al}^{26}$ resonance. A summary of the values for the magnet constant defined according to the equation

$$E \left(1 + \frac{E}{2E_0} \right) = K \frac{f^2 e^2}{M^2}$$

where

K = magnet calibration constant

E = beam energy in Mev

E_0 = rest mass energy of the particle in Mev

f = proton resonance frequency in Mc/sec

e = electron charges per particle

M = mass of particle in amu (O^{16})

is plotted at the bottom of figure 10. The uncertainties assigned to each point of the plot are primarily due to the uncertainty of the threshold energy or resonance energy. The weighted mean value of these measurements is $1996.8 \pm 3 \times 10^{-5}$. The uncertainty assigned is roughly twice the standard deviation of the measurements, and is somewhat less than the value (± 4) estimated from the slit settings for a beam of no lateral extent.

Prior to the final $Al^{27}(p,n)Si^{27}$ threshold measurements, runs were made on the $O^{16}(\alpha,\gamma)Ne^{20}$ resonance at 6.93 Mev. The front edge of the thick target yield is also given in figure 10. The resonant energy is 6.930 ± 0.010 Mev. The 1/4 to 3/4 rise of the front edge indicates a total width of 2 or 3 kev. Estimating the beam stability to be 1-2 kev from the reproducibility of the $Al^{27}(p,n)Si^{27}$ threshold measurements, and from the experimental width of the $Na^{23}(\alpha,n)Al^{26}$ resonance whose natural width is less than 1 kev, gives a width for the 6.93 Mev resonance in Ne^{20} of 2 kev or less.

III. RESULTS

EXCITATION FUNCTION

The excitation function for gamma-ray transitions in Ne^{20} to the ground state and first excited state produced in the alpha-capture reaction by O^{16} for alpha-particle energies of 4.8 to 10 Mev is shown in figures 11 and 12. The abscissas of these plots are the alpha-particle bombarding energy, E_α , and the calculated excitation energy in Ne^{20} , E_x , obtained by using the Q value; $\text{O}^{16} + \alpha - \text{Ne}^{20} = 4.730 \text{ Mev}$ (24). The ordinate is the number of counts, N, falling in channels of the spectra obtained from the 400 channel analyzer that correspond to the energy range; $0.86(E_x - 1.63) \text{ Mev}$ to $1.10 E_x \text{ Mev}$, for a fixed integration of the beam current. This variable energy window includes the full energy peak and the two escape peaks of ground state gamma-ray transitions, as well as the full energy peak, the first escape peak, and roughly half of the second escape peak of gamma-ray transitions to the first excited state. An illustration of the window used at 5.40-Mev bombarding energy is given in figure 13. The gamma ray observed at that energy is the 7.40-Mev transition from a level at 9.029 Mev to the first excited state. The only correction made to the number of counts determined in this fashion was a subtraction of the time dependent room background of approximately 6 counts/min in the window.

In the lower half of the excitation function shown in figure 11, the region has been covered in 20 kev steps or less of the bombarding energy. A target of anodized tantalum foil with an oxide layer 51 kev thick to 7-Mev alpha particles was placed perpendicular to the beam in the clean

vacuum system. The gamma rays were detected by the 4" x 4" NaI(Tl) scintillator placed 1.06" from the target at 0° with respect to the beam axis. The counts in the variable energy window have been normalized to a charge of 300 μC of He^{++} . Resonances in the gamma-ray yield are seen at 5.37-, 5.94-, 6.61-, and 6.93-Mev alpha-particle bombarding energy. A preliminary investigation indicated a weak resonance in the vicinity of 4.95-Mev, but this investigation has not been followed up.

Resonances found in this region of excitation energy in Ne^{20} by elastic scattering of alpha particles on O^{16} are shown by arrows on the top of the page. The set of solid arrows is from the work of McDermott et al. (28), the dotted arrows are from the preliminary work of Davis et al. (29). Except for a discrepancy in energy, which will be discussed later, the resonances at 5.37 and 5.95 Mev correspond to those found by McDermott et al. They have also postulated a broad 4^+ level just beyond their range of 6.5 Mev, which probably is the resonance seen at 6.61 Mev. Corroborating evidence for the existence of the 5.95- and 6.61-Mev resonances is supplied by Davis et al. The resonance at 6.93 Mev with the relatively large radiative width seen in this experiment will be ascribed to the 2^+ , $T = 1$, analog of the F^{20} and Na^{20} ground states. Davis et al. have found a level in this region but it is apparently unrelated to the resonance seen in this experiment.

Six levels seen in this region by elastic scattering of alpha particles on O^{16} are not seen in this work. One of these six, the 5^- at 8.84-Mev excitation energy, has such a high spin that gamma radiation

to the ground state or the first excited state is unlikely. The 0^+ and 2^+ resonances in the vicinity of 5-Mev bombarding energy marked with B's in figure 11 have widths of 800 kev, and gamma rays from these levels would be difficult to observe with targets of thicknesses used in this experiment. The remaining three levels are all odd parity and would have to decay by E1 or M2 radiation to the ground state or 2^+ first excited state to be detected. Since theoretical estimates (30) indicate M2 transitions will have small radiative widths ($\sim 7 \times 10^{-3}$ ev for a 9 Mev M2 transition), it is supposed that the isotopic spin selection rule (31) forbidding E1 transitions between the $T = 0$ levels in question is primarily responsible for the absence of these three resonances.

Other experiments indicate that E1 transitions between the low-lying $T = 0$ levels in Ne^{20} are very slow when compared to the Weisskopf single particle estimate (30). The radiative width for the 3.34-Mev transition (32) between the 2^- , 4.97-Mev level and the 2^+ , 1.63-Mev level has a ratio to this estimate of $|M|^2 = 1.6 \times 10^{-5}$. Toppel et al. (33), who performed the only previous experiment with the $\text{O}^{16}(\alpha, \gamma)\text{Ne}^{20}$ reaction, searched for, but did not find, the 5.54-Mev transition from the 3^- , 7.17-Mev level to the 2^+ , 1.63-Mev level. The limit they set on this transition is $|M|^2 \lesssim 4.3 \times 10^{-5}$. By assuming that a ratio of $|M|^2 \lesssim 5 \times 10^{-5}$ applies to the three missing E1 transitions in question, the estimated radiative widths obtained for these transitions ($\Gamma_\gamma \sim 0.02$ ev) are much smaller than the sensitivity of the experiment.

There are indications of two additional levels in this region of excitation from the (d, n) reaction on F^{19} . Neutrons corresponding to a level at 9.22-Mev excitation energy in Ne^{20} have been seen in a cloud chamber experiment (34), and by a proton-recoil neutron spectrometer (35). Gamma rays with 9.22-Mev energy from the $F^{19}(d, n\gamma)Ne^{20}$ reaction (36) have been attributed to this level. The angular distribution of the neutrons (35) indicate the proton is captured with $l = 1$, giving a sequence of possible spin values of 0^- , 1^- , 2^- for this level. Its absence from this work and the alpha-scattering data would indicate 0^- or 2^- as possible spins. The other level in this region of excitation energy in Ne^{20} indicated by work on the $F^{19}(d, n)Ne^{20}$ reaction is in the vicinity of 10 Mev. Unfortunately the evidence for the position of this resonance is somewhat contradictory.

The upper half of the excitation function is shown in figure 12. The data in this figure was obtained from a tungsten oxide target 55 kev thick to 7-Mev alpha-particles, and has been normalized to an integrated beam current of 150 μC of He^{++} . The NaI(Tl) detector was at 45° to the beam and 1.06" from the target. The region has been covered in 40 kev steps or less. Resonances in the gamma-ray yield are clearly indicated at 7.94-, 8.17-, 8.54-, 9.40-, and 9.57-Mev bombarding energy.

Gamma rays from the first resonance at 7.93 Mev cascade mainly through the 4^+ second excited state of Ne^{20} . Its presence in the excitation function for radiation to the ground state and the first excited state of Ne^{20} is primarily due to summing of the cascade gamma rays

in the NaI crystal. The resonance at 9.57-Mev is primarily due to pulse pile-up from the very strong 6.13-Mev radiation from an inelastic scattering resonance on O^{16} at this energy.

The solid arrows at the top of the diagram indicate levels found in this region of excitation energy in Ne^{20} by the $F^{19}(d, n\gamma)Ne^{20}$ reaction. The first row of arrows is from the work of Butler (37), who used a gamma-ray threshold technique. The second row of arrows represents levels reported by Rabson et al. (36) from gamma rays detected in a pair spectrometer. There is general agreement between this experiment and the $F^{19}(d, n\gamma)Ne^{20}$ experiments on level position and decay schemes of the levels at 11.27- and 12.25-Mev excitation energy. Butler also sees a level near 11.08-Mev, but claims it is due to a gamma-ray transition to the first excited state of Ne^{20} .

The dotted arrows are the continuation of the preliminary results of Davis et al. In general it seems that these two techniques are complementary, for the resonances reported in this work do not show up clearly in the elastic scattering results, the broad resonances (125 to 600 kev) easily found by the elastic scattering of alpha-particles, apparently have small radiative widths for gamma-ray transitions to the ground state and first excited state of Ne^{20} .

In both halves of the excitation function, the resonances are seen to be superimposed on a background of counts. In the region between resonances, the pulse-height spectra usually have some indication of the photo-peaks of the 6.13-Mev radiation from $C^{13}(\alpha, n\gamma)O^{16}$ followed by a smooth decrease in the number of counts towards higher energies with

no signs of gamma rays from Ne^{20} . Figure 16 shows spectra from an on-off resonance sequence.

The sensitivity of the experiment is roughly the height of the background. At 6.0-Mev bombarding energy, this implies that a narrow resonance would need a product $\omega\Gamma_{\gamma} \sim 1.3$ ev to be detected, and at 8.5-Mev bombarding energy a product of $\omega\Gamma_{\gamma} \sim 0.5$ ev would be sufficient. If these hypothetical resonances had total widths of 1 kev, the numbers above would imply cross sections of 0.5 μbarns and 0.12 μbarns respectively.

The next three sections will describe in detail the resonances at 5.37-, 6.93-, and 7.94-Mev bombarding energy. A less detailed description of the remaining resonances will be given at the end of "Results."

5.37-MEV RESONANCE

The detailed studies made on the gamma rays from the 5.37-Mev resonance include a precise determination of the resonance energy, measurements of the gamma-ray angular distributions, and determinations of the radiative width. The original purpose of the angular distribution measurements made on this resonance was to test the ability of the apparatus to resolve a $P_4(\cos \theta)$ term in an angular distribution. The choice of this transition for the test was rather fortunate since precise energy determinations of the resonance energy gave a value 58 kev lower than that obtained by McDermott et al. and without the information from the angular distribution direct comparison of the two experimental results would be difficult.

The capture gamma rays from this resonance result from the 7.40-Mev transition from the corresponding level at 9.029 Mev to the 2^+ , first excited state of Ne^{20} at 1.63 Mev. A spectrum for this gamma

ray along with the cascade scheme is shown in figure 13. The small bump at channel 125 corresponding to the energy of direct transitions to the ground state can be accounted for by summing of the two cascade members in the NaI detector. The dotted curve in figure 13 is from a similar run 100 kev lower in energy. The slightly lower background in the second spectrum is partially due to a decrease of the 6.13-Mev radiation from the $C^{13}(\alpha, n\gamma)O^{16}$ reaction that occurs in going from 5.40 Mev to 5.30 Mev alpha bombarding energy (11).

Precise determinations of the resonant energy were made with slit settings on the analyzing magnet and switching magnet identical to those used during the calibration of the analyzing magnet (see page 20). The excitation functions for the 7.40-Mev gamma ray obtained with the He^+ and He^{++} beams available from the tandem accelerator at this energy are shown in figure 14. Plotted in this figure are the number of counts in the energy window of 6.56 Mev to 8.58 Mev for an integrated beam current of 90 μC as a function of the bombarding energy. The value for the resonant energy as determined from these two excitation functions is 5.372 Mev and 5.378 Mev. Considering other measurements made during the course of the experiment, the best value for the resonant energy is 5374 ± 10 kev, where the uncertainty is primarily due to uncertainties in the value of the magnet calibration constant. Using the Q-value for $O^{16} + \alpha - Ne^{20}$ of 4.730 Mev (27), the excitation energy of the corresponding level in Ne^{20} is 9.029 ± 0.008 Mev. This value is 58 kev lower than the value obtained by McDermott et al.(28) at Columbia. A possible explanation of this discrepancy is a saturation

problem in the analyzing magnet used at Columbia at that time (38). Evidence that magnet saturation effects are of no consequence in this experiment is given by the two excitation functions in figure 14 which required the maximum and minimum magnet currents used in the study of the O^{16} -alpha-capture reaction.

Angular distribution results are given in figure 15. The target-collimator-NaI detector geometry was similar to that shown in figure 28

The exact distances were 0.86" to the collimator, and 2.84" to the NaI. The main objective of this study was to show the ability of the apparatus to resolve a $P_4(\cos \theta)$ term in an angular distribution. The effect of the $P_4(\cos \theta)$ term can be seen directly in the decrease of the low angle points in the uncorrected angular distribution shown at the top of figure 15 for gamma rays in the energy window, 6.56 Mev to 8.58 Mev. The smooth curve through the points is the result of a least squares analysis for the coefficients in the formula

$$W(\theta) = A_0 + A_2 P_2(\cos \theta) + A_4 P_4(\cos \theta)$$

which gave (normalized to $A_0 = 1$),

$$W(\theta) = 1 + (0.306 \pm 0.017)P_2(\cos \theta) - (0.186 \pm 0.020)P_4(\cos \theta)$$

The uncertainty on each point is the standard deviation in the number of counts, and this uncertainty is indicated on one of the points.

Estimates of the background contribution to the counts taken on resonance were made by running an angular distribution below resonance. The relationship of the on resonance and the below resonance

runs is shown on the excitation function in figure 14 by two arrows. Subtracting the background determined in this fashion from the uncorrected data of figure 15 with additional corrections for target absorption (+2.2%), beam displacement (+1.1%), and Doppler shift (-4.3%) gave the lower set of points in the same figure. The smooth curve through these corrected data points is the result of a least squares analysis which gave

$$W(\theta) = 1 + (0.439 \pm 0.052)P_2(\cos \theta) - (0.243 \pm 0.057)P_4(\cos \theta)$$

The uncertainty on each point is primarily due to the statistical error of the counts after background subtraction.

Rose's smoothing factors (ref. 39, also see Appendix A) appropriate for the detector geometry are $J_2/J_0 = 0.884 \pm 0.009$, and $J_4/J_0 = 0.653 \pm 0.020$ where the uncertainty corresponds to a possible error of 0.1" in the distance from the target to the NaI crystal. The corrected angular distribution is

$$W(\theta) = 1 + (0.497 \pm 0.059)P_2(\cos \theta) - (0.372 \pm 0.087)P_4(\cos \theta)$$

This angular distribution agrees favorably with the expected angular distribution for an E2 transition from a 4^+ level to a 2^+ level given in table 3. The uncertainty in the final form of this angular distribution are mainly due to the uncertainty of the measured angular distribution.

The radiative width for the 7.40-Mev gamma-ray transition has been determined from the formula for the height of a thick target step for an isolated resonance (40)

$$SY(\theta) = \frac{\pi\sigma_r \Gamma}{2\epsilon} \frac{Qn \mathcal{E}(\theta)}{ze}$$

where

$Y(\theta)$ = step height in counts at angle θ with respect to the beam direction

σ_r = reaction cross section at resonance for producing the 7.40-Mev gamma ray

Γ = total width

ϵ = stopping power per molecule of target material

ze = charge of the bombarding particle

Q = integrated beam current per run

n = number of oxygen atoms per molecule of target material

S = spectrum fraction where $SY(\theta)$ is the total number of counts detected by the NaI at angle θ

$\mathcal{E}(\theta)$ = efficiency for detecting gamma rays in the NaI detector at angle θ with respect to the beam, where

$$\mathcal{E}(\theta) = \frac{1}{2} J_0 \sum_i A_i \frac{J_i}{J_0} P_i(\cos \theta)$$

In the formula for $\mathcal{E}(\theta)$, $\frac{1}{2} J_0$ is the detection efficiency of the NaI crystal for gamma rays that have an isotropic angular distribution, J_i/J_0 are Rose's smoothing factors, and the A_i are defined so that the angular distribution for the gamma radiation with respect to the beam axis is given by

$$W(\theta) = \sum_i A_i P_i(\cos \theta) \quad \text{with } A_0 = 1$$

A derivation of this formula for the detector efficiency is given in

Appendix A. The reaction cross section at resonance for gamma-ray production from $O^{16}(\alpha, \gamma)Ne^{20}$ in the energy range under consideration is given by (41):

$$\sigma_r = \pi \lambda^2 \omega \frac{\Gamma_\gamma \Gamma_\alpha}{(\frac{1}{2} \Gamma)^2}$$

where

Γ_α = alpha particle width

Γ_γ = radiative width for the gamma ray

Γ = total width = $\Gamma_\gamma + \Gamma_\alpha$

$2\pi\lambda$ = De Broglie wavelength for the bombarding particle

ω = statistical factors = $(2J + 1)$ where

J = spin of the compound level in Ne^{20} formed by $O^{16} + \alpha$

It will be assumed that the alpha particle width is much larger than the gamma-ray width, in which case substituting for the value of σ_r in the first equation and solving for $\omega\Gamma_\gamma$ gives for He^{++} beams:

$$\omega\Gamma_\gamma = 0.1989 \times 10^{-3} \frac{SY(\theta) \epsilon E}{Q \mathcal{E}(\theta) n} \quad (\text{ev})$$

where

E = beam energy in the laboratory in Mev

Q = charge in micro-Coulombs of He^{++}

ϵ = stopping cross section in units of 10^{-15} ev-cm^2

The radiative width for the 7.40-Mev gamma-ray transition from the 9.027-Mev level to the 2^+ first excited state of Ne^{20} has been determined with the aid of this formula. As an illustration of these calculations, the numbers used for determining the radiative width from the gamma-ray spectra that gave the He^+ excitation function in figure 14 are typical. By summing these spectra over the energy range 5.92 Mev to 7.91 Mev, a thick target step of 750 counts was obtained. The quantities put in the formula for the radiative width in terms of this height are:

S = spectrum fraction for $0.80 E_\gamma$ to $1.07 E_\gamma$ for a 7.40-Mev gamma ray = 1.81

ϵ = stopping power of Ta_2O_5 for alpha particles with 5.37 Mev = $238 \times 10^{-15} \text{ ev-cm}^2$ (43)

$n = 5$ (target material was Ta_2O_5)

$\mathcal{E}(\theta)$ = efficiency at $0^\circ = 0.104$

Q = integrated beam current $90 \mu\text{C}$ of He^+ .

The yield at 0° was taken as 750 counts with +5% correction for target absorption and absorption in the glass walled target chamber.

The value obtained for the product $\omega\Gamma_\gamma$ was

$$\omega\Gamma_\gamma = 3.1 \pm 0.4 \text{ ev}$$

The uncertainties assigned to the above quantities were:

S - 6%
ϵ - 2
$\mathcal{E}(\theta)$ - 6
statistics - 7
absorptions - 2
<hr/>
Q - 1
total 11%

where the uncertainty in the spectrum fraction includes both methods of extrapolating the low energy tails of the standard gamma-ray spectra used to determine the value of S.

Other measurements used for the calculation of the radiative width of this transition include data from other tantalum oxide targets as well as tungsten oxide targets, for NaI detector geometries with and without the collimator, and for a variety of distances between the target and the NaI detector ranging from 0.6" to 2.8". The best values for the parameters describing the 7.40-Mev gamma-ray transition are:

$$\omega\Gamma_{\gamma} = 3.4 \pm 0.4 \text{ ev}$$

$$\Gamma_{\gamma} = 0.38 \pm 0.05 \text{ ev}$$

$$|M|^2 = 7.0$$

where a spin of 4 has been used in the calculation of ω . The quantity $|M|^2$ is the ratio of the measured width to the width predicted by the Weisskopf single particle estimate for an E2 transition with this energy calculated with the specific formula given by Wilkinson (43). The final answer is assigned a 10% uncertainty due to the fact that there are

possible systematic errors in the measurements, especially in the value for the spectrum fraction, S .

It seems quite certain that the 9.03-Mev level seen in this work is the same level reported by McDermott et al. (28). The arguments in favor of this identification are the approximate agreement of the resonant energies, and the spin value. The width reported by McDermott et al. for this level is 4 kev (lab) and this agrees with the value of 3 to 4 kev indicated by the front edge rise of the excitation functions in figure 14.

Due to the lack of experimental information at the present time, the only theoretical significance that can be attached to the radiative width of the 7.40-Mev transition is that its strength of 7.0 Weisskopf units shows an enhancement typical of $E2$ transitions in the light nuclei (44). Litherland et al. (2) have proposed that the 9.03-Mev level is the 4^+ member of a $K = 0$ band based on either the 0^+ , 6.75-Mev level or the 0^+ , 7.22-Mev level in Ne^{20} . While the result from this experiment sheds no additional light on this suggestion, the strength of the transition to the ground state band would indicate the band containing the 7.40-Mev level has a particle configuration similar to the configuration for the ground state band.

6.93-MEV RESONANCE

Detailed studies made on the gamma rays from the 6.93-Mev resonance include a precise determination of the resonant energy, gamma-ray angular distributions, determination of radiative widths, investigation of the cascade scheme, and triple angular correlation

measurements. Interest in the corresponding level at 10.27-Mev excitation energy in Ne^{20} is due to the fact that the first $T = 1$ level in Ne^{20} , corresponding to the ground state of F^{20} and Na^{20} , is expected in this region of excitation (1).

The principal gamma ray seen in this experiment is the result of the 8.64-Mev transition from the 10.27-Mev level to the 2^+ first excited state of Ne^{20} at 1.63 Mev. Typical spectra are shown in figure 16. Again, as was the case for the 5.37-Mev resonance, the small bump corresponding to transitions direct to the ground state can be partially accounted for by summing of the cascade members in the NaI(Tl) detector. The dotted curve in figure 16 is a spectrum obtained below resonance at 6.89 Mev. The background behavior is rather complicated in this region. The 6.13-Mev radiation from the $\text{C}^{13}(\alpha, n\gamma)\text{O}^{16}$ reaction is rapidly decreasing with energy from a strong resonance at 6.878 Mev, while the 6.92- and 7.12-Mev gamma-rays from the same reaction are increasing with energy (11). The low energy portion of the spectrum, presumably neutron background and gamma rays from the $\text{O}^{18}(\alpha, n\gamma)\text{Ne}^{21}$ reaction, increases with energy through this region.

Precise determination of the resonance energy was made at the same time the analyzing magnet was calibrated. The excitation function obtained at that time for gamma rays in the energy range 7.10 Mev to 9.80 Mev is shown in figure 10 along with the data used for determining the magnet calibration constant. The best value for the resonance energy is $E_r = 6930 \pm 10$ kev, where the uncertainty is primarily due to uncertainty in the calibration constant. The rise of the front edge of this excitation function is consistent with a total width of 1 to 2 kev

or less as is explained in the section on energy calibrations.

Angular distribution measurements on the 8.64-Mev gamma ray have been made several times. Data typical of that obtained during these runs is shown in figure 17. The target-collimator-Na I detector geometry is similar to that shown in figure 28. The exact distances were 0.89" to the collimator from the target, and 2.81" to the NaI from the target. The number of counts in the gamma-ray spectra from 6.90 to 9.07 Mev with corrections for background, target absorption (+ 2.3%), beam displacement (+ 0.8%), and doppler shift (- 1.6%) are plotted as a function of cosine of the angle in figure 17. The errors on the data points are primarily statistical errors, and a typical value is shown on one of the data points. The background correction was obtained from angular distributions run above and below resonance. The interpolated values are the curve plotted at the bottom of figure 17. The energy relationship of above, on, and below resonance angular distribution runs is shown on the excitation function inserted in figure 17.

The curve through the angular distribution data points is the result of a least squares analysis which gave:

$$W(\theta) = 1 + (0.475 \pm 0.025)P_2(\cos \theta) + (0.004 \pm 0.031)P_4(\cos \theta)$$

Rose's smoothing factors appropriate for the geometry are $J_2/J_0 = 0.885 \pm 0.008$, $J_4/J_0 = 0.658 \pm 0.020$, where the uncertainties are due to a possible error of 0.1" in the distance to the detector. Application of these smoothing factors to the data in figure 17 gives:

$$W(\theta) = 1 + (0.537 \pm 0.031)P_2(\cos \theta) + (0.006 \pm 0.047)P_4(\cos \theta)$$

Errors in the final answer are primarily the statistical errors of the data. From this measurement and similar measurements, the best value for the gamma-ray angular distribution is:

$$W(\theta) = 1 + (0.529 \pm 0.017)P_2(\cos \theta) + (0.021 \pm 0.026)P_4(\cos \theta)$$

These numbers are close to the expected angular distribution for an M1 transition from a 2^+ level to a 2^+ level given in table 3, however the coefficient of $P_2(\cos \theta)$ term is approximately two standard deviations from the value for a pure M1 transition. The total absence of the $P_4(\cos \theta)$ term in the angular distribution initiated the investigation of the E2 transition discussed in the previous section on the 5.37-Mev resonance. The angular distribution for that transition showed the apparatus is able to resolve a $P_4(\cos \theta)$ term in an angular distribution.

The spin of 2^+ for the 10.27-Mev level in Ne^{20} would allow E2 transitions as well as M1 transitions to the 2^+ first excited state. Theoretical angular distributions for such transitions are a mixture of the two possible angular distributions with an additional interference term (45). For the transition in question, the angular distribution would have the form:

$$W(\theta) \approx W(\theta;M1) + 2\delta W(\theta;M1+E2) + \delta^2 W(\theta;E2)$$

where $W(\theta;M1)$ and $W(\theta;E2)$ are the angular distributions for pure M1 and E2 transitions respectively, and where $W(\theta;M1+E2)$ represents the interference term. With the coefficient of $P_0(\cos \theta)$ normalized to unity, the numerical formula for this angular distribution is:

$$W(\theta) = 1 + \frac{\frac{1}{2} + \delta(15/7)^{1/2} \delta^2(15/98)}{1 + \delta^2} P_2(\cos \theta) - \frac{\delta^2(24/49)}{1 + \delta^2} P_4(\cos \theta)$$

The quantity δ is the mixing parameter, and is defined as the ratio of the reduced matrix elements for the E2 and M1 operators, and hence δ^2 is the ratio of the two intensities. The reduced matrix elements may be made real (46) in which case the sign of δ can be either plus or minus. An additional discussion is given in Appendix A.

Plots of the Legendre polynomial coefficients as a function of the mixing parameter together with the experimental values are given in figure 18. The value for the mixing parameter obtained from this plot is:

$$\delta = (2.0 \pm 1.2) \times 10^{-2}$$

or that the intensity of the electric quadrupole radiation is 4×10^{-4} the intensity of the magnetic dipole radiation. In this case the value for δ can only be determined from the $P_2(\cos \theta)$ coefficient, while the coefficient for $P_4(\cos \theta)$ provides the necessary uniqueness. The mechanism that makes this very weak E2 transition visible is the interference with the M1 radiation which gives a term proportional to δ in the coefficient of $P_2(\cos \theta)$. It is worth noting that only a small change in the uncertainty assigned to δ would allow the probable values to range from zero up to $\sim 3.2 \times 10^{-2}$.

The radiative width for the 8.64-Mev gamma-ray transition from the 10.27-Mev level to the 2^+ first excited state of Ne^{20} has been computed with the formula given on page 33. Typical of the numbers

used in these calculations are those used to calculate the radiative width from the angular distribution data in figure 17. The height of the thick target step was taken as the number of counts in the upper curve of figure 17 with an additional (+ 1%) correction for the gamma-ray absorption in the 1/16" glass-walled target chamber. Other numbers used in the formula for the radiative width were:

$$S = \text{spectrum fraction of } 0.8 E_{\gamma} \text{ to } 1.07 E_{\gamma} \text{ for a } 8.64\text{-Mev gamma ray} = 1.74$$

$$\epsilon = \text{stopping cross section of } \text{Ta}_2\text{O}_5 \text{ for alpha particles with } 6.93\text{-Mev} = 206 \times 10^{-15} \text{ ev-cm}^2 \text{ (43)}$$

$$n = 5 \text{ (target material was } \text{Ta}_2\text{O}_5)$$

$$\mathcal{E}(\theta) = 2.49 \times 10^{-2} (1 + 0.475 P_2(\cos \theta) + 0.004 P_4(\cos \theta))$$

$$Q = 240 \mu\text{C of He}^{++}$$

An average value of $\omega \Gamma_{\gamma}$ for the seven data points in figure 13 is 28 ± 3 ev. The uncertainties on the above numbers, statistics of the data points, and corrections to the data are:

S - 9%
ϵ - 3
$\mathcal{E}(\theta)$ - 6
statistics - 2
corrections to data - 2
<hr/> Q - 1
total - 11%

The principal uncertainty is the spectrum fraction. The nine per cent uncertainty attached to this number covers both possible methods of extrapolating the low energy tails of the standard spectra.

Other sources used for the calculation of the radiative width of the 8.64-Mev gamma-ray transition includes data from tungsten oxide, tantalum oxide, as well as ice targets taken with the NaI(Tl) detectors with and without the collimator, for a variety of distances between detector and target. The best values for the parameters describing the 8.64-Mev gamma-ray transition are:

$$\omega\Gamma_{\gamma} = 27.8 \pm 3 \text{ ev}$$

$$\Gamma_{\gamma} = 5.6 \pm 0.6 \text{ ev}$$

$$|M|^2 = 0.41$$

where $|M|^2$ is the ratio of the measured radiative width to the Weiskopf single particle estimate for M1 transitions with this energy (43). The value of ω has been computed using a spin of 2 for the 10.27-Mev level. Since there are possible systematic errors in the calculation of the radiative width, the final answer is assigned an 11% uncertainty.

The ice targets were used as an independent means of checking the yields from the metallic oxide targets. Gamma-ray yields from the bombardment of ice targets made in situ with the specially designed target chamber shown in figure 4 were detected in a 3" x 3" NaI crystal placed 1.93" from the target at 0° with respect to the beam. At this single angle, it is possible to treat the gamma-ray absorption in the metal pieces of the target chamber with Rose's smoothing factors. These measurements give for the radiative width:

$$\omega\Gamma_{\gamma} = 29.8 \pm 6 \text{ ev}$$

The larger uncertainty is due to a poorer spectrum obtained from the ice targets.

By using the radiative widths above and the value of δ^2 obtained from the angular distribution measurements, the following parameters are obtained for the 8.64-Mev E2 transition from the 10.27-Mev level to the 2^+ first excited state in Ne^{20} :

$$\Gamma_{\gamma} = 2.2 \begin{array}{c} + 4.1 \\ - 1.9 \end{array} \times 10^{-3} \text{ ev}$$

$$|M|^2 = 1.7 \times 10^{-2}$$

Investigations of cascade gamma rays from the 10.27-Mev level were made with the fast-slow coincidence system described previously. As is to be expected, the 8.64-1.63-Mev cascade pair dominate the coincidence spectra. A typical coincidence spectrum for the 8.64-Mev gamma rays detected in a 3" x 3" NaI crystal placed 0.88" from the target at 90° to the beam is shown in figure 19C. These high energy gamma rays were in coincidence with low energy gamma rays in the energy window 1.275 to 1.850-Mev detected in the 4" x 4" NaI placed 1.25" from the target, and opposed to the 3" x 3" NaI crystal. This energy window is shown in the singles spectrum obtained from the 4" x 4" NaI crystal in figure 19B. The rapidly rising tail in the high energy gamma ray spectra starting in channel 55 was present in coincidence runs made off the resonances, and is due to real coincidences presumably from $\text{O}^{18}(\alpha, n\gamma)\text{Ne}^{21}$ or other (n, γ) processes. In particular

the energy window set around the photo peak of the 1.63-Mev gamma ray would also include the 1.40-Mev gamma ray transition from the second excited state to the first excited state of Ne^{21} (4). Possible identifications of these gamma rays are given in the low energy gamma-ray spectra of figure 19B.

By interchanging the role of the two crystals in the operation of the coincidence circuit, a spectrum for the 1.63-Mev gamma rays was obtained. This spectrum, shown in figure 19D, was shifted out of the singles spectra shown in figure 19B, on the condition that there was a fast coincidence, and that the high energy gamma ray was above 3.85 Mev (shown by the arrow in figure 19A).

It is interesting to note that other possible gamma-ray transitions in Ne^{20} that cascade through the 1.63-Mev level do not show up strongly in the spectrum in figure 19C. Of particular interest are a possible 6.02-Mev E2 transition to the 4^+ second excited state of Ne^{20} at 4.25 Mev which then decays by emission of a 2.62-Mev gamma ray to the 1.63-Mev first excited state and a possible 5.30-Mev E1 transition to the 4.97-Mev, 2^- third excited state which then decays to the first excited state by emitting a 3.34-Mev gamma ray (47). The strengths of these possible transitions can be roughly estimated at 10% or less of the 8.64-Mev transition strength from the data in figure 19C. A more direct measure of these strengths was made by coincidence measurements with an integral bias set above the 1.63-Mev gamma ray in the low energy channel at 2.26 Mev. In this fashion, the 8.64-Mev transition will not be

observed. The resulting high energy gamma-ray spectra showed the 1.63-Mev gamma ray, but little else that was recognizable as a gamma-ray spectrum. By attributing all the counts in these spectra from 3.67 Mev to 5.40 Mev to the possible E1 transition to the third excited state, and all the counts from 5.40 to 6.60 Mev as due to the possible E2 transition to the second excited state the following upper limits for the radiative widths of these transitions were obtained:

<u>E</u>	<u>Transition</u>	<u>Type</u>	<u>Γ_{γ}</u>	<u>$M ^2$</u>
6.02 Mev	10.27 \rightarrow 4.25	E2	$\lesssim 0.48$ ev	$\lesssim 22.8$
5.30	10.27 \rightarrow 4.97	E1	$\lesssim 0.44$ ev	$\lesssim 6 \times 10^{-3}$

where the upper limit obtained for the possible E2 transition is hardly a restriction. These radiative width limit determinations, which are admittedly crude, were made by assuming an isotropic angular distribution for the two coincident gamma rays, and then calculating the detection efficiency of the coincidence circuit from the product of the individual NaI detector efficiencies and the appropriate spectrum fractions. Calculating the radiative width for the 8.64-1.63-Mev gamma ray pair in this fashion gave a number 20% lower than the previously determined width, and the efficiencies calculated above have been decreased by this 20%. An estimated background of roughly 40% of the total counts has not been subtracted from the data. It is felt that these radiative widths are good upper limit estimates by roughly this factor of two.

The calculation of the radiative width for the transition direct to the ground state is hindered by the difficulty of estimating the summing contribution from the 8.64-1.63-Mev gamma-ray pairs. Such summing calculations are similar in nature to the calculations made for the coincidence circuit, but have the additional difficulty that they involve integrals over the spectrum shapes of the two gamma rays. Since these integrals can only be done analytically in cases where vast simplifications are made about the gamma-ray spectrum shapes, it is desirable to choose spectra obtained with a detector geometry that has low detection efficiency, and hence a small summing contribution. Spectra obtained during angular distribution measurements with the collimator have this desired property, and the spectrum in figure 16 which is the sum of spectra obtained during an angular distribution measurement was used for the calculations described below.

In this spectrum there were 1532 counts in the 8.64-Mev gamma-ray photo peaks in the region 7.29 Mev to 9.08 Mev that when combined with a pulse from a 1.63-Mev gamma ray above 0.44 Mev could add up to a count in the energy region 9.08 to 11.30 Mev. If it is assumed that the spectrum for the 1.63-Mev gamma ray is a delta function at 1.63 Mev, then the probability, P , for this occurrence per pulse in the 8.64-Mev photo peaks is:

$$P = \mathcal{E} \times \frac{1}{S} = 2.28 \times 10^{-2}$$

where \mathcal{E} is the detection efficiency for the 1.63-Mev gamma rays, and S is the spectrum fraction for pulses above 0.44 Mev for this gamma ray. In this fashion 35 of the counts in the energy range 9.08 to 11.30 Mev

can be attributed to summing. If it is assumed that both gamma-ray spectra are rectangular in shape, one half of this number would be obtained. Using the mean of these two estimates and subtracting a background of 85 counts, leaves 68 counts to be attributed to 10.27-Mev gamma rays. Substituting the appropriate numbers in the formula for the yield for a thick target gives for this E2 transition:

$$\omega\Gamma_{\gamma} = 0.95 \pm 0.24 \text{ ev}$$

$$\Gamma_{\gamma} = 0.19 \pm 0.05 \text{ ev}$$

$$|M|^2 = 0.6$$

The errors on these numbers are mainly due to the summing estimate (± 9 counts), and the large background subtraction.

Triple angular correlation measurements were made on the 8.64-1.63-Mev gamma rays from the 10.27-Mev level as preparation for similar measurements on gamma rays from the 7.93-Mev resonance. The coincidence counts between pulses detected above 3.90 Mev in the 4" x 4" NaI crystal and pulses detected above 0.95 Mev in a 2" x 2" NaI crystal are plotted as a function of the cosine of the angle between the 4" x 4" crystal and the beam direction in figure 20. The data points have been corrected for background, as determined from runs made below and above resonance, target absorption, and beam displacement effects with respect to the angle of the 4" x 4" crystal. The NaI crystals without collimators were placed in a plane with distances to the target of 1.05" and 0.98" for the 4" x 4" and 2" x 2" crystals respectively. A sketch of this geometry is given in figure 20. This

geometry has very poor angular resolution. It was felt that the loss of coincidence counting rate would not justify the proper geometry for high angular resolution.

Theoretical curves for various spin sequences and gamma-ray multipolarities are also plotted in figure 20. The coefficients for the 19 possible angular functions involved in specifying the triple angular correlation function for point counters have been modified by smoothing factors to obtain the theoretical curves for the detector geometry of this experiment. The theoretical curves obtained in this fashion were then adjusted in amplitude to give the best fit to the experimental points of figure 20. The "goodness of fit" to the experimental points was judged by the chi-squared test (48), and a summary of the probabilities for the various patterns is given in the caption for figure 20. The best fit is to the spin-gamma-ray multipole sequence: $2^+(M1)2^+(E2)0^+$. This supplies confirming evidence for the spin assignment of 2^+ for the 10.27-Mev level obtained by the double angular correlation measurements. There is a possibility that the more complex gamma-ray cascades starting from the 10.27-Mev level and going through the 1.63-Mev first excited state may have contributed coincidence counts to the data in figure 20. However the previously described search for such cascades by coincidence techniques indicates these more complex cascades are weak. Particular details about the calculation of the theoretical triple angular correlation functions are given in Appendix A.

The experimental information about the new level at 10.27-Mev excitation energy in Ne^{20} indicates that this level is the first $T = 1$ level in Ne^{20} corresponding to the ground state of F^{20} and Na^{20} .

The $T = 1$ assignment is supported by the excitation energy, spin and parity, radiative width, and alpha-particle width.

The calculation of the expected position of the first $T = 1$ level in Ne^{20} is hindered by the inaccurate value for the $\text{Ne}^{20} - \text{Na}^{20}$ mass difference. Without this mass difference it is impossible to determine the Coulomb radius for the mass 20 isotopic spin triplet. Calculating the Coulomb radius of nearby isotopic spin doublets and triplets and comparing these radii with the formula

$$R = r_0 A^{1/3}$$

gives r_0 the value: $r_0 = (1.45 \pm 0.05) \times 10^{-13}$ cm where the uncertainty includes most of the examples from mass 17 to mass 22. Using the radius from the formula for calculating the Coulomb energy difference in F^{20} and Ne^{20} and making corrections for the neutron-proton mass difference gives 10.23 ± 0.14 Mev for the position of the first $T = 1$ level in Ne^{20} . Wilkinson (49) obtains a value of 10.22 Mev for the position of the first $T = 1$ level in Ne^{20} by using the Coulomb energy difference in $\text{F}^{19} - \text{Ne}^{19}$ doublet corrected by $(1 - \frac{1}{A})^{1/3}$. In principle, this latter method is probably more accurate since the only assumption is that the charge distribution in Ne^{19} is similar to that in Ne^{20} . Typical discrepancies of values calculated in this fashion with known positions of $T = 1$ levels in the self conjugate light nuclei is of the order of 50 kev. The excitation energy of the new level at 10.27 Mev is then in the correct energy range for the level to be the first $T = 1$ level in Ne^{20} .

Besides showing that the 10.27-Mev level is at the correct excitation energy, it is also necessary to demonstrate that this level has properties similar to the $\text{Na}^{20} - \text{F}^{20}$ ground states. Unfortunately Na^{20}

is difficult to make and so far this nucleus has escaped close scrutiny. The most direct information pertaining to the ground state spin of F^{20} is from a measurement of the circular polarization of the Ne^{20} , 1.63-Mev gamma ray that follows the beta decay of the F^{20} ground state (50). The results of this experiment are consistent only with a spin of 2. Measurement of a small anisotropy in the beta-gamma angular distribution of this decay by Boehm et al. (51) supplies confirming evidence. The positive parity assignment given to the ground state of F^{20} is based on the allowed beta-ray transition to the 2^+ first excited state of Ne^{20} (52). The spin of the new level seen in this experiment at 10.27 Mev is 2 on the basis of gamma-ray angular distribution measurements; the parity is positive from the nature of the alpha capture reaction on O^{16} .

The strong 8.64-Mev transition to the first excited state can be used as further evidence for the $T = 1$ nature of the new level. Arguments about the strengths of M1 transitions in self conjugate nuclei are based on the theoretical estimates of Morpurgo (53), who was able to show the isotopic spin scalar part of the M1 matrix element is approximately 1/100 the intensity of the vector part. Morpurgo interprets this result to mean: "M1 transition strengths between levels with the same T in self-conjugate nuclei are expected to be on the average weaker by a factor of a 100 than the average normal M1 transition strengths." Warburton (54) changes this estimate to a factor of 30 by arguing that the average nuclear level will have an isotopic spin impurity of 3% in intensity. From his compilation of M1 transition rates in self-conjugate nuclei for $A \leq 20$, Warburton concludes the average normal M1 transition

for these nuclei are 0.15 Weisskopf units (i. e. the ratio of the experimental width to the width calculated from the Weisskopf single particle limit is 0.15), and the seven known M1 transitions with $\Delta T = 0$ are roughly 1/10 of this number.

The difficulty with such arguments for a particular case is that one can never be sure that it is not an exception. For example, the largest isotopic spin impurity is 10%, the strongest M1 transition is 4 Weisskopf units (44), and combining these numbers it is possible to argue that the fastest "inhibited" M1 transition would be 0.4 Weisskopf units. However Warburton concludes from his compilation that transitions stronger than 0.1 Weisskopf units are most probably isotopic spin changing transitions in the light self-conjugate nuclei. By applying such arguments to the 8.64-Mev gamma ray with its transition strength of 0.41 Weisskopf units, further evidence is supplied for the $T = 1$ assignment.

Electric dipole transitions in self-conjugate nuclei have isotopic spin selection rules similar to those for magnetic dipole transitions (31). Wilkinson (43) finds that the average of the E1 strengths in the light nuclei is 0.055 Weisskopf units, and for transitions weaker than 1.5×10^{-3} Weisskopf units the chances are 10 to 1 the isotopic spin has not changed. The upper limit for the strength of the 5.30-Mev E1 transition from the 10.27-Mev level to the 4.97-Mev level is four times this number, and probably it is not wise to draw any further conclusions.

Somewhat similar arguments can be based on the alpha-particle width. Since both O^{16} and He^4 are $T = 0$ particles, a $T = 1$ assignment for the 10.27-Mev level would imply the formation of this level

by $O^{16} + \alpha$ takes place through a $T = 0$ impurity (55). An "average impurity" is $\sim 3\%$ in intensity (44), and hence one might expect a small alpha-particle width for such a $T = 1$ level.

The front edge rise of the excitation function for the 6.93-Mev resonance is consistent with a total width of 1 to 2 kev or less. Attributing all of the possible 2 kev width to the alpha-particle width, and calculating the dimensionless reduced width, θ^2 , from the formula

$$\Gamma_{\alpha} = 2kR P_{\ell} \theta^2 (3\hbar^2 / 2MR^2)$$

where

Γ_{α} = alpha-particle width (center of mass)

k = wave number = $0.1542(2ME)^{1/2} \times 10^{-13}$ cm

M = reduced mass = 3.2 amu

E = center of mass energy = $0.8E_{\alpha}$

R = channel radius = $(1.414 \times 16^{1/3} + 2.190) \times 10^{-13}$ cm

P_{ℓ} = penetration factor (56)

a value of $\theta^2 \lesssim 0.8 \times 10^{-3}$ of the Wigner limit ($\theta^2 = 1$) is obtained. Even though numbers of this order of magnitude are not uncommon for the dimensionless reduced widths of the $T = 0$ levels in Ne^{20} (28), this number is the upper limit for the 10.27-Mev level and the dimensionless reduced width may well be considerably smaller.

It should be noted once again that the radiative widths have been calculated under the assumption that $\Gamma_{\gamma} \ll \Gamma_{\alpha}$. None of the results from this experiment can be used to justify this assumption. If this should fail to be the case, all the numbers quoted for the radiative widths would be increased, thus strengthening the arguments for the $T = 1$

assignment.

In the preliminary results of Davis et al. (29) on elastic scattering of alpha-particles on O^{16} , no signs of this 2^+ resonance are seen at 6.93 Mev, but a narrow resonance of this sort might have easily been missed. The broad (~ 150 kev) resonance with a tentative spin assignment of 5^- that they do find at 6.97 Mev has not been seen in this experiment.

7.94-MEV RESONANCE

Measurements made on the gamma rays from the 7.94-Mev resonance, corresponding to a level in Ne^{20} at 11.08-Mev excitation energy, include a determination of the resonant energy, gamma-ray angular distributions, determination of the radiative width, investigation of the cascade scheme, and triple angular correlations.

The principal gamma ray seen at this resonance is the 6.83-Mev transition to the 4^+ second excited state of Ne^{20} at 4.25 Mev. This level in turn cascades through the 2^+ first excited state giving 2.62- and 1.63-Mev gamma rays. The simultaneous detection of the high energy gamma ray together with other members of the cascade is responsible for the presence of this resonance in the excitation function for radiation to the first excited state and the ground state shown in figure 12. Spectra obtained during these early measurements showed no strong transitions to the first excited state, and this was taken for evidence that the spin of this level was relatively high; 5^- , 6^+ , or possibly 4^+ . However estimates of the radiative width from preliminary

coincidence measurements gave $\omega\Gamma_{\gamma} = 43$ ev which is only a reasonable number for an uninhibited M1 transition from a 4^+ level. Furthermore, when the ground state of F^{20} is equated to the 10.27-Mev level in Ne^{20} , this level corresponds in energy almost exactly to the second excited state of F^{20} . The possibility that this level was another $T = 1$ level lead to the additional work described below.

Gamma-ray spectra shown in figure 21 were obtained at bombarding energies below, on, and above the 7.94-Mev resonance. The energies at which these spectra were taken are shown on the excitation function for the 6.83-Mev radiation in figure 22A. The on resonance spectrum in figure 21B shows the 6.83-Mev radiation and the very strong 4.43-Mev radiation from $C^{12}(\alpha, \alpha'\gamma)C^{12}$. As observed with the other cascade gamma rays there is a summing contribution above the 6.83-Mev gamma ray that hides possible transitions to the ground state and first excited state. Off resonance spectra in the same figure also shows the 4.43-Mev carbon gamma ray together with the weaker 6.13-Mev and some suggestion of the 7-Mev radiations from $C^{13}(\alpha, n\gamma)O^{16}$.

Fortunately the yield of gamma rays from $C^{13}(\alpha, n\gamma)O^{16}$, which is the most serious background in the study of the 6.83-Mev radiation, is smoothly decreasing with increasing alpha-particle bombarding energy in the region of interest from a series of strong resonances at 7.927, 7.88 and 7.736 Mev to a minimum at 8.05 Mev (11). The fact that the yield of these gammarays appears weak in comparison to the 4.43-Mev radiation from C^{12} is due to the low, 1.11%, abundance of C^{13} in natural carbon. The rise and fall of the 4.43-Mev radiation seen

in these three spectra is due to the first strong resonance in the $C^{12}(\alpha, \alpha'\gamma)C^{12}$ reaction at 7.96 Mev (57). Fortunately the counting rates are very low (7.3 counts per channel per second average in channels 49 to 61) and pulse pile-up leading to additional counts under the 6.83-Mev gamma-ray photo peaks is negligible. It is felt that in spite of the serious background problem reasonable measurements would be possible on the 6.83-Mev gamma ray.

Prior to the measurements of the resonant energy for this gamma ray, the slits on the 90° analyzing magnet were removed for the installation of new equipment. For this reason no effort has been made to establish the resonant energy with the precision attempted for the 6.93- and 5.37-Mev resonances. With slit widths of 0.200" at the entrance and exit of the 90° analyzing magnet, the average of three determinations is 9744 ± 20 kev. The magnet calibration is based on the 6.93-Mev resonance in Ne^{20} , and the uncertainty quoted is roughly half the value indicated by the slit settings, and twice the spread of the measurements. The fact that the measurements are more reproducible than the estimate obtained from the slit geometry of the 90° analyzing magnet for a beam of no lateral extent is not surprising in view of the finite size of the beam, and the automatic centering of the beam in the exit slit of the 90° magnet by the energy regulation circuit of the accelerator. Two typical excitation functions are shown in figure 22. Even though the one shown in figure 22A lacks a point at the bottom of the front edge rise, the resulting uncertainty in the resonant energy is only ± 3 kev.

The total width as determined from the $1/4$ to $3/4$ rise of the front edge of the excitation function in figure 22B indicates a width of 3.2 kev. The beam stability is in the order of 1 to 2 kev indicating the total width of the resonance is less than this number.

Angular distribution measurements were made with a target-collimator-NaI(Tl) detector geometry similar to that shown in figure 27. The exact distances were 0.86" from the collimator to the target, and 2.84" from the NaI crystal to the target. Angular distributions were made on, below, and above resonance, at energies shown by arrows on the excitation function for the 6.83-Mev gamma ray in figure 22A. The gamma-ray spectra in figure 21 were obtained during these measurements, and are the sum of spectra at various angles. To minimize possible errors in the estimate of the background contribution to the counts on resonance, the measurements were made in two different sequences. During the first sequence, complete angular distributions were made, first on resonance, then below, and finally above resonance. For the second sequence, these three runs were made at each angle before the angle was changed. The argument in favor of the first sequence of runs is that a minimum of adjustment of the accelerator was required during the three angular distribution measurements. However the fact that these measurements required 6.75 hr. favored the second approach. An estimate of the constancy of the background was obtained from the angular distribution of the C^{12} , 4.43-Mev gamma ray. The angular distributions for this gamma ray obtained during the first sequence of runs showed pronounced quadrupole patterns which

became "washed out" as the energy increased past the 7.96-Mev resonance. The patterns obtained during the second sequence of runs show a 10% discontinuity, probably from a change in the beam spot size. However, this discontinuity is reflected in the background estimates of the second sequence of runs, and it is felt that the discontinuity has been properly handled.

A plot of the angular distribution for the 6.83-Mev gamma ray is shown in figure 23. This plot was obtained by summing the spectra over the energy range, 5.72 to 7.40 Mev, for the data combined after subtraction of the background and corrections for beam spot displacement (-1.9%), target absorption (1.8%), and Doppler shift (-3.5%). The smooth curve through the data points is the result of a least squares analysis which gave:

$$W(\theta) = 1 + (0.252 \pm 0.019)P_2(\cos \theta) - (0.033 \pm 0.024)P_4(\cos \theta).$$

Angular distributions for gamma rays in the energy ranges 5.37 to 7.40 Mev and 6.11 to 7.40 Mev were also measured and the angular distribution functions are within half a standard deviation of the numbers given above. The average background removed from the data in figure 23 is shown by the lower curve. Uncertainties indicated on the data points are primarily due to the uncertainty in the background subtraction.

Rose's smoothing factors appropriate for the geometry are:

$J_2/J_0 = 0.883 \pm 0.008$ and $J_4/J_0 = 0.652 \pm 0.021$, where the uncertainties allow for a possible error of 0.1" in the target-detector distance.

Using these numbers to correct the measured angular distribution, one obtains:

$$W(\theta) = 1 + (0.285 \pm 0.022)P_2(\cos \theta) - (0.051 \pm 0.037)P_4(\cos \theta)$$

Comparing these coefficients with the theoretical angular distributions for transitions to a 4^+ level given in table 3 shows the angular distribution is intermediate between the expected angular distributions of a $4^+(M1)4^+$ transition and a $2^+(E2)4^+$ transition.

An assignment of 4^+ to the 11.08-Mev level would allow a mixture of M1 and E2 decays to the 4^+ second excited state. In this case the angular distribution is given by:

$$W(\theta) = 1 + \frac{\frac{1}{2} + \delta(45/17)^{1/2} - \delta^2(325/1078)}{1 + \delta^2} P_2(\cos \theta) - \frac{\delta^2(324/532)}{1 + \delta^2} P_4(\cos \theta)$$

where the mixing coefficient, δ , is the ratio of the reduced matrix elements for the E2 and M1 transitions respectively. As explained previously, the sign of δ can be either plus or minus, allowing two possible values for the coefficient of the second Legendre polynomial. Plots of the Legendre polynomial coefficients as a function of the mixing coefficient together with the experimental values are given in figure 24. The value of the mixing coefficient as determined from the second Legendre polynomial coefficient is:

$$\delta = -0.238 \pm 0.023$$

or the intensity of the E2 radiation is 5.66×10^{-2} times the intensity of the M1 radiation. This value for the mixing parameter is consistent with the value obtained from $P_4(\cos \theta)$.

In spite of the fact that the coefficient for $P_2(\cos \theta)$ is four

standard deviations from the value expected for a $2^+(E2)4^+$ transition, it does not seem wise to rule out the possibility that the 11.08-Mev level has a spin of 2^+ on the angular distribution data alone since there is a serious background problem.

Triple angular correlation measurements made on the 6.83-2.62-Mev gamma rays using the techniques described in the discussion of similar measurements for the gamma rays from the 6.93-Mev resonance on page 47 failed to give additional information because of poor statistics. Shown in figure 25 are the coincidence counts between pulses detected above 5.10 Mev in the 4" x 4" NaI crystal and pulses detected above 1.73 Mev in a 2" x 2" NaI crystal plotted against the cosine of the angle between the 4" x 4" NaI crystal and the beam direction. The chi-squared values for the fits given in the figure caption for figure 25 indicate that at best the triple angular correlation data could be used to rule out possible 3^- and 5^- assignments for the 11.08-Mev level.

Estimates of the radiative width for the 6.83-Mev gamma ray have been made from data obtained from several tantalum oxide targets and a variety of NaI(Tl) detector geometries. The average value for the product $\omega\Gamma_\gamma$ is:

$$\omega\Gamma_\gamma = 46 \pm 5 \text{ ev}$$

As an example of these calculations, the average value for the radiative width obtained from the seven angular distribution data plots in figure 23 was $\omega\Gamma_\gamma = 47.5 \pm 5 \text{ ev}$. The numbers used in the calculations of the radiative width from the height of the thick target step given in the discussion of the 5.37-Mev resonance were:

S = spectrum fraction for $0.84E_{\gamma}$ to $1.09E_{\gamma}$ for a 6.83-Mev gamma ray = 1.92

ϵ = stopping cross section for Ta_2O_5 for alpha particles with 7.94 Mev = 191×10^{-15} ev-cm²

n = 5 (target material was Ta_2O_5)

$$\mathcal{E}(\theta) = \text{detector efficiency} = 2.52 \times 10^{-2} (1 + 0.252P_2(\cos \theta) - 0.033P_4(\cos \theta))$$

Q = 500 μ C of He⁺⁺

where the height of the thick target step was taken as the number of counts in figure 23 with an additional (+1%) correction for the absorption in the glass-walled target chamber. The uncertainties on the above constants, statistics of the data points, and corrections are:

S - 6%
$\mathcal{E}(\theta)$ - 6
ϵ - 2
corrections to data - 2
statistics - 3
Q - 1
total - 10%

A 10% error is assigned to the average value for the product $\omega\Gamma_{\gamma}$ quoted above since there are possible systematic errors in the calculations.

The size of the term, $\omega\Gamma_{\gamma}$, can be used as further evidence that the spin of the 11.08-Mev level is 4^+ . A spin of 4^+ and the value of $\delta = -0.238$ determined from the angular distribution give the following numbers for the radiative widths of the 6.83-Mev M1 and E2 transitions:

$$\begin{aligned}\Gamma_{\gamma}(\text{M1}) &= 4.8 \pm 0.5 \text{ ev} \\ |M|^2 &= 0.72 \text{ - - for M1} \\ \Gamma_{\gamma}(\text{E2}) &= 0.29 \pm 0.07 \text{ ev} \\ |M|^2 &= 7.3 \text{ - - for E2}\end{aligned}$$

Assuming the 11.08-Mev level is 2^+ , the gamma ray is E2, and the radiative width is:

$$\begin{aligned}\Gamma_{\gamma}(\text{E2}) &= 9.2 \pm 1.0 \text{ ev} \\ |M|^2 &= 236 \text{ - - for E2}\end{aligned}$$

Considering that the strengths of the E2 transitions in the ground state band of Ne^{20} are only 38 and 28 Weisskopf units for the transitions, first excited state to ground state, and second excited state to first excited state (32), a value of 6 - 9 times these numbers for a transition from a level which is not in the ground state band is unreasonable. However, Wilkinson (44) has estimated a value of 300 Weisskopf units for a supposed E2 transition in B^{10} from the data of Meyer-Schützmeister et al. (58). Even though this B^{10} transition is exceptionally strong when compared to other E2 transitions in the light nuclei it may be the 6.83-Mev transition is another such exception.

Further evidence for the 4^+ assignment can be obtained from the small radiative widths for transitions to the first excited state and ground state. By making estimates of the summing contributions from the main cascade to counts attributable to the 9.45- and 11.08-Mev transitions, the limits $\omega\Gamma_{\gamma} \lesssim 0.7 \text{ ev}$ and $\omega\Gamma_{\gamma} \lesssim 6.8 \times 10^{-3} \text{ ev}$ are obtained for the two transitions. By then assuming the 11.08-Mev level

is 2^+ or 4^+ , the following assignments would be made:

a) 2^+ assignment for the 11.08-Mev level

1) 9.45-Mev transition

$$\Gamma_{\gamma} \lesssim 0.14 \text{ ev}$$

$$|M|^2 \lesssim 7.9 \times 10^{-3} \quad \text{for pure M1}$$

$$|M|^2 \lesssim 0.7 \quad \text{for pure E2}$$

2) 11.08-Mev transition

$$\Gamma_{\gamma} \lesssim 1.4 \times 10^{-3}$$

$$|M|^2 \lesssim 3.5 \times 10^{-3} \quad \text{for E2}$$

b) 4^+ assignment for 11.08-Mev level

1) 9.45-Mev transition

$$\Gamma_{\gamma} \lesssim 0.08 \text{ ev}$$

$$|M|^2 \lesssim 0.4 \quad \text{for E2}$$

2) 11.08-Mev transition

$$\Gamma_{\gamma} \lesssim 8 \times 10^{-4} \text{ ev for E4}$$

In view of all the evidence, the possibility that the 11.08-Mev level is 2^+ is very small. The 2^+ assignment would require explanations for the four standard deviations in the angular distribution fits, an enormous E2 width to the second excited state with weak E2 transitions to the two lower states, and a weak M1 transition to the second excited state. If a 4^+ assignment is made, reasonable values are obtained.

Investigation of other cascades from the 4^+ , 11.08-Mev level by coincidence techniques was hindered by the three gamma-ray cascade initiated by the 6.83-Mev radiation. Neither a possible 3.43-Mev,

E2 gamma-ray transition to a level of 7.65 Mev that is thought to be 6^+ (59), nor a possible 4.06-Mev, E1 transition to a level at 7.02 Mev that is thought to be 4^- (59) were seen. The upper limit for these transition strengths can be placed no lower than $1/5$ of the main transition strength, and while this limit is hardly a restriction on the possible E2 transition, this limit on the E1 transitions gives $\Gamma_\gamma(E1) \lesssim 1.4$ ev or $|M|^2 \lesssim 4.3 \times 10^{-2}$. In this estimate an allowance has been made for the fact that $\sim 30\%$ of the decays from the 7.02-Mev level give low energy gamma rays followed by alpha particles.

The experimental data can be used to infer a $T = 1$ assignment for the 11.08-Mev level. The evidence for this assignment is the M1 width, the excitation energy of the level, and the alpha-particle width. The excitation energy of 11.084-Mev places this level 810 ± 18 kev above the 10.27 Mev level. The second excited state of F^{20} occurs at 828 ± 8 kev (19). Thus within the errors, the 11.08-Mev level would correspond to the F^{20} second excited state if it had a $T = 1$ assignment. The $T = 1$ assignment can be made on the basis of the 6.83-Mev M1 transition strength. A comparison of the 0.72 Weisskopf units for the strength for this transition to the M1 strengths in other self conjugate light nuclei in Warburton's compilation (54) places this transition in the category of most likely an isotopic spin changing transition. A $T = 1$ assignment would also imply a small alpha-particle width for break-up into $\alpha + O^{16}$. Attributing all of the measured width of 3.2 kev to the alpha-particle width, an upper limit of 2.1×10^{-3} is obtained for the ratio to the Wigner single particle limit. While such a number does not confirm the $T = 1$

assignment, it is important for the arguments that it is small (55).

The one missing piece of information is the spin of the second excited state of F^{20} . The proton group to this state from the $F^{19}(d, p)F^{20}$ stripping reaction reported by El Bedewi (60) exhibits a characteristic $l = 2$ Butler pattern. On this basis, El Bedewi has assigned possible spin values of 1^+ , 2^+ , or 3^+ to this level. However his data shows this proton group is only 1/16 as strong as the $l = 2$ groups to the first and 7th excited states. A possible explanation for the weakness of this group is that with the neutron being captured into the s - d shell, it would be necessary to resort to spin flip stripping to make a 4^+ level.

The 11.08-Mev level has possibly been seen in two other experiments. Butler (37) using a gamma-ray threshold technique on the $F^{19}(d, n\gamma)F^{20}$ reaction reports a level at 11.08-Mev excitation energy in Ne^{20} . This level decays by emitting a 9.6-Mev gamma ray in a transition to the first excited state. While the excitation energy of this level agrees with the energy found in this experiment, there is no agreement on the cascade scheme. Possibly the 9.6-Mev gamma ray that Butler reports is the result of detection of the 6.83-Mev gamma ray and one of the other cascade members in his two crystal gamma-ray spectrometer. Davis et al. (29) have reported a poorly resolved level at 11.10 Mev in Ne^{20} in their preliminary results from alpha-particle scattering in O^{16} .

From the experimental data and discussion given above, the 11.08-Mev level in Ne^{20} is 4^+ , and most likely the Ne^{20} $T = 1$ analog of the F^{20} second excited state.

OTHER RESONANCES

The resonances described in this section have not received the attention given to the resonances at 5.37, 6.93, and 7.94 Mev. Most of the results quoted below have been derived from the excitation function presented in figure 11 and figure 12. Resonant energies have not been determined with the highest attainable precision, and the values quoted below are based on the 5.374-Mev and the 6.930-Mev resonances in $O^{16}(\alpha, \gamma)Ne^{20}$. Where applicable, radiative width estimates have been made from the formula for the height of a thick target step given in the discussion of the 5.37-Mev resonance. The modifications made to this formula for those resonances that show measureable widths follow the form of Fowler et al. (40). In particular the maximum yield is related to the radiative width by:

$$\frac{\omega \Gamma_Y \Gamma_a}{\Gamma} = 0.1989 \times 10^{-3} \frac{S \epsilon E Y(\theta)_{\max}}{Q \mathcal{E}(\theta) n} \cdot \frac{\pi}{2 \tan^{-1} \frac{t}{T}}$$

where $Y(\theta)_{\max}$ is the maximum yield at angle θ , and t is the target thickness in energy units. The other factors are defined on page 32. Similarly, the area under the yield curve is related to the radiative width by:

$$\frac{\omega \Gamma_Y \Gamma_a}{\Gamma} = 0.1989 \times 10^{-3} \frac{S \epsilon E}{Q \mathcal{E}(\theta) n} \cdot \frac{\int Y(\theta) dE}{t}$$

where $\int Y(\theta) dE$ is the area in counts-energy units.

In the estimates of the radiative widths for the resonances discussed below, it has been assumed that the angular distribution is

isotropic. The error introduced in this fashion is arbitrarily taken to be 25%. For one of the resonances, sufficient information is available about the spin of the level and probable multipolarity of the radiation to allow a reasonable estimate of the correction factor for the angular distribution. This estimate is given in the discussion of the 6.61-Mev resonance.

5.94-MEV RESONANCE

This resonance is shown on the excitation function for radiation to the ground state and first excited state of Ne^{20} given in figure 11. Even though the region has only been covered in 20-kev steps, the yield curve for the 5.94-Mev resonance shows a definite thin target shape. The yield in figure 11 reaches a maximum at 5.955 ± 0.010 Mev. The calculated target thickness at this energy is 52 ± 5 kev, and this value and the value of the maximum yield give 5.93 ± 0.03 Mev as the resonance energy, corresponding to a level in Ne^{20} at 9.48 ± 0.03 Mev. The uncertainty assigned to the resonant energy allows for uncertainties in the beam energy as well as an additional uncertainty in the location of the maximum yield. The width of the yield curve is 63 ± 10 kev, indicating a resonant width of 29 ± 15 kev in the center of mass.

Gamma-ray spectra obtained at this bombarding energy show the 7.85-Mev transition to the first excited state of Ne^{20} , with a weaker transition to the ground state. Estimates of the radiative width for the transition to the first excited state by the height formula and the area formula give $\omega\Gamma_{\gamma} = 1.56$ and 1.25 ev respectively. Probably the area under the yield curve is the better estimate in these circumstances, and

the best estimate is considered to be $\omega\Gamma_{\gamma} = 1.3 \pm 0.5$ ev. The uncertainty in this number allows for a substantial background subtraction that was estimated by drawing a straight line under the yield curve, as well as the possible error incurred by neglecting angular distribution effects. Similar estimates for the radiative width of the 9.48-Mev transition direct to the ground state gave $\omega\Gamma_{\gamma} \lesssim 0.3$ ev. This width is only a rough upper limit due to poor statistics, a large background, and the difficulty of estimating the summing contribution from the 7.85-1.63-Mev cascade gamma rays to the counts in the photo-peak region of the 9.48-Mev gamma ray.

The gamma-ray decay scheme indicates possible spin values of 1^{-} or 2^{+} for the 9.48-Mev level in Ne^{20} . McDermott et al. (28) have found a 2^{+} resonance with a width of 24 kev in the center of mass at 6.03-Mev bombarding energy corresponding to a level at 9.55 Mev in Ne^{20} . Most likely the two resonances are the same even though the energy discrepancy is 70 kev instead of the 58 kev noted in the discussion of the 5.37-Mev resonance. Corroborating evidence for the identity of this resonance is obtained from the preliminary data of Davis et al. (29) who report a resonance at 5.95 Mev bombarding energy with tentative spin-parity assignment, 2^{+} . A 2^{+} spin value for this resonance would then allow E2 and M1 transitions to the first excited state, as well as E2 transitions to the ground state. The parameters in these cases are:

- a) 7.85-Mev transition to the first excited state

$$\Gamma_{\gamma} = 0.26 \pm 0.1 \text{ ev}$$

$$|M|^2 = 3.2 \text{ - - for pure E2}$$

$$|M|^2 = 0.025 \text{ - - for pure M1}$$

b) 9.48-Mev transition to the ground state

$$\Gamma_{\gamma} \leq 0.06 \text{ ev}$$

$$|M|^2 \leq 0.3 \text{ - - for E2}$$

The spin assignment of 2^+ also allows calculation of the reduced width for the alpha particle. These numbers are:

$$\Gamma_{\alpha} = 29 \pm 15 \text{ kev}$$

$$\theta^2 = 1.49\%$$

where the total width has been taken as the alpha particle width.

6.61-MEV RESONANCE

This resonance is shown on the excitation function for radiation to the ground state and first excited state of Ne^{20} given in figure 11. Parameters describing this resonance have been calculated in the same fashion as the parameters used to describe the 5.94-Mev resonance. The width of the yield curve in figure 11 at half maximum is 199 ± 30 kev. The target thickness at this energy is 51 ± 5 kev indicating a resonance width of 155 ± 30 kev in the center of mass. The maximum yield is at 6.63 Mev, locating the resonance at 6.61 ± 0.03 Mev, corresponding to a level in Ne^{20} at 10.02 ± 0.03 Mev. Gamma-ray spectra obtained in this energy region show the 8.39-Mev gamma ray from the transition to the first excited state with little if any direct transitions to the ground state. Coincidence measurements made at this energy showed an 8.4-Mev gamma ray in coincidence with a 1.63-Mev gamma ray, but poor

statistics prevent any statements about possible transitions to higher excited states in Ne^{20} .

The radiative width has been estimated from the data used to obtain the excitation function shown in figure 11. A value of $\omega\Gamma_{\gamma} = 8 \pm 3$ ev was obtained for the gamma-ray transition to the first excited state. The large uncertainty again is primarily due to the background and possible errors incurred by neglecting the angular distribution. An estimate of the gamma-ray transition width to the ground state can only be given in the form of an upper limit since it is possible to attribute all of the counts seen in the region to the 10.0-Mev gamma-ray photo-peaks to summing of the cascade radiation from the 8.39-1.63-Mev transitions. At most for the transition to the ground state, $\omega\Gamma_{\gamma} \lesssim 0.6$ ev.

The gamma-ray decay scheme indicates possible spin values of 3^{-} or 4^{+} for the 10.02-Mev level in Ne^{20} . Of the other experiments that yield information about levels in Ne^{20} in this excitation energy range, the results of McDermott et al. and Davis et al. from the elastic scattering of alpha particles in O^{16} are the most helpful. Although McDermott et al. stopped at 6.5-Mev bombarding energy, they found it necessary to postulate a broad 4^{+} resonance just beyond their range in order to obtain good theoretical fits to their data above 5.6 Mev. Davis et al. report in their preliminary data a broad resonance at 6.58 Mev having a width of approximately 120 kev, and tentative spin-parity of 4^{+} . If it is assumed this resonance is 4^{+} , then the parameters for the gamma radiation to the first excited state and ground state are:

- a) 8.39-Mev transition to the first excited state

$$\Gamma_{\gamma} = 0.9 \pm 0.4 \text{ ev}$$
$$|M|^2 = 6.9 \text{ - - for E2}$$

- b) 10.02-Mev transition to the ground state

$$\Gamma_{\gamma} \lesssim 0.07$$

where it has been assumed the gamma-ray angular distribution is isotropic.

It is worthwhile to illustrate the steps that should be taken to correct the data for angular distribution effects. A 4^+ assignment for the 10.02-Mev level in Ne^{20} would imply the transition to the 2^+ first excited state was pure E2. The angular distribution of the radiation with respect to the beam axis is given in table 3. The data in figure 11 was obtained with the 4" x 4" NaI crystal placed 1.06" from the target at 0° with respect to the beam. Rose's smoothing factors appropriate for this geometry are $J_2/J_0 = 0.514$ and $J_4/J_0 = 0.028$. Applying these numbers to the theoretical angular distribution gives a correction factor of 1.25 at 0° that should be divided into the widths given above.

Assuming a spin of 4^+ for the 10.02-Mev level in Ne^{20} also allows the determination of the alpha particle parameters. If all the measured width of this resonance is attributed to the alpha-particle width, the following numbers are obtained:

$$\Gamma_{\alpha} = 155 \pm 30 \text{ kev}$$
$$\theta^2 = 25.4\%$$

8.17-MEV RESONANCE

This resonance is shown on the excitation function for radiation to the ground state and first excited state of Ne^{20} given in figure 12, as a single high point. A separate excitation function run over the region of this resonance in 10 kev steps shows a typical thick target excitation function that rises on the low energy side in less than 10 kev. From this excitation function it is possible to place the resonant energy at 8.17 ± 0.03 Mev, corresponding to a level in Ne^{20} at 11.27 ± 0.03 Mev, and with a resonant width of 4 kev or less in the center of mass.

Gamma-ray spectra obtained at this alpha-particle bombarding energy show the 11.27-Mev transition to the ground state with no clear indication of the possible 9.64-Mev transitions to the first excited state. However even in the best spectrum obtained at this energy, poor statistics prevent the upper limit estimate of the strength of the transition to the first excited state from being set lower than $1/3$ of the transition strength to the ground state. Estimates of the radiative width for the 11.27-Mev transition to the ground state gave $\omega\Gamma_{\gamma} = 0.9 \pm 0.4$ ev, indicating the 9.64-Mev transition to the first excited state has $\omega\Gamma_{\gamma} \lesssim 0.3$ ev. Additional evidence for the validity of the upper limit set on the transition to the first excited state was obtained from coincidence measurements at this energy. A 1000 μC run gave 25 coincidence counts which leads to an upper limit estimate of $\omega\Gamma_{\gamma} \sim 0.4$ ev if all the counts are attributed to the possible 9.64-1.63-Mev gamma-ray cascade.

It is interesting to speculate on the possible spin values for this resonance. The fact that the transition is primarily to the ground state of Ne^{20} limits the possible spin values to 1^- or 2^+ . A 1^- assignment

would probably mean the transition to the ground state is E1, while a 2^+ assignment would mean E2. In either case these transitions are weak, and the parameters would be:

a) 1^- assignment for the 11.27-Mev level

$$\Gamma_{\gamma} = 0.3 \text{ ev}$$
$$|M|^2 = 4.2 \times 10^{-2} \text{ - - for E1}$$

b) 2^+ assignment for the 11.27-Mev level

$$\Gamma_{\gamma} = 0.18 \text{ ev}$$
$$|M|^2 = 0.37 \text{ - - for E2}$$

As mentioned previously, both Butler (37) and Rabson et al. (36) have reported a level in the vicinity of this excitation energy in Ne^{20} from the $\text{F}^{19}(\text{d}, \text{n}\gamma)\text{Ne}^{20}$ reaction. The gamma ray they report is due to a direct transition to the ground state. Davis et al. have also reported a resonance at 8.20-Mev bombarding energy, but assign a resonance width of approximately 125 kev. It seems unlikely that the resonance they report is the resonance reported here.

8.54-MEV RESONANCE

This resonance is seen as a single high point on the excitation function for radiation to the ground state and first excited state of Ne^{20} given in figure 12. The data used to derive this excitation function is the only source of information on this resonance. The resonant energy is 8.54 ± 0.04 Mev, corresponding to a level in Ne^{20} at 11.56 ± 0.04 Mev excitation energy. The uncertainty assigned to the resonance energy corresponds to the 40 kev steps used to cover this energy region. The gamma-ray spectrum obtained at 8.54-Mev bombarding energy shows

the distinct features of a weak 9.94-Mev gamma ray from the transition to the first excited state of Ne^{20} . This gamma ray is clearly absent in the spectra obtained at 8.50- and 8.58-Mev bombarding energy.

Estimates of the radiative width were made by assuming the single high point is the height of a thick target step. Such an assumption gives for the radiative width: $\omega\Gamma_{\gamma} = 0.5 \pm 0.3$ ev. In view of the fact that the excitation function was run in 40 kev steps, and the fact that the tungsten oxide target was 50 kev thick to alpha particles with this energy, a resonance with as much as 15 kev total width might appear as a single high point. This uncertainty, poor statistics, and possible angular distribution effects are the primary sources of the large uncertainty quoted on the number above. There is no evidence for a transition to the ground state, however a width of $\omega\Gamma_{\gamma} \leq 0.2$ ev probably would go undetected.

9.40-Mev Resonance

This resonance is shown on the excitation function for radiation to the ground state and first excited state of Ne^{20} given in figure 12. On the basis of the experimental widths of the yield curves for the 6.93- and 7.94-Mev resonances, the thickness of the target used for the measurement of the excitation function shown in figure 12 was 47 ± 5 kev for alpha particles of this energy. The width of the yield curve for the 9.39-Mev resonance is 68 ± 15 kev at half maximum, indicating a resonance width of 40 ± 16 kev in the center of mass. The maximum yield is at 9.42 Mev, and hence the resonance is located at 9.40 ± 0.04 Mev corresponding to a level in Ne^{20} at 12.25 ± 0.04 Mev.

Gamma-ray spectra obtained at this bombarding energy show the

10.62-Mev transition to the first excited state with no clear indication of a transition to the ground state. Estimates of the radiative width for the transition to the first excited state gave $\omega\Gamma_\gamma = 7 \pm 3$ ev. Transitions to the ground state can not be ruled out due to the summing problem, however a lower limit of $\omega\Gamma_\gamma \leq 1$ ev can be set on this transition. Coincidence measurements made at this energy showed the 10.67-Mev and 1.63-Mev gamma rays, but due to poor statistics, no statement can be made about transitions to low-lying states above the first excited state of Ne^{20} .

Both Butler and Rabson et al. have reported a level in the vicinity of this excitation energy in Ne^{20} from the $\text{F}^{19}(\text{d}, \text{n}\gamma)\text{Ne}^{20}$ reaction. The levels they report decay by the same gamma-ray cascade scheme as noted in this work. Davis et al. have also reported a resonance at 9.42-Mev bombarding energy, but they do not assign a width.

9.57-Mev Resonance

The presence of this resonance on the excitation function for radiation to the ground state and first excited state of Ne^{20} shown in figure 12 is primarily due to pulse pile up of the very intense 6.13-Mev radiation from a resonance in the $\text{O}^{16}(\alpha, \alpha'\gamma)\text{O}^{16}$ reaction at this bombarding energy. Even though the threshold for this reaction is at 7.68 Mev, this is the first strong resonance that has been observed. The fact that the first strong resonance occurs 2 Mev above the threshold is not surprising if one considers the fact that the outgoing, inelastically scattered alpha particle will have only 1.22 Mev in the center of mass, and must penetrate a Coulomb barrier of 4.0 Mev for s-wave alpha particles from O^{16} .

A separate excitation function for the 6.13-Mev radiation is shown in figure 26. The data was obtained from the same data used for the excitation function given in figure 12, and the experimental conditions are given on page 32. The contribution to the yield of 6.13-Mev radiation from the $C^{13}(\alpha, n\gamma)O^{16}$ reaction has been estimated by smoothly matching the excitation function obtained by Spear et al. (11) for this reaction to the data at 9.05 Mev. The crosses in figure 26 are the result of the procedure. As seen in this figure, the width at half maximum for the 9.57-Mev resonance is 74 ± 15 kev. The target thickness at this bombarding energy is 47 ± 5 kev, thus indicating a resonance width of 46 ± 16 kev in the center of mass. The maximum in the yield occurs at 9.57 Mev, placing the resonance at 9.57 ± 0.04 Mev, and corresponding to a level in Ne^{20} at 12.39 ± 0.04 Mev.

The product $(\omega\Gamma_{\alpha}\Gamma_{\alpha'})/\Gamma$ has been computed from the height and the area of the yield curve for the 9.57-Mev resonance. The value obtained was $(\omega\Gamma_{\alpha}\Gamma_{\alpha'})/\Gamma = 3 \pm 1$ kev, where the uncertainty is primarily due to the uncertainty in the width of the resonance. It is possible to restrict the spin values that can be assigned to this level on the basis that the required width for Γ_{α} should not exceed the Wigner single particle limit. By equating Γ_{α} to Γ , one obtains the following table:

J^π	ω	$\Gamma_{\alpha'}$	l^π	$\Gamma_{\alpha'w}$	θ^2
3^-	7	430 ev	0^+	768 ev	56 %
2^+	5	600	1^-	400	150
4^+	9	333	1^-	400	83
1^-	3	1000	2^+	116	860
3^-	7	430	2^+	116	370
5^-	11	272	2^+	116	230
0^+	1	3000	3^-	18.8	15900
2^+	5	600	3^-	18.8	3200
4^+	9	333	3^-	18.8	1800
6^+	13	231	3^-	18.8	1230

In this table, J^π is a possible spin and parity value for the 12.39-Mev level in Ne^{20} , and l is the relative angular momentum (in units of \hbar) with parity π removed by the outgoing inelastically scattered alpha particle. The requirements on J^π and l^π is summarized by the vector equation:

$$\vec{J}^\pi + \vec{l}^\pi = \vec{3}^-$$

The quantity $\Gamma_{\alpha'}$ is the channel width for the inelastically scattered alpha particle, $\Gamma_{\alpha'w}$ is the Wigner single particle limit for alpha particles with this energy (1.22 Mev) and relative angular momentum, l , and θ^2 is the ratio of $\Gamma_{\alpha'}$ to $\Gamma_{\alpha'w}$. As seen in this table, 3^- and 4^+ are distinct possibilities for the spin of the 12.39-Mev level, however 2^+ and 5^- can not be entirely ruled out in view of the large uncertainty in the quantity $(\omega\Gamma_{\alpha'}\Gamma_{\alpha'})/\Gamma$. The preliminary data of Davis et al. on the elastic scattering of alpha particles on O^{16} shows evidence for a resonance at this bombarding which is seen to vanish at 90° and

140.8° in the center of mass indicating the spin is 3⁻.

Radiative transitions from the 12.39-Mev level in Ne²⁰ to the first excited state and ground state are difficult to estimate due to the pulse pile-up from the intense 6.13-Mev radiation. Crude estimates give:

$$\begin{aligned} \omega\Gamma_{\gamma} &= 3.5 \pm 2 \text{ ev} && - \text{ first excited state} \\ \omega\Gamma_{\gamma} &\leq 1 \text{ ev} && - \text{ ground state} \end{aligned}$$

The ground state radiative width is given in the form of an upper limit since it is possible to attribute all the counts seen in the gamma-ray spectra in the energy region of the 12.39-Mev photo peaks to pulse pile-up. Similar problems were encountered in making the estimate for the radiative width to the first excited state, but a comparison of two runs made at 9.59-Mev bombarding energy with beam currents that differed by a factor of two showed that not all of the counts were due to pulse pile-up. A coincidence measurement made at this energy did not yield sufficient counts to give a recognizable spectrum, but if all the coincidence counts obtained are attributed to the 10.76- and 1.63-Mev cascade gamma rays, a value of $\omega\Gamma_{\gamma} = 3.6$ is obtained for this transition.

In the excitation function for 6.13-Mev radiation for $O^{16}(\alpha, \alpha'\gamma)O^{16}$ shown in figure 26, a small bump is seen at 9.25-Mev bombarding energy. This bump is reproducible, and probably is due to a resonance in $O^{16}(\alpha, \alpha'\gamma)O^{16}$ reaction, and would correspond to a level in N²⁰ at 12.13 ± 0.04 Mev. The area under this bump indicates a value for the quantity $(\omega\Gamma_{\alpha}\Gamma_{\alpha'})/\Gamma = 100 \pm 50$ ev. Arguments based on the size of the Wigner single particle limit are of no assistance in limiting the

possible spin values for this resonance due to the small size of the quantity $(\omega\Gamma_a\Gamma_{a'})/\Gamma$.

IV. SUMMARY

The results from this experiment are summarized in table 1 and table 2. The final state parameters listed in table 1 have been taken from Lauritsen and Ajzenberg-Selove (4) and the spin and parity assignments for the 9.48- and 10.02-Mev levels are based on the experiments of McDermott et al. (28) and Davis et al. (29). Otherwise the data in this table is from this experiment. The isotopic spin assignments that have been made are based on the assumption that the 10.270-Mev level is the first $T = 1$ level in Ne^{20} . Table 2 lists the alpha-particle parameters for those resonances in table 1 for which the spin of the corresponding level in Ne^{20} is known.

In figure 27, the energy level diagram of F^{20} has been adapted from Lauritsen and Ajzenberg-Selove and so arranged that the ground state corresponds in energy to the analog state in Ne^{20} at 10.270 Mev. This arrangement shows that with the single exception of the 12.39-Mev level found in the inelastic scattering of alpha particles on O^{16} , each Ne^{20} level found in this experiment agrees in energy with a level in F^{20} . Such agreement makes it tempting to assume that these levels are analogs; however more experimental information is necessary before such conclusions can be drawn.

Some systematic behavior can be seen in the data of table 1. The two stronger resonances in the capture reaction are for magnetic dipole transitions between states that differ by one unit in their isotopic spin quantum number. Several of the E2 transitions are approximately seven times stronger than the single particle limit. Even though the single

particle limit is proportional to the fourth power of the radius, it is necessary to increase the radius of Ne^{20} from 3.25 Fermis used for the calculations to roughly 5.3 Fermis before the single particle estimate would produce the factor of seven. Since such a radius seems unreasonably large, these enhanced radiative widths for the E2 transitions indicate that collective effects are important even at these relatively high excitation energies. Electric quadrupole radiative widths in excess of the single particle limit have been noted in a number of other transitions in the light nuclei (43), and typical strengths are roughly 1 to 30.

The principal result of this experiment is the location and identification of the first $T = 1$ level in Ne^{20} at 10.27 Mev. The $T = 1$ assignment was made on the basis of the excitation energy, the fact that the 2^+ spin of this level is the same as the ground state of F^{20} , and the large radiative width for the M1 transition to the first excited state of Ne^{20} . Since such an assignment implies this level is quite similar in structure to the F^{20} ground state, it then becomes interesting to make a comparison of the M1 decay of the 10.27-Mev level in Ne^{20} with the allowed Gamow-Teller beta decay of the F^{20} ground state. The only difficulty is obtaining a suitable model. At present, no complete intermediate-coupling shell model calculations have been made for the mass 20 system. The difficulty with such calculations is the evaluation of a large number of radial integrals describing possible residual interactions in the (2s,1d) shell. Efforts to bypass these integrals by describing the low-lying levels of Ne^{20} by simple configurations in this shell led

Elliott and Lane (61) to the conclusion that it is important to include all configurations. The unified model of Bohr and Mottelson offers at least an approximate method of treating the residual interactions by the introduction of a permanently deformed well. This model has had success in describing nuclei in this mass region, and in view of recent success of Litherland et al. (2) with the application of this model to the low-lying, $T = 0$, levels of Ne^{20} , it seems rather natural to assume the model will offer a good description of the $T = 1$ levels in Ne^{20} or the low-lying levels of F^{20} and Na^{20} .

A calculation comparing the allowed Gamow - Teller beta decay of the F^{20} ground state to the M1 decay of the 10.27-Mev level of Ne^{20} is given in Appendix B. At best, the calculation is premature. A paucity of information about the character of the excited states of F^{20} and the $T = 1$ levels in Ne^{20} above the 10.27-Mev level makes it impossible to argue, even qualitatively, that the unified model is applicable. There is no indication that these levels have even the $I(I+1)$ spacing of a rigid rotor. However, by making some "hopefully-reasonable" guesses for unknown parameters, an interesting, qualitative picture is obtained from the unified model. The very slow ($\log ft = 4.99$) but allowed Gamow-Teller beta decay of the F^{20} ground state (52) is a natural consequence of the K selection rule of this model. However the strong M1 decay of the 10.27-Mev level is not so easily explained, and the estimate of this strength based on the $\log ft$ value of the beta decay is low by a factor of three. Probably this is not poor agreement in view of the uncertainties. Finally it is tempting to put the 4^+ , $T = 1$, level of Ne^{20}

at 11.08 Mev into a rotational band based on the 2^+ , 10.27-Mev level. However, the calculations in Appendix B indicate these levels are much too close in energy to be related in this fashion. The question this raises, of course, is just how many bands will be necessary to describe the $T = 1$ levels in Ne^{20} or the low-lying levels of F^{20} or Na^{20} .

While unobserved transitions usually deserve no additional comment, the possible E1 gamma-ray transition from the 10.27-Mev level to the 4.97-Mev level in Ne^{20} (see figure 1) should be mentioned once again because of the possible astrophysical importance of the 4.97-Mev level. This level lies just above the $\text{O}^{16} + \alpha$ threshold in Ne^{20} , and in the past it has been suggested (62) that it may play an important role in the formation of Ne^{20} in the interior of helium burning stars. However recent measurements (63) have shown the spin and parity of the 4.97-Mev level is 2^- hence forbidding the formation of this level by $\text{O}^{16} + \alpha$. The fact that the expected E1 transition from the 10.27-Mev level to the 4.97-Mev level is much weaker than the Weisskopf single particle estimate (with a ratio of $|M|^2 < 6 \times 10^{-3}$) is surprising, however this limit is not small enough to throw doubt on the 2^- assignment for the 4.97-Mev level.

APPENDIX A

Angular Distribution Considerations

In this appendix the theoretical angular distribution and angular correlation formulas that have been used in this experiment will be presented, and a discussion will be given of the modifications introduced in these formulas by the finite size of the NaI(Tl) detectors.

A.1. Theoretical Formulas

The theory of angular correlations of nuclear radiations is an important facet of nuclear spectroscopy, and the subject has been treated in some detail in a number of excellent reviews (64, 65). Tables have been prepared for the explicit purpose of expediting the calculation of angular correlation functions, and several authors (66, 67) present articles with detailed instructions for the use of these tables. One of the clearer demonstrations of the modern techniques of using density matrices and statistical tensors for the derivation of correlation functions is given by Wiedenmüller (68), who derives a "master formula" that gives the statistical tensor for the residual nucleus in terms of the statistical tensors for the initial state and the outgoing radiation. Similar formulas may be obtained from the review article of Devons and Goldfarb (65). It is probably worth noting that Wiedenmüller's definition of a statistical tensor differs from the definition given by Devons and Goldfarb, and one should take care not to go from one formulation to the other indiscriminately.

The formulas listed below have been derived with a master

formula similar to that of Wiedenmüller's but for statistical tensors defined in the same fashion as given by Devons and Goldfarb. For a problem as simple as the alpha-capture by O^{16} , the master formula can be used directly to give the angular distribution of outgoing gamma radiation with respect to the beam axis. This formula is:

$$W(\theta) \approx \sum_{KLL'} (-1)^{\{(2L+1)(2L'+1)\}^{1/2}} (J_1 0, J_1 0 | K 0) \\ \times (L 1, L 1 | K 0) W(J_1 J_1 L L'; K J_2) P_K(\cos \theta) \\ \times \langle J_1 || T_L || J_2 \rangle \langle J_1 || T_{L'} || J_2 \rangle^*$$

where

J_1 = spin of the initial state formed by the alpha capture reaction

L, L' = angular momentum removed by the outgoing gamma ray

J_2 = final state spin

θ = angle between the gamma-ray direction and the beam direction

$\langle J_1 || T_L || J_2 \rangle$ = reduced matrix element for the multipole operator T_L

$(J_1 M_1, J_2 M_2 | J_3 M_3)$ = Clebsch-Gordon coefficient that adds J_1 to J_2 to give J_3

$W(J_1 J_1 L L'; K J_2)$ = Racah coefficient.

Some computation convenience is achieved by introducing the Z_1 coefficient of Sharp et al. (69), in this case one obtains:

$$W(\theta) = \sum_{KLL'} (-1)^{K/2} \langle J_1 0, J_1 0 | K 0 \rangle Z_1 (L J_1 L' J_1; J_2 K) \\ \times P_K(\cos \theta) \langle J_1 || T_L || J_2 \rangle \langle J_1 || T_{L'} || J_2 \rangle^*$$

Numerical formulas for the angular distribution of gamma radiation with respect to the alpha-particle beam direction for pure multipole transitions to the ground state and first two excited states of Ne^{20} are given in table 3. In this table, the angular distribution functions have been normalized to the form:

$$W(\theta) = 1 + a_2 P_2(\cos \theta) + a_4 P_4(\cos \theta)$$

in which case the number of gamma rays at angle θ , $N(\theta)$, in solid angle $d\Omega$ is given in terms of the source strength N by:

$$N(\theta) = \frac{N}{4\pi} (1 + a_2 P_2(\cos \theta) + a_4 P_4(\cos \theta))$$

The numerical values in table 3 have been checked in all cases with values obtained from the formulas and tables of Sharp et al. (69), and most cases have been compared with formulas obtained from the tables of Biedenharn and Rose (64).

The specific formulas for transitions involving mixed gamma ray multipoles are too extensive to warrant treatment here. The numerical formulas, given in the text as needed, have been derived from the general formulas above. In these cases it is not possible to factor out the constant reduced matrix elements, and as a result an additional parameter, the mixing coefficient δ or the ratio of the two reduced matrix elements, is introduced in the formulas. For the two examples

in the text:

$$\delta = \frac{\langle J_1 || E2 || J_2 \rangle}{\langle J_1 || M1 || J_2 \rangle}$$

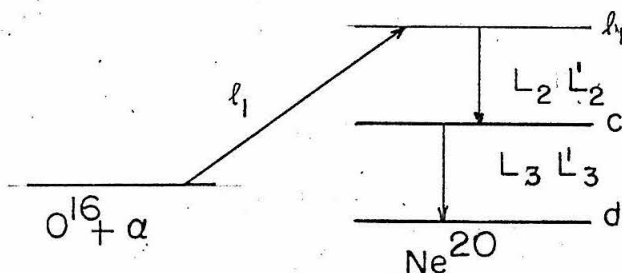
where $\langle J_1 || E2 || J_2 \rangle$ and $\langle J_1 || M1 || J_2 \rangle$ are the reduced matrix elements for the electric quadrupole and magnetic dipole transitions respectively. The transition rates or radiative widths are proportional to the reduced matrix elements squared, hence to δ^2 . By suitable phasing of the nuclear wave functions, the reduced matrix elements may be made real (47), in which case δ is either positive or negative. Physical significance can be attached to the sign of δ only in regards to a specific nuclear model, and in such cases positive δ corresponds to the phasing of the matrix elements of Blatt and Weisskopf (70), and the usual definition of the reduced matrix elements:

$$\langle J_1 M_1 | T_{LM} | J_2 M_2 \rangle = (J_2 M_2, L M | J_1 M_1) \langle J_1 || T_L || J_2 \rangle$$

where T_{LM} is one of the multipole operators.

Formulas for triple angular correlations involving the incident alpha particle and two outgoing cascade gamma rays are derived by a continuation of the process used to obtain a single cascade formula.

For a cascade of the form



where ℓ_1 , c , and d are the initial state, intermediate state and final state respectively, and where L_2, L_2' and L_3, L_3' represent the multipolarity of the first and second cascade gamma rays. The general formula has the same form as the single cascade formula being a sum over angular dependent terms each of which is multiplied by a coefficient. The formula used was:

$$W(\theta_2\phi_2, \theta_3\phi_3) = \sum_{\substack{K_1 K_2 K_3 \\ L_2 L_2' \\ L_3 L_3'}} C(\ell_1, c, d; L_2, L_2'; L_3, L_3'; K_1, K_2, K_3) \times \Lambda_{K_1 K_2 K_3}(\theta_2\phi_2, \theta_3\phi_3)$$

where the coefficient is:

$$\begin{aligned} & C(\ell_1, c, d; L_2, L_2'; L_3, L_3'; K_1 K_2 K_3) \\ &= [(2\ell_1+1)^4 (2K_3+1)(2K_2+1)(2L_2+1)(2L_2'+1)(2L_3+1)(2L_3'+1) \\ & \quad \times (2c+1)^2]^{1/2} (-1)^{\ell_1 + L_2' + d + K_3 - c} (\ell_1 0, \ell_1 0 | K_1 0) \\ & \quad \times (L_2 1, L_2' - 1 | K_2 0) (L_3 1, L_3' - 1 | K_3 0) (K_3 0, K_2 0 | K_1 0) \\ & \quad \times W(c c L_3 L_3'; K_3 d) \left\{ \begin{matrix} \ell_1 & c & L_2 \\ \ell_1 & c & L_2' \\ K_1 & K_3 & K_2 \end{matrix} \right\} \langle \ell_1 || L_1 | c \rangle \\ & \quad \times \langle \ell_1 || L_1' || c \rangle^* \langle c || L_2 || d \rangle \langle c || L_2' || d \rangle^* \end{aligned}$$

where the term, $\left\{ \right\}$ is a 9-J symbol. The angular dependent functions for the general case are:

$$\begin{aligned} \Lambda_{K_1 K_2 K_3}(\theta_2 \phi_2, \theta_3 \phi_3) &= \frac{1}{(K_3 0, K_2 0 | K_1 0)} \sum_M (K_3 M, K_2 - M | K_1 0) \\ &\quad \times \left(\frac{4\pi}{2K_3 + 1} \right)^{1/2} Y_{K_3}^{+M}(\theta_3 \phi_3) \left(\frac{4\pi}{2K_2 + 1} \right)^{1/2} Y_{K_2}^{-M}(\theta_2 \phi_2) \end{aligned}$$

where the $Y_K^M(\theta\phi)$ are spherical harmonics. The angles θ_2, ϕ_2 referring to the first gamma ray, are the Euler angles describing the rotation ϕ_2 about the beam axis or the original Z-axis, followed by a rotation θ_2 about the new Y-axis such that the new Z-axis is in the direction of the detector. Angles θ_3, ϕ_3 for the second gamma ray are defined in the same fashion. For the experimental arrangement of two coplanar detectors on opposite sides of the beam direction, the angular functions reduce to:

$$\begin{aligned} \Lambda_{K_1 K_2 K_3}(\theta_2 \phi_2) &= \frac{1}{(K_3 0, K_2 0 | K_1 0)} \sum_{M \geq 0} (2 - \delta_M^0) \left(\frac{(K_3 - M)!}{(K_3 + M)!} \right)^{1/2} P_{K_3}^M(\cos \theta_3) \\ &\quad \times \left(\frac{(K_2 - M)!}{(K_2 + M)!} \right)^{1/2} P_{K_2}^M(\cos \theta_2) (K_3 M K_2 - M | K_1 0) \end{aligned}$$

where the angles θ_2 and θ_3 are measured with respect to the beam axis. If the correlation function is normalized so the coefficient of the first term Λ_{000} , is unity, then the pairs of coincidence gamma rays with the first gamma ray going into solid angle $d\Omega_2$ at θ_2, ϕ_2 and with the second gamma ray going into solid angle $d\Omega_3$ at θ_3, ϕ_3 are given

in terms of the source strength N by:

$$N(\theta_2\phi_2, \theta_3\phi_3) = \frac{N}{(4\pi)^2} W(\theta_2\phi_2, \theta_3\phi_3) d\Omega_2 d\Omega_3$$

Even restricting the discussion to dipole and quadrupole transitions, as many as nineteen coefficients and angular functions may appear in a correlation function. For this reason the correlation functions have been computed with the aid of a high speed computer. Values obtained in this way have been compared with hand calculated values, and compared with correlation functions computed from the tables of Ferguson and Rutledge (71) wherever possible.

A. 2. Smoothing Factors and the Collimator Geometry

The discussion of angular distributions and correlation functions given above would be sufficient for gamma-ray detectors of no physical extent. For a detector geometry employing large cylindrically shaped NaI detectors whose axes of symmetry pass through the target spot, the experimental angular distribution or triple angular correlation functions may be obtained from the functions for point detectors using a technique described by Rose (39). The essence of the technique is the expression of the angular parts of the correlation by a new set of angular functions based on a coordinate system coinciding with the axis of symmetry of the NaI detector. While it might appear off-hand as if little could be gained by this change, integrals over the volume of the gamma-ray detector in this new coordinate system are performed more easily and the final correlation functions obtained are the same as the point counter functions with only minor changes.

By way of illustration, consider the form of the angular distribution function that gives the number of gamma rays in $d\Omega$ at θ' with respect to the beam axis from a source of strength N :

$$N(\theta') = \frac{N}{4\pi} \sum_{\ell} a_{\ell} P_{\ell}(\cos \theta) \quad \text{with } a_0 = 1$$

Expressing this distribution in terms of a coordinate system based on the symmetry axis of the crystal gives:

$$N(\theta') = \frac{N}{4\pi} \sum_{\ell} a_{\ell} \sum_{M} \left(\frac{4\pi}{2\ell+1}\right) Y_{\ell}^{M*}(\theta_1, \phi_1) Y_{\ell}^M(\theta_2, \phi_2)$$

where the $Y_{\ell}^M(\theta, \phi)$ are spherical harmonics. The angles θ_1, ϕ_1 and θ_2, ϕ_2 are the coordinates of the beam direction and the gamma ray direction respectively in the new coordinate system and they form a spherical triangle with:

$$\cos \theta' = \cos \theta_1 \cos \theta_2 + \sin \theta_1 \sin \theta_2 \cos(\phi_1 - \phi_2)$$

The number of gamma rays that will be detected in the NaI crystal is given by the integral:

$$\int_{\text{Crystal}} N(\theta') \times (\text{probability of detection}) d\Omega$$

where the probability of detection depends only on the polar angle θ_2 in the new coordinate system. Performing this integral gives:

$$\text{counts at angle } \theta' = \frac{N}{4\pi} 2\pi \sum_{\ell} a_{\ell} P_{\ell}(\cos \theta_1) J_{\ell} \quad \text{with } a_0 = 1$$

The quantities J_ℓ are defined by the integral:

$$J_\ell = \int_{\text{Crystal}} P_\ell(\cos \theta_2) (1 - e^{-\mu \ell(\theta_2)}) \sin \theta_2 \, d\theta_2$$

where

μ = linear attenuation coefficient for the gamma ray
in NaI

$\ell(\theta_2)$ = path length at angle θ in the NaI crystal.

The term $\frac{1}{2} J_0$ is the efficiency integral and:

$$\text{counts at angle } \theta' = N \times (\text{efficiency}) \times \sum_\ell a_\ell \frac{J_\ell}{J_0} P_\ell(\cos \theta_1)$$

where θ' and θ_1 are the same angle. Quite similar arguments give the following form for the triple angular correlation formulas:

$$\begin{aligned} (\text{coincidence counts at angles } (\theta_2, \theta_3)) &= N \times (\text{efficiency of counter \#1}) \times (\text{efficiency of counter \#2}) \\ &\times \sum_{K_1 K_2 K_3} a_{K_1 K_2 K_3} \frac{J_{K_2}(\#1)}{J_0(\#1)} \times \frac{J_{K_3}(\#2)}{J_0(\#2)} \Lambda_{K_1 K_2 K_3}(\theta_2, \theta_3) \end{aligned}$$

$$\text{with } a_{000} = 1$$

where the first gamma ray at angle θ_2 is detected in counter #1 having integral factors $J_{K_2}(\#2)$, and where the second gamma ray at angle θ_3 is detected in counter #2 having integral factors $J_{K_3}(\#3)$.

The ratios J_ℓ/J_0 appearing in the correlation formulas for detectors with a finite size are known as Rose's smoothing factors.

Since they are always smaller than one the angular distribution patterns measured with large counters are attenuated or "smoothed out" when compared to measurements made with smaller counters. The attenuation problem can be serious, and for example the 4" x 4" NaI crystal used in this experiment is practically incapable of detecting $P_4(\cos \theta)$ terms in angular distributions from gamma-ray sources 1" or closer to the face of the crystal. The angular resolution of such a crystal may be enhanced by placing it some distance from the target, or by installing a collimator. The second method was chosen for this experiment, and a typical target-collimator-NaI(Tl) detector geometry is shown in figure 28. For this geometry, Rose's smoothing factors are given by:

$$J_\ell = \int_{\text{Crystal}} P_\ell(\cos \theta) e^{-\mu_1 \ell_1(\theta)} (1 - e^{-\mu_2 \ell_2(\theta)}) \sin \theta \, d\theta$$

where

μ_1 = linear attenuation coefficient for the gamma ray
in lead

$\ell_1(\theta)$ = path length in the lead collimator at angle θ

μ_2 = linear attenuation coefficient for the gamma ray
in NaI

$\ell_2(\theta)$ = path length in the NaI crystal at angle θ

where the angle θ is measured with respect to the axis of symmetry of the NaI crystal.

The collimator geometry was chosen instead of an open crystal some distance from the target since it is known that such geometries

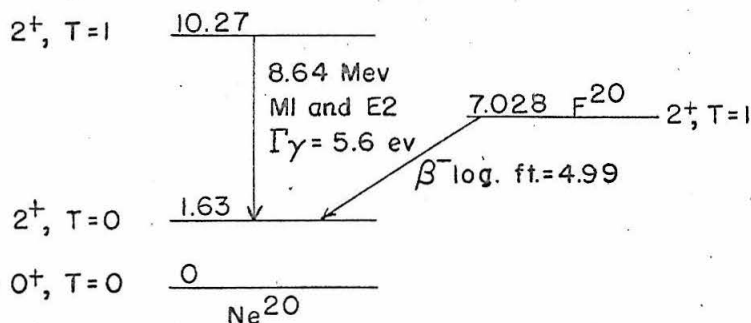
increase the photo-fractions of the gamma ray spectra (15). This choice seems to have been fortunate. Recent measurements and calculations by Twin and Willmott (72) indicate that the ratios J_{ℓ}/J_0 for the full energy peak alone in a bare 5" x 4" NaI are closer to unity than indicated by the calculated smoothing factors for the complete gamma-ray spectrum. For gamma-rays in the 4 to 8-Mev range, they quote $\sim 5\%$ for $P_2(\cos \theta)$ and $\sim 20\%$ for $P_4(\cos \theta)$ increase over the calculated values at 8 cm between source and detector. The cause of this phenomena is an increase in the loss of secondary gamma rays and electrons through the sides of the crystal for primary events occurring near one of the surfaces of the NaI crystal. Hence the probability for producing full energy events in the crystal decreases more rapidly with the angle θ than the probability for detecting the gamma ray. Several factors make such effects less important to the measurements in this experiment. Gamma rays were kept away from the wings of the NaI by the collimator, and larger spectrum fractions (approximately 50% of the total) were used for angular distribution measurements. In any event the conclusions drawn on information obtained from angular distribution measurements in this experiment were based primarily on $P_2(\cos \theta)$ terms where the error incurred would be small even for an uncollimated crystal.

Appendix B

In this appendix, a comparison of the F^{20} ground state beta decay with the M1 gamma-ray decay of the 10.27-Mev level in Ne^{20} will be made with the unified model of Bohr and Mottelson (73, 74) using Nilsson (75) wave functions for the intrinsic states of this model. There are difficulties with this comparison due to the fact that there are too many parameters for the amount of experimental data that is presently available. However it is possible to assign reasonable values to some of these parameters, and then present the results as a graph plotted against the remaining parameters.

B1. Experimental Data

The experimental data for the decay of the 10.27-Mev level in Ne^{20} , and the F^{20} beta decay is summarized in the following energy level diagram:



The theoretical radiative width for a gamma-ray transition of multipole order λ and energy E is given by:

$$\Gamma = \frac{8\pi(\lambda + 1)}{\lambda [(2\lambda + 1)!!]^2} \left(\frac{E}{\hbar c} \right)^{2\lambda+1} B(\lambda)$$

$B(\lambda)$ is defined in terms of the matrix element between initial and final states for the multipole operator:

$$B(\lambda) = \sum_{\mu, M_f} |\langle f | M_{\lambda\mu}(\vec{X}) | i \rangle|^2$$

where μ and M_f are the magnetic quantum numbers of λ and the final state spin. For magnetic dipoles, the operator $M_{1\mu}(\vec{X})$ is:

$$M_{1\mu} = \left(\frac{3}{4\pi}\right)^{1/2} \left(\frac{e\hbar}{2Mc}\right) \sum_{i=1}^A (g_l^i \ell_{1\mu}^i + g_s^i S_{1\mu}^i)$$

where $\ell_{1\mu}^i$ and $S_{1\mu}^i$ are the orbital angular momentum and spin operators for the i^{th} particle respectively. The gyromagnetic factors, g , are:

protons:	$g_l = 1$	$g_s = 5.587$
neutrons:	$g_l = 0$	$g_s = -3.826$

For electric quadrupole radiation, the operator is:

$$Q_{2\mu} = e \sum_{i=1}^Z (r^i)^2 Y_2^\mu(\vec{\theta}_i)$$

where the sum in this case is only over proton states. The multipole operators given above are those of Blatt and Weisskopf (70).

For allowed Gamow-Teller beta decay, the ft value is given by (74):

$$ft = \frac{2740}{0.61 \times 4 \times B_{GT}} = \frac{1122}{B_{GT}}$$

where B_{GT} is defined by:

$$B_{GT} = \sum_{\mu M_f} | \langle f | \sum \tau_+ S_{1\mu}^i | i \rangle |^2$$

The operator, τ_+ , changes a neutron state to a proton state.

For comparison with the theoretical estimates of the transition rates, it is convenient to remove the dimensioned factors and constant numerical values from the matrix elements. The radiative widths for an 8.64-Mev gamma ray in terms of this dimensionless reduced transition probability B' are:

$$\Gamma(M1) = 1.778 B'(M1) \text{ (ev)}$$

$$\Gamma(E2) = 0.0389 B'(E2) \text{ (ev)}$$

The operators for B' are:

$$M_{1\mu}^i = \sum_{i=1}^A (g_\ell^i \ell_{1\mu}^i + g_s^i S_{1\mu}^i)$$

$$Q_{2\mu}^i = \sum_{i=1}^Z (r^i)^2 Y_2^\mu(\vec{\theta}_i)$$

$$(GT)_{1\mu} = \sum_{i=1}^A \tau_+^i S_{i\mu}^i$$

Hence the experimental values indicated in the energy level diagram give the following values for the B' :

$$\pm (B'(M1))^{1/2} = 1.773 \pm 0.095$$

$$\pm (B'(E2))^{1/2} = (8.84 \begin{matrix} + 6.36 \\ - 5.58 \end{matrix}) \times 10^{-2} \text{ or zero}$$

$$\pm (B'(GT))^{1/2} = 0.107$$

The large range on the E2 value is due to the fact that this value was derived from the angular distribution pattern of the 8.64-Mev gamma ray. The same angular distribution pattern also requires the phase of $(B'(M1))^{1/2}$ and $(B'(E2))^{1/2}$ be the same

B. 2. Wave Functions

The unified model finds application in the description of nuclei which have acquired non-spherical shapes. In a coordinate system (X', Y', Z') fixed in the nucleus, the usual assumptions about the nuclear shape are axial symmetry about the Z' axis, and reflection symmetry through the $Z' = 0$ plane. One of the prominent features of the model is the introduction of an additional quantum number K that is the projection of the total angular momentum I on the Z' axis. Wave functions are given by specifying I , M (the projection of I on the space fixed axis, Z''), K , and the wave function χ_K of the intrinsic structure of the nucleus. These wave functions have the form:

$K \neq 0$

$$|IMK\rangle = \left(\frac{2I+1}{16\pi}\right)^{1/2} \left(\chi_K(\vec{X}') D_{MK}^I(\vec{\theta}_i) \right. \\ \left. + (-1)^{I+K} D_{M, -K}^I(\vec{\theta}_i) R_{Y'(\pi)} \chi_K(\vec{X}') \right)$$

$K = 0$

$$|IMK\rangle = \left(\frac{2I+1}{8\pi}\right)^{1/2} \left(\chi_0(\vec{X}') D_{M,0}^I(\vec{\theta}_i) \right)$$

The $D_{MK}^I(\vec{\theta}_1)$ are the wave functions of the symmetric top where the $\vec{\theta}_1$ are the Euler angles that specify the orientation of the nucleus with respect to the space fixed axis, (X'', Y'', Z'') . The second term in the wave functions for $K \neq 0$ is a symmetrizing term included to give this wave function a definite parity, in this case, the parity of χ_K . The operator $R_{Y',(\pi)}$ rotates χ_K by π about the Y' axis.

Holding K and χ_K fixed, one finds these wave functions apply to a series of levels, or a band, that has the spin sequence:

$$K \neq 0$$

$$I = K, K + 1, K + 2, \text{ etc.}$$

$$K = 0$$

$$I = 0^+, 2^+, 4^+, \text{ etc.}$$

or

$$I = 1^-, 3^-, 5^-, \text{ etc.}$$

The energies of these levels are:

$$E(I) = E_{\text{intr.}} + \frac{\hbar^2}{2\mathcal{J}_{X'}} (I(I+1) - K^2)$$

where $\mathcal{J}_{X'}$ is the moment of inertia of the nucleus around the X' axis.

The first three levels of Ne^{20} are 0^+ , 2^+ , and 4^+ with a spacing that indicates $\hbar^2/2\mathcal{J}_{X'} = 0.27$ Mev. In this calculation it will be assumed that the 2^+ ground state of F^{20} , and 2^+ , $T = 1$, 10.27-Mev level in Ne^{20} are the beginning of a $K = 2$ band with members, 2^+ , 3^+ , etc. There is a complication in the calculation. The K quantum numbers for the initial and final states connected by a tensor operator of rank λ must satisfy:

$$|K_i - K_f| \leq \lambda$$

For the magnetic dipole and allowed Gamow-Teller beta decay, $\lambda = 1$, and hence the simple wave functions suggested above would have neither of these vector operators connecting them.

The standard method of circumventing this K selection rule is to mix bands with different K into the wave functions describing the initial and final states. Fortunately the model readily provides the mechanism for the mixing in a Coriolis type of interaction between the particle motion and the slow rotation of the nucleus. Usually this interaction is referred to as R.P.C. (rotation-particle coupling), and it serves to mix bands that differ by one in the K quantum number. The program for this calculation is first to find suitable bands for mixing in the ground state bands of Ne^{20} and F^{20} , and then to calculate the matrix elements for the various possible transitions.

The intrinsic wave functions, χ_K , for Ne^{20} and F^{20} will be constructed from Nilsson single particle wave functions, χ_Ω , for the four particles outside the O^{16} core. These single particle wave functions are eigenfunctions for a harmonic oscillator potential with the spin orbit and l^2 terms of the shell model, and an additional quadrupole term in the potential. The parameters for the potential have been chosen so the predicted energy levels correspond to those of the shell model when the quadrupole term is zero. The size of the quadrupole term is given by the deformation parameter η , which is primarily a measure of the variation of the nuclear radius. In the notation of Nilsson (75):

$$\eta \approx - \frac{2\hbar \omega_0 \delta}{C}$$

where:

$$\delta = \frac{\Delta R}{R} = 0.281$$

$$\Delta R = R_{Z''} - R_{X''}$$

$$R = \text{average radius} = 1.45 A^{1/3} \times 10^{-13} \text{ cm}$$

$$C = \text{size of the spin-orbit potential} = - 2 \text{ Mev}$$

$$\hbar \omega_0 = 15.4 \text{ Mev}$$

The size of the spin orbit potential has been deduced from the $d_{3/2} - d_{5/2}$ splitting in O^{17} (61). For the term $\hbar \omega_0$ Nilsson suggests:

$$\hbar \omega_0 = \frac{41}{A^{1/3}} = 15.1 \text{ Mev}$$

which agrees well with the value of $\langle r^2 \rangle$ in the s-d shell which gives:

$$\hbar \omega_0 = \frac{115}{A^{2/3}} = 15.7 \text{ Mev}$$

The term δ has been derived from the radiative width of the E2 transition from the 2^+ first excited state to the 0^+ ground state of Ne^{20} (32) with the aid of the formula given by Mottelson and Nilsson (76) for the static quadrupole moment. In this calculation, it will be assumed the value of η also applies to the ground state band of F^{20} and to the mirror levels of this band in Ne^{20} .

The actual single particle wave functions, χ_{Ω} , are given by Nilsson in terms of expansion coefficients of the $l - S$ representation:

$$\chi_{\Omega} = \sum_{\ell \Lambda} a_{\ell \Lambda} |N \ell \Lambda S \Sigma \rangle \quad \text{where } \Omega = \Lambda + \Sigma$$

The quantum number N is the total number of oscillator quanta, ℓ is the orbital angular momentum with projection Λ , and S is the spin quantum number with projection Σ . Nilsson abbreviates the quantum numbers by omitting S , which is always $1/2$, and writing $+$ to signify a $+1/2$ projection of S and $-$ for a $-1/2$ projection. The particular terms for Nilsson orbits #6 and #7 which will be used in the following calculations will be written as:

Orbit #6

$$\chi_{\Omega} = (\frac{1}{2} +) = a_1 |2 2 0 + \rangle + b_1 |2 0 0 + \rangle + c_1 |2 2 1 - \rangle$$

Orbit #7

$$\chi_{\Omega} = (\frac{3}{2} +) = a_2 |2 2 1 + \rangle + b_2 |2 2 2 - \rangle$$

For $\eta > 0$, the numerical values for the expansion coefficients are:

η	a_1	b_1	c_1	a_2	b_2
6	0.805	0.533	0.262	0.978	0.207
4	0.786	0.520	0.336	0.967	0.257
2	0.787	0.396	0.472	0.943	0.331

The unit of length for these wave functions is given in terms of

$$(\hbar/M\omega_0)^{1/2} = 1.64 \times 10^{-13} \text{ cm.}$$

Wave functions for particles having a negative projection are obtained by applying the rotation operator $R_{Y_1}(\pi)$ to the positive projection

wave function. The values are:

$$R_{Y_1}(\pi) \left(\frac{1}{2} + \right) \equiv \left(\frac{1}{2} - \right) = - \{ a_1 | 2 2 0 - \rangle + b_1 | 2 0 0 - \rangle + c_1 | 2 2 -1 + \rangle \}$$

$$R_{Y_1}(\pi) \left(\frac{3}{2} + \right) \equiv \left(\frac{3}{2} - \right) = + \{ a_2 | 2 2 -1 - \rangle + b_2 | 2 2 -2 + \rangle \}$$

The phases are determined by the equation (75):

$$R_{Y_1}(\pi) | N \ell \Lambda S \Sigma \rangle = (-1)^{\ell + \Lambda + S + \Sigma} | N \ell -\Lambda S -\Sigma \rangle$$

Nilsson orbit #6 lies below #7 in energy for prolate deformations ($\eta > 0$), and putting the two neutrons and two protons outside the O^{16} core in this orbit gives the Ne^{20} ground state. Since the exclusion principle requires like particles to have opposite projections, Ω , the sum of these projections, K , is zero for the Ne^{20} ground state. Hence one obtains the $K = 0$ band for the first three levels of Ne^{20} . These four particles fill this orbit; additional particles would go into Nilsson orbit #7.

For the three neutrons and one proton of the F^{20} ground state, one of the neutrons has to be put in orbit #7. The sum of the possible projections, Ω , give the following K values:

$$K = 2 = \text{neutrons } \left(+\frac{3}{2} + \frac{1}{2} - \frac{1}{2} \right) + \text{proton } \left(+\frac{1}{2} \right)$$

$$K = 1 = \text{neutrons } \left(+\frac{3}{2} + \frac{1}{2} - \frac{1}{2} \right) + \text{proton } \left(-\frac{1}{2} \right)$$

As far as the Nilsson model is concerned, these two bands would be degenerate in energy; however in practice the former, or the maximum K

value, is the ground state (77). The indicated $K = 1$ band is the band that will be mixed into the two ground bands to provide the observed $M1$ and allowed Gamow-Teller decays.

Slater determinants for these bands will be constructed from the four single particle wave functions. The following notation will be used:

$P(\frac{1}{2} +)_1$ = particle 1, a proton, in Nilsson orbit #6 with a positive projection, $\Omega = +\frac{1}{2}$

$N(\frac{3}{2} -)_3$ = particle 3, a neutron, in Nilsson orbit #7 with a negative projection, $\Omega = -\frac{3}{2}$.

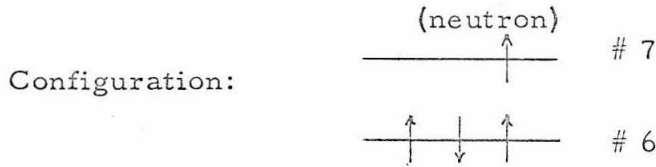
1. Ne^{20} ground state band, $K = 0, T = 0, T_z = 0$

Configuration:

$$\chi_K = \frac{1}{(4!)^{1/2}} \begin{vmatrix} N(\frac{1}{2} +)_1 & N(\frac{1}{2} +)_2 & N(\frac{1}{2} +)_3 & N(\frac{1}{2} +)_4 \\ N(\frac{1}{2} -)_1 & N(\frac{1}{2} -)_2 & N(\frac{1}{2} -)_3 & N(\frac{1}{2} -)_4 \\ P(\frac{1}{2} +)_1 & P(\frac{1}{2} +)_2 & P(\frac{1}{2} +)_3 & P(\frac{1}{2} +)_4 \\ P(\frac{1}{2} -)_1 & P(\frac{1}{2} -)_2 & P(\frac{1}{2} -)_3 & P(\frac{1}{2} -)_4 \end{vmatrix}$$

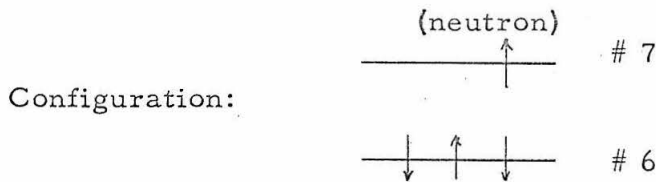
The small diagram is a helpful way to picture the state represented by the determinant. T and T_z are the isotopic spin quantum numbers.

2. F^{20} ground state, $K = 2$, $T = 1$, $T_z = -1$



$$\chi_K = \frac{1}{(4!)^{1/2}} \begin{vmatrix} N(\frac{3}{2}+)_{1} & N(\frac{3}{2}+)_{2} & N(\frac{3}{2}+)_{3} & N(\frac{3}{2}+)_{4} \\ N(\frac{1}{2}+)_{1} & N(\frac{1}{2}+)_{2} & N(\frac{1}{2}+)_{3} & N(\frac{1}{2}+)_{4} \\ N(\frac{1}{2}-)_{1} & N(\frac{1}{2}-)_{2} & N(\frac{1}{2}-)_{3} & N(\frac{1}{2}-)_{4} \\ P(\frac{1}{2}+)_{1} & P(\frac{1}{2}+)_{2} & P(\frac{1}{2}+)_{3} & P(\frac{1}{2}+)_{4} \end{vmatrix}$$

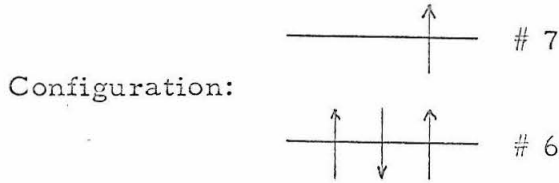
3. F^{20} , $K = 1$, $T = 1$, $T_z = -1$



$$\chi_K = \frac{1}{(4!)^{1/2}} \begin{vmatrix} N(\frac{3}{2}+)_{1} & N(\frac{3}{2}+)_{2} & N(\frac{3}{2}+)_{3} & N(\frac{3}{2}+)_{4} \\ N(\frac{1}{2}+)_{1} & N(\frac{1}{2}+)_{2} & N(\frac{1}{2}+)_{3} & N(\frac{1}{2}+)_{4} \\ N(\frac{1}{2}-)_{1} & N(\frac{1}{2}-)_{2} & N(\frac{1}{2}-)_{3} & N(\frac{1}{2}-)_{4} \\ P(\frac{1}{2}-)_{1} & P(\frac{1}{2}-)_{2} & P(\frac{1}{2}-)_{3} & P(\frac{1}{2}-)_{4} \end{vmatrix}$$

The intrinsic wave function for the band with $K = 2$, $T = 1$ and $T_z = 0$ in Ne^{20} can be generated from the $K = 2$, $T = 1$, $T_z = -1$ wave function for F^{20} by changing a neutron state to a proton state. This gives:

4. Ne²⁰, K = 2, T = 1, T_z = 0

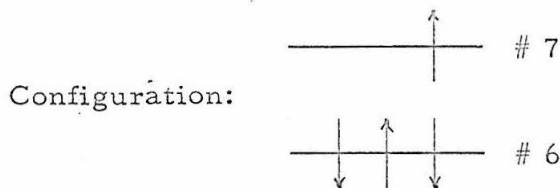


$$\chi_K = \frac{1}{(2 \times 4!)^{1/2}} \begin{vmatrix} N(\frac{1}{2} +)_1 & N(\frac{1}{2} +)_2 & N(\frac{1}{2} +)_3 & N(\frac{1}{2} +)_4 \\ N(\frac{1}{2} -)_1 & N(\frac{1}{2} -)_2 & N(\frac{1}{2} -)_3 & N(\frac{1}{2} -)_4 \\ P(\frac{3}{2} +)_1 & P(\frac{3}{2} +)_2 & P(\frac{3}{2} +)_3 & P(\frac{3}{2} +)_4 \\ P(\frac{1}{2} +)_1 & P(\frac{1}{2} +)_2 & P(\frac{1}{2} +)_3 & P(\frac{1}{2} +)_4 \end{vmatrix}$$

$$- \frac{1}{(2 \times 4!)^{1/2}} \begin{vmatrix} N(\frac{3}{2} +)_1 & N(\frac{3}{2} +)_2 & N(\frac{3}{2} +)_3 & N(\frac{3}{2} +)_4 \\ N(\frac{1}{2} +)_1 & N(\frac{1}{2} +)_2 & N(\frac{1}{2} +)_3 & N(\frac{1}{2} +)_4 \\ P(\frac{1}{2} +)_1 & P(\frac{1}{2} +)_2 & P(\frac{1}{2} +)_3 & P(\frac{1}{2} +)_4 \\ P(\frac{1}{2} -)_1 & P(\frac{1}{2} -)_2 & P(\frac{1}{2} -)_3 & P(\frac{1}{2} -)_4 \end{vmatrix}$$

A similar procedure gives the K = 1, T = 1, T_z = 0 wave function for Ne²⁰.

5. $\underline{\text{Ne}^{20}, K=1, T=1, T_z=0}$

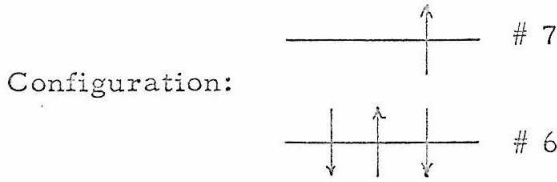


$$\chi_K = \frac{1}{(2 \times 4!)^{1/2}} \begin{vmatrix} N(\frac{1}{2} +)_1 & N(\frac{1}{2} +)_2 & N(\frac{1}{2} +)_3 & N(\frac{1}{2} +)_4 \\ N(\frac{1}{2} -)_1 & N(\frac{1}{2} -)_2 & N(\frac{1}{2} -)_3 & N(\frac{1}{2} -)_4 \\ P(\frac{3}{2} +)_1 & P(\frac{3}{2} +)_2 & P(\frac{3}{2} +)_3 & P(\frac{3}{2} +)_4 \\ P(\frac{1}{2} -)_1 & P(\frac{1}{2} -)_2 & P(\frac{1}{2} -)_3 & P(\frac{1}{2} -)_4 \end{vmatrix}$$

$$- \frac{1}{(2 \times 4!)^{1/2}} \begin{vmatrix} N(\frac{3}{2} +)_1 & N(\frac{3}{2} +)_2 & N(\frac{3}{2} +)_3 & N(\frac{3}{2} +)_4 \\ N(\frac{1}{2} -)_1 & N(\frac{1}{2} -)_2 & N(\frac{1}{2} -)_3 & N(\frac{1}{2} -)_4 \\ P(\frac{1}{2} +)_1 & P(\frac{1}{2} +)_2 & P(\frac{1}{2} +)_3 & P(\frac{1}{2} +)_4 \\ P(\frac{1}{2} -)_1 & P(\frac{1}{2} -)_2 & P(\frac{1}{2} -)_3 & P(\frac{1}{2} -)_4 \end{vmatrix}$$

The orthogonal wave function to this last wave function gives the final wave function.

6. Ne²⁰, K = 1, T = 0, T_z = 0



$$X_K = \frac{1}{(2 \times 4!)^{1/2}} \begin{vmatrix} N(\frac{1}{2} +)_1 & N(\frac{1}{2} +)_2 & N(\frac{1}{2} +)_3 & N(\frac{1}{2} +)_4 \\ N(\frac{1}{2} -)_1 & N(\frac{1}{2} -)_2 & N(\frac{1}{2} -)_3 & N(\frac{1}{2} -)_4 \\ P(\frac{3}{2} +)_1 & P(\frac{3}{2} +)_2 & P(\frac{3}{2} +)_3 & P(\frac{3}{2} +)_4 \\ P(\frac{1}{2} -)_1 & P(\frac{1}{2} -)_2 & P(\frac{1}{2} -)_3 & P(\frac{1}{2} -)_4 \end{vmatrix}$$

$$+ \frac{1}{(2 \times 4!)^{1/2}} \begin{vmatrix} N(\frac{3}{2} +)_1 & N(\frac{3}{2} +)_2 & N(\frac{3}{2} +)_3 & N(\frac{3}{2} +)_4 \\ N(\frac{1}{2} -)_1 & N(\frac{1}{2} -)_2 & N(\frac{1}{2} -)_3 & N(\frac{1}{2} -)_4 \\ P(\frac{1}{2} +)_1 & P(\frac{1}{2} +)_2 & P(\frac{1}{2} +)_3 & P(\frac{1}{2} +)_4 \\ P(\frac{1}{2} -)_1 & P(\frac{1}{2} -)_2 & P(\frac{1}{2} -)_3 & P(\frac{1}{2} -)_4 \end{vmatrix}$$

B.3. Evaluation of Matrix Elements

To evaluate the matrix elements for M1, E2, and the allowed Gamow-Teller beta transitions, it is necessary to rotate the operators from the laboratory system, to the coordinate system fixed in the rotating nucleus. Representing the operators by a general tensor operator, $M_{\lambda q}(\vec{X}^i)$, the rotation is accomplished by:

$$M_{\lambda q}(\vec{X}''') = \sum_{q'} M_{\lambda q'}(\vec{X}') D_{qq'}^{\lambda}(\vec{\theta}_i)$$

The Euler angles, $\vec{\theta}_i$, are the same as those of the D functions appearing in the wave functions. In this fashion, one obtains for the reduced transition probability B' :

$$B' = \sum_{M_f q} \left| \langle I_f M_f K_f | \sum_{q'} M_{\lambda q'}(\vec{X}') D_{qq'}^{\lambda}(\vec{\theta}_i) | I_i M_i K_i \rangle \right|^2$$

By doing the integrals over the collective coordinates, and performing the sum over M_f and q , this expression will reduce to:

Transitions: $K_i \rightarrow K_f$, where $K_i \neq 0$ and $K_f \neq 0$

$$B' = \left[\sum_{q'} \langle I_i K_i, \lambda q' | I_f K_f \rangle \langle \chi_{\Omega_f} | M_{\lambda q'}(\vec{X}') | \chi_{\Omega_i} \rangle \right]^2$$

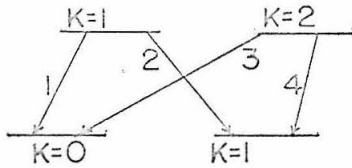
Transitions: $K_i \rightarrow K_f$, where $K_i \neq 0$ and $K_f = 0$

$$B' = \left[\sum_{q'} \sqrt{2} \langle I_i K_i, \lambda q' | I_f K_f \rangle \langle \chi_{\Omega_f} | M_{\lambda q'}(\vec{X}') | \chi_{\Omega_i} \rangle \right]^2$$

The Clebsch-Gordon coefficient, $\langle I_i K_i, \lambda q' | I_f K_f \rangle$, which arises from the integral over the three D functions, is the source of the K selection rule:

$$|K_i - K_f| \leq \lambda$$

A simple picture is a convenient method of representing the transitions to be calculated



wave function for the $2^+ T_2 = 1$ level in either Ne^{20} or F^{20}

wave function for the $2^+ T = 0$, first excited state of Ne^{20}

Numerical values for the transition matrix elements will be listed in the order of the numbering system in the diagram above. The M1 and beta decay transitions will be listed first, and then followed by the E2 transitions.

In the M1 transitions, the neutron and proton contributions combine to form the isotopic spin vector part of the operator:

$$M_{1\mu}^i (\text{Vector}) = \sum_{i=1}^A \frac{1}{2} \ell_{1\mu}^i + \frac{g_p^i - g_h^i}{2} S_{1\mu}^i$$

This operator will be used instead of listing the neutron and proton contributions separately.

Transition 1: $K_i = 1 \rightarrow K_f = 0$

$$M1: B'(M1) = [2(2\ 1, 1\ -1 | 2\ 0) \langle (\frac{1}{2}\ +) | M_{1, -1}^i(V) | (\frac{3}{2}\ +) \rangle]^2$$

Gamow-Teller allowed beta decay (GT):

$$B'(GT) = [\sqrt{2} (2\ 1, 1\ -1 | 2\ 0) \langle (\frac{1}{2}\ +) | S_{1, -1} | (\frac{3}{2}\ +) \rangle]^2$$

where:

$$M_{1,-1}^{\prime}(V) = \frac{1}{\sqrt{2}} \left\{ \frac{1}{2} \ell_{-} + \frac{g_p - g_n}{2} S_{-} \right\}$$

and

$$\ell_{1,-1} = \frac{1}{\sqrt{2}} \ell_{-} = \frac{1}{\sqrt{2}} (\ell_x - i\ell_y)$$

$$S_{1,-1} = \frac{1}{\sqrt{2}} S_{-} = \frac{1}{\sqrt{2}} (S_x - iS_y)$$

Values of the matrix elements over the intrinsic structure are:

$$\langle (\frac{1}{2}+) | \ell_{-} | (\frac{3}{2}+) \rangle = (6)^{1/2} a_1 a_2 + 2c_1 b_2$$

$$\langle (\frac{1}{2}+) | S_{-} | (\frac{3}{2}+) \rangle = c_1 a_2$$

Numerical values as a function of the deformation parameter η are:

η	ℓ_{-}	S_{-}	$M_{1,-1}^{\prime}(V)$	$S_{1,-1}$	$(B^{\prime}(M1))^{1/2}$	$(B^{\prime}(GT))^{1/2}$
6	2.036	0.256	1.572	0.181	2.224	0.181
4	2.033	0.325	1.082	0.230	2.547	0.230
2	2.130	0.445	2.239	0.314	3.163	0.314

Transition 2: $K_i = 1 \rightarrow K_f = 1$

$$M1: B^{\prime}(M1) = [(2\ 1, 1\ 0 | 2\ 1) \{ \langle (\frac{3}{2}+) | M_{1\ 0}^{\prime}(V) | (\frac{3}{2}+) \rangle - \langle (\frac{1}{2}+) | M_{1\ 0}^{\prime}(V) | (\frac{1}{2}+) \rangle \}]^2$$

$$GT: B^{\prime}(GT) = [(2\ 1, 1\ 0 | 2\ 1) \frac{1}{\sqrt{2}} \{ \langle (\frac{3}{2}+) | S_{1\ 0}^{\prime} | (\frac{3}{2}+) \rangle - \langle (\frac{1}{2}+) | S_{1\ 0}^{\prime} | (\frac{1}{2}+) \rangle \}]^2$$

where:

$$M_{10}^{\dagger}(V) = \frac{1}{2} \ell_z + \frac{g_p - g_n}{2} S_z$$

and where

$$\ell_{10} = \ell_z$$

$$S_{10} = S_z$$

Values for the matrix elements over the intrinsic structure are:

$$\langle (\frac{3}{2} +) | \ell_z | (\frac{3}{2} +) \rangle = 1 + b_2^2$$

$$\langle (\frac{1}{2} +) | \ell_z | (\frac{1}{2} +) \rangle = c_1^2$$

$$\langle (\frac{3}{2} +) | S_z | (\frac{3}{2} +) \rangle = \frac{1}{2} - b_2^2$$

$$\langle (\frac{1}{2} +) | S_z | (\frac{1}{2} +) \rangle = \frac{1}{2} - c_1^2$$

The numerical values for the $(\frac{3}{2} +) \rightarrow (\frac{3}{2} +)$, and the $(\frac{1}{2} +) \rightarrow (\frac{1}{2} +)$, will be listed separately, and then combined.

η	$(\frac{3}{2} +) \rightarrow (\frac{3}{2} +)$		$(\frac{1}{2} +) \rightarrow (\frac{1}{2} +)$		transition 2	
	ℓ_z	S_z	ℓ_z	S_z	ℓ_z	S_z
6	1.043	0.457	0.069	0.431	0.974	0.026
4	1.066	0.434	0.113	0.387	0.953	0.047
2	1.110	0.390	0.223	0.277	0.887	0.113

The operators and the reduced transition probabilities have the values:

η	$M_{10}^i(V)$	S_{10}^i	$(B^i(M1))^{1/2}$	$(B^i(GT))^{1/2}$
6	0.608	0.026	0.248	0.007
4	0.799	0.047	0.326	0.014
2	0.977	0.113	0.399	0.033

Transition 3: $K_i = 2 \rightarrow K_f = 0$

This transition is K forbidden, and there is no contribution to the vector operators.

Transition 4: $K_i = 2 \rightarrow K_f = 1$

$$M1: B^i(M1) = [(2\ 2, 1\ -1 | 2\ 1) \langle (\frac{1}{2}\ -) | M_{1,-1}^i(V) | (\frac{1}{2}\ +) \rangle]^2$$

$$GT: B^i(GT) = [\frac{1}{\sqrt{2}} (2\ 2, 1\ -1 | 2\ 1) \langle (\frac{1}{2}\ -) | S_{1,-1}^i | (\frac{1}{2}\ +) \rangle]^2$$

where

$$M_{1,-1}^i(V) = \frac{1}{\sqrt{2}} \left(\frac{1}{2} \ell_- + \frac{g_p^- g_h}{2} S_- \right)$$

and where

$$\ell_{1,-1} = \frac{1}{\sqrt{2}} \ell_-$$

$$S_{1,-1} = \frac{1}{\sqrt{2}} S_-$$

Values for the matrix elements over the intrinsic structure are:

$$\langle (\frac{1}{2}\ -) | \ell_- | (\frac{1}{2}\ +) \rangle = -2(6)^{1/2} a_1 c_1$$

$$\langle (\frac{1}{2}\ -) | S_- | (\frac{1}{2}\ +) \rangle = -[1 - c_1^2]$$

Numerical values as a function of η are:

η	l_-	S_-	$M'_{1_2, -1}(V)$	$S_{1, -1}$	$(B'(M1))^{1/2}$	$(B'(GT))^{1/2}$
6	-1.031	-0.931	-3.460	-0.659	-2.002	-0.268
4	-1.290	-0.887	-3.335	-0.626	-1.927	-0.256
2	-1.816	-0.778	-3.232	-0.546	-1.866	-0.224

For the E2 transitions, it is somewhat simpler to do the indicated sum over the proton coordinates and not introduce the isotopic spin operator. The values of $(B'(E2))^{1/2}$ listed below have been multiplied by the scale factor for r^2 , 2.96.

Transition 1: $K_i = 1 \rightarrow K_f = 0$

$$E2: B'(E2) = [(2\ 1, 2\ -1 | 2\ 0) \langle \frac{1}{2}\ + | r^2 Y_2^{-1}(\theta') | \frac{3}{2}\ + \rangle]^2$$

Values for the matrix element over the intrinsic structure are:

$$\begin{aligned} & \langle \frac{1}{2}\ + | r^2 Y_2^{-1}(\theta') | \frac{3}{2}\ + \rangle \\ & = - [\frac{5}{4\pi}]^{1/2} \{ \frac{1}{2} a_1 a_2 + \sqrt{2} b_1 a_2 + [\frac{3}{2}]^{1/2} c_1 b_2 \} \end{aligned}$$

Numerical values as a function of η are:

η	$r^2 Y_2^{-1}$	$(B'(E2))^{1/2}$
6	-0.755	-0.543
4	-0.755	-0.543
2	-0.687	-0.493

Transition 2: $K_i = 0 \rightarrow K_f = 1$

$$E2: B'(E2) = \left[\frac{1}{2} (2\ 1, 2\ 0 | 2\ 1) \left\{ \langle (\frac{3}{2} +) | r^2 Y_2^0 | (\frac{3}{2} +) \rangle \right. \right. \\ \left. \left. - \langle (\frac{1}{2} +) | r^2 Y_2^0 | (\frac{1}{2} +) \rangle \right\} \right]^2$$

Values for the matrix elements over the intrinsic structure are:

$$\langle (\frac{3}{2} +) | r^2 Y_2^0(\theta') | (\frac{3}{2} +) \rangle = \left[\frac{5}{4\pi} \right]^{1/2} \left[\frac{1}{2} - \frac{3}{2} b_2^2 \right]$$

$$\langle (\frac{1}{2} +) | r^2 Y_2^0(\theta') | (\frac{1}{2} +) \rangle = \left[\frac{5}{4\pi} \right]^{1/2} \left[a_1^2 + 2\sqrt{2} a_1 b_1 + \frac{1}{2} c_2^2 \right]$$

The numerical values for the $(\frac{3}{2} +) \rightarrow (\frac{3}{2} +)$ and $(\frac{1}{2} +) \rightarrow (\frac{1}{2} +)$ will be listed separately, and then combined

η	$(\frac{3}{2} +) \rightarrow (\frac{3}{2} +)$	$(\frac{1}{2} +) \rightarrow (\frac{1}{2} +)$	Transition 2	
	$r^2 Y_2^0$	$r^2 Y_2^0$	$r^2 Y_2^0$	$(B'(E2))^{1/2}$
6	0.274	1.194	-0.920	0.331
4	0.253	1.154	-0.902	0.324
2	0.211	1.016	-0.805	0.289

Transition 3: $K_i = 2 \rightarrow K_f = 0$

$$E2: B'(E2) = \left[- (2\ 2, 2\ -2 | 2\ 0) \langle (\frac{1}{2} -) | r^2 Y_2^{-2}(\theta') | (\frac{3}{2} +) \rangle \right]^2$$

The value for the matrix element over the intrinsic structure is:

$$\langle (\frac{1}{2} -) | r^2 Y_2^{-2}(\theta') | (\frac{3}{2} +) \rangle \\ = \left[\frac{5}{4\pi} \right]^{1/2} \left[a_1 b_1 - \sqrt{2} b_1 b_2 + \left[\frac{3}{2} \right]^{1/2} c_1 a_2 \right]$$

Numerical values as a function of η are:

η	$r^2 Y_2^{-2}$	$(B'(E_2))^{1/2}$
6	0.205	-0.295
4	0.259	-0.372
2	0.391	-0.562

Transition 4: $K_i = 2 \rightarrow K_f = 1$

$$E2: \quad B'(E_2) = \left[\frac{1}{2} (2 \ 2, \ 2 \ -1 | 2 \ 1) \left\langle \left(\frac{1}{2} \ - \right) \left| r^2 Y_2^{-1} \left| \left(\frac{1}{2} \ + \right) \right\rangle \right]^2$$

The value for the matrix element over the intrinsic structure is zero.

The vanishing of this matrix element is accidental.

B.4. Band Mixing

Matrix elements for the R.P.C. term that serves to mix bands differing by one in the K quantum number are discussed by Kerman (78).

The relevant matrix elements are:

$K \neq 0$

$$H_K(I) = \frac{\hbar^2}{2\mathcal{J}_X} \left\{ ((I+K+1)(I-K))^{1/2} (-1) \langle \chi_K | \sum_{i=1}^A J_-^i | \chi_{K+1} \rangle \right\}$$

$K = 0$

$$H_K(I) = \frac{\hbar^2}{2\mathcal{J}_X} \left\{ -\sqrt{2} (I(I+1))^{1/2} \langle \chi_0 | \sum_{i=1}^A J_-^i | \chi_1 \rangle \right\}$$

where $J_-^i = \ell_-^i + S_-^i$. Wave functions are obtained by diagonalizing

the 2 x 2 Hamiltonian matrix:

$$\begin{vmatrix} E_K(I) & H_K(I) \\ H_K(I) & E_{K+1}(I) \end{vmatrix}$$

where:

$$E_K(I) = E_{\text{intr.}} + (I(I+1) - K^2) \frac{\hbar^2}{2\mathcal{I}_K}$$

The matrix is easily diagonalized, and the following table gives the un-normalized eigenfunction with their energy eigenvalues.

$$\underline{E_K(I) \geq E_{K+1}(I)}$$

	<u>Wave Function</u>	<u>Eigenvalue</u>
Higher energy solution:	$\Psi_+ = I M K\rangle + \epsilon_+ I M K+1\rangle$	E_+
Lower energy solution	$\Psi_- = \epsilon_- I M K\rangle + I M K+1\rangle$	E_-

$$\underline{E_K(I) \leq E_{K+1}(I)}$$

Higher energy solution:	$\Psi_+ = \epsilon_+ I M K\rangle + I M K+1\rangle$	E_+
Lower energy solution:	$\Psi_- = I M K\rangle + \epsilon_- I M K+1\rangle$	E_-

where the algebraic symbols are:

$$E_{\pm} = E_{\text{av.}} \pm \frac{1}{2} [(\Delta E)^2 + 4(H_K(I))^2]^{1/2}$$

$$\epsilon_{\pm} = \mp \frac{|\Delta E|}{2H_K(I)} \pm \frac{1}{2H_K(I)} [(\Delta E)^2 + 4(H_K(I))^2]^{1/2}$$

$$E_{av} = \frac{E_K(I) + E_{K+1}(I)}{2}$$

$$\Delta E = E_K(I) - E_{K+1}(I)$$

For the $K = 1$ and 2 band with $T = 1$ in Ne^{20} and F^{20} , the R.P.C. term is given by:

$$H_1(I) = \frac{\hbar^2}{2J_X} \{ ((I+2)(I-1))^{1/2} (-1) < (\frac{1}{2} -) | J_- | (\frac{1}{2} +) > \}$$

The matrix element over the intrinsic structure as a function of η is:

η	J_-
6	-1.962
4	-2.177
2	-2.594

For $\eta = 6$, the values of $H_K(I)$ as a function of I are:

I	$H_K(I)$ - (units of $\frac{\hbar^2}{2J_X}$)
2	3.294
4	6.204
6	8.325

For the $K = 0$ and 1 bands with $T = 0$ of the Ne^{20} ground state band, $H_K(I)$ is given by:

$$H_0(I) = \frac{\hbar^2}{2J_X} [2(I(I+1))^{1/2} (-1) < (\frac{1}{2} +) | J_- | (\frac{3}{2} +) >]$$

The matrix element over the intrinsic structure as a function of η is:

η	J_-
6	2.292
4	2.358
2	2.575

B. 5. Numerical Results

The procedure at this point should be an application of the formulas in B. 4 to match the levels in F^{20} and Ne^{20} . Such a procedure has been demonstrated by Paul (79) for the $1/2$ and $3/2$ bands in F^{19} . Once the energy levels are matched, the indicated wave functions should be used in the calculation of the M1, beta decay, and E2 transition rates. Unfortunately the lack of information about the spin assignments of F^{20} levels or the $T = 1$ levels in Ne^{20} makes this procedure impossible. Hence to obtain a qualitative picture from the calculation, the transition rates were calculated for a range of mixtures in the $T = 1$ and $T = 0$ bands. By using $\sin \theta$ and $\cos \theta$ as the amplitudes of the two mixed bands, one obtains a convenient method of varying the mixture. The form of the wave functions used for the calculations were:

initial state ($T = 1$ bands)

$$\Psi_{(I, M)} = - \sin \theta_i |I M K = 1 \rangle + \cos \theta_i |I M K = 2 \rangle$$

final state ($T = 0$ bands)

$$\phi_{(I, M)} = \cos \theta_f |I M K = 0 \rangle + \sin \theta_f |I M K = 1 \rangle$$

Several assumptions have prejudiced the form of these wave functions. The final state wave function corresponds to the one in B. 4

that places the $K = 0$ band lower than the $K = 1$ band. Mottelson (80) describes this as a necessary condition since the $K = 1, T = 0$ band being mixed in the ground state band is a spurious band, or a band that has been introduced by the additional collective coordinates (see ref. 77, for example), and indeed, he points out that such a band is introduced by the cranking model (81), to account for the moment of inertia. From this model, the first term in the expansion for \mathcal{J}_X for the four particles outside the O^{16} core is:

$$\mathcal{J}_X \approx 4 \times 2 \hbar^2 \frac{\langle (\frac{3}{2} +) | J_X | (\frac{1}{2} +) \rangle^2}{\Delta E}$$

In so far as ΔE is large, the amplitude for ϵ_- in B.4 is given by:

$$\epsilon_- \approx \frac{\hbar^2}{2\mathcal{J}_X} 2 [I(I+1)]^{1/2} \frac{\langle (\frac{3}{2} +) | J_X | (\frac{1}{2} +) \rangle}{\Delta E}$$

Combining these last two equations, and substituting the value for the matrix element for $\eta = 4$ given in B.4 gives $\theta_i \sim 27^\circ$ or the ground state of Ne^{20} is $\sim 79\%$ $K = 0$ band in intensity.

The initial state wave function is associated with a definite level order in Ne^{20} or F^{20} . The results of a calculation of this level order for $\eta = 6$ and $\hbar^2/2\mathcal{J}_X = 0.27$ Mev is given in figure 29d as a function of θ_i and ΔE of B.4. The energy scale has been adjusted in height so the lower of the two $I = 2$ levels corresponds to the 10.27-Mev level in Ne^{20} . For those solution with $E_{K=1}(I) < E_{K=2}(I)$, an $I = 1, T = 1$ level (shown as a dotted line in figure 29d) is seen to lie below the 10.27-Mev level, and would imply the first $T = 1$ level in Ne^{20}

or the F^{20} ground state should be spin one. For $E_{K=1(I)} > E_{K=2(I)}$ the $I = 1$ level lies above the lower $I = 2$ level for most θ_i , and the wave function used for numerical calculations corresponds to this solution. Approximate limits can be put on θ_i . The first excited state of F^{20} is at 0.65 Mev (4), indicating $\theta_i < 30^\circ$. For small θ_i , the separation of the two bands becomes very large, and hence θ_i will probably be larger than 10° .

The results of the calculation for $\eta = 6, 4, 2$ are given in figure 29a, b, c as a function of θ_i and θ_f . The lines marked M1 are, top to bottom, the upper limit, best value, and lower limit for the experimental M1 width. Similar lines for the E2 transition are marked. The line marked β is the experimental value for the F^{20} ground state beta decay. For all three transitions, the plotted solutions are those obtained from $-(B')^{1/2}$. There are no solutions for $+(B')^{1/2}$ for the beta decay and M1 decay. The $+(B'(E2))^{1/2}$ equal to the lower limit of the experimental values will appear in the $\eta = 6$ (fig. 29a) and $\eta = 4$ (fig. 29b) plots in the upper left corner above $(B'(E2))^{1/2} = 0$.

In such plots, one hopes to find one point in common to all three experimental values. Here it is not the case. The M1 and E2 values for the 8.64-Mev gamma ray do show some of the desired properties in the $\eta = 4$ diagram, which corresponds most closely to the value of $\eta = 4.26$ for the Ne^{20} ground state band. Picking $\theta_f = 27^\circ$, the best value for the M1 decay gives $\theta_i = 24^\circ$. These values of θ_i and θ_f fall in the "reasonable" range. A value for the radiative width of the E2 transition a little lower than the best experimental value (E2-on in

figure 29b) will overlap this point. Furthermore, the matrix elements for the M1 and E2 transitions have the same phase as is required by the experimental data shown in figure 18.

The situation for the beta decay is not as satisfactory. In all three plots, a reasonable value for θ_f makes θ_i too low or vice versa. Unexplained is the gap between the beta line and the M1 lines that indicates the beta decay is either too weak or the M1 decay too strong. For example, it is possible to make the two solutions overlap if the radiative width for the 8.64-Mev transition is reduced from 5.6 ev to 1.9 ev.

Hence for the assumptions that have been made, it seems the unified model is only able to give a qualitative picture of the experimental data. The slow beta decay of the F^{20} ground state can be attributed to the K selection rule; the fast M1 decay can be arranged by a reasonable mixture of bands in the initial and final states.

Of course the assumptions of this calculation are open to question. The most questionable assumption is that a $K = 1$ and $K = 2$ band mixture is a good description of the F^{20} ground state. Figure 29d indicates that this assumption can account for only 5 of the 12 levels in the first 3 Mev excitation energy in F^{20} . If the remaining levels are members of bands that have intrinsic wave functions similar to the $K = 1$ and $K = 2$ bands used in the calculation, the structure of the ground state of F^{20} , or the first $T = 1$ level in Ne^{20} would be considerably more complex than assumed.

TABLE I
STATES IN NE²⁰ FROM O¹⁶ (α, γ)Ne²⁰

Resonance Energy-Lab E_a (keV)	Initial State		Final State (4)			Radiation			$ M ^2$ (ref. 43)
	E_X (MeV)	$J^\pi; T$	$\Gamma_{C.M.}$ (keV)	E_X (MeV)	$J^\pi; T$	Multipole	$\omega\Gamma_\gamma$ (ev)	Γ_γ (ev)	
5374 \pm 9	9.029 \pm 0.008	4 ⁺ ; 0	≤ 3	1.63	2 ⁺ ; 0	E2	3.4 \pm 0.4	0.38 \pm 0.05	7.0
5940 \pm 30	9.48 \pm 0.03	2 ⁺ ; 0	29 \pm 15	1.63	2 ⁺ ; 0	(E2 or M1)	1.3 \pm 0.5	0.26 \pm 0.1	3.2 (E2) or 0.025 (M1)
6610 \pm 30	10.02 \pm 0.03	(ref. 28) (4 ⁺); 0	155 \pm 30	0	0 ⁺ ; 0	E2	≤ 0.3	≤ 0.06	≤ 0.3
6930 \pm 10	10.270 \pm 0.009	(ref. 30) 2 ⁺ ; 1	≤ 2	0	0 ⁺ ; 0	(E4)	≤ 0.6	≤ 0.07	6.9 (for E2)
7940 \pm 20	11.08 \pm 0.02	4 ⁺ ; 1	≤ 3	1.63	2 ⁺ ; 0	M1	27.8 \pm 3	5.6 \pm 0.6	0.41
				0	0 ⁺ ; 0	E2	(2.2 ^{+4.1} -1.9) $\times 10^{-3}$	0.017	
				4.97	2 ⁻ ; 0	E1	≤ 2.2	≤ 0.44	$\leq 6 \times 10^{-3}$
				4.25	4 ⁺ ; 0	M1	46 \pm 5	4.8 \pm 0.5	0.72
8170 \pm 30	11.27 \pm 0.03	(1 ⁻ or 2 ⁺)	≤ 4	0	0 ⁺ ; 0	E2	≤ 0.7	≤ 0.08	≤ 0.4
				1.63	2 ⁺ ; 0	E2	≤ 12	≤ 1.4	≤ 0.043
				7.02	(4 ⁻); 0	E1			
8540 \pm 40	11.56 \pm 0.04	(0 ⁺ , 1 ⁻ , 2 ⁺ , 3 ⁻ , 4 ⁺)		0	0 ⁺ ; 0		0.9 \pm 0.4		
(9250 \pm 40)	(12.13 \pm 0.04)			1.63	2 ⁺ ; 0		≤ 0.3		
				0	0 ⁺ ; 0		≤ 0.2		
				1.63	2 ⁺ ; 0		0.5 \pm 0.3		
Decays by alpha emission to the 6.13-Mev level in O ¹⁶ with $\frac{\omega\Gamma_{\alpha'}}{\Gamma_{\alpha'}} = 100 \pm 50$ ev									
9400 \pm 40	12.25 \pm 0.04	(0 ⁺ , 1 ⁻ , 2 ⁺ , 3 ⁻ , 4 ⁺)		0	0 ⁺ ; 0		≤ 1		
			40 \pm 16	1.63	2 ⁺ ; 0		7 \pm 3		
9570 \pm 40	12.39 \pm 0.04	(3 ⁻ or 4 ⁺)		0	0 ⁺ ; 0		≤ 1		
			46 \pm 16	1.63	2 ⁺ ; 0		3.5 \pm 2		
Decays by alpha emission to the 6.13-Mev level in O ¹⁶ with $\frac{\omega\Gamma_{\alpha'}}{\Gamma_{\alpha'}} = 3 \pm 1$ kev									

TABLE 2
ALPHA PARTICLE PARAMETERS

E_r (Mev)	E_X (Mev)	$J^\pi; T$	Γ_α (kev)	θ^2 (per cent)
5.374	9.029	$4^+; 0$	≤ 3	≤ 1.3
5.940	9.48	$2^+; 0$	29 ± 15	1.5
6.610	10.02	$(4^+); 0$	155 ± 30	25.0
6.930	10.27	$2^+; 1$	≤ 2	≤ 0.08
7.940	11.08	$4^+; 1$	≤ 3	≤ 0.21
9.570	12.39	$(3^-);$	46 ± 16	1.23
Γ_α to 6.13-Mev level in $O^{16} =$			3 ± 1	56.0

TABLE 3
 GAMMA RAY ANGULAR DISTRIBUTION FUNCTIONS
 FOR $O^{16}(\alpha, \gamma)Ne^{20}$

In the following table, the coefficients a_2 , a_4 , and a_6 will be given for angular distributions of the form

$$W(\theta) = 1 + a_2 P_2(\cos \theta) + a_4 P_4(\cos \theta) + a_6 P_6(\cos \theta)$$

where θ is measured with respect to the beam axis.

<u>J^{π}</u> <u>Initial State</u>	<u>Gamma-Ray</u> <u>Multipolarity</u>	<u>a₂</u>	<u>a₄</u>	<u>a₆</u>
<u>TRANSITIONS TO 0⁺ GROUND STATE</u>				
1 ⁻	E1	-1.000	0	0
2 ⁺	E2	+0.714	-1.714	0
3 ⁻	E3	+1.000	+0.273	-2.273
<u>TRANSITIONS TO 2⁺ FIRST EXCITED STATE</u>				
0 ⁺	E2	0	0	0
1 ⁻	E1	-0.100	0	0
2 ⁺	M1	+0.500	0	0
2 ⁺	E2	-0.153	-0.490	0
3 ⁻	E1	-0.400	0	0
4 ⁺	E2	+0.510	-0.367	0
<u>TRANSITIONS TO 4⁺ SECOND EXCITED STATE</u>				
2 ⁺	E2	+0.204	-0.014	0
3 ⁻	E1	-0.167	0	0
4 ⁺	M1	+0.500	0	0
4 ⁺	E2	-0.301	-0.601	0
5 ⁻	E1	-0.333	0	0
6 ⁺	E2	+0.455	-0.242	0

REFERENCES

1. T. Lauritsen, *Ann. Rev. Nuclear Sci.* 1, 67 (1952); and also, T. Lauritsen and F. Ajzenberg-Selove, "The Light Isobars," Joint Report of Haverford College and California Institute of Technology, August, 1960.
2. A. E. Litherland, J. A. Kuehner, H. E. Gove, M. A. Clark, and E. Almqvist, *Phys. Rev. Letters* 7, 98 (1961).
3. E. M. Burbidge, G. R. Burbidge, W. A. Fowler, and F. Hoyle, *Revs. Mod. Phys.* 29, 547 (1957).
4. T. Lauritsen and F. Ajzenberg-Selove, "Nuclear Data Sheets," sets 5 and 6, National Academy of Sciences (1962).
5. R. J. Van de Graaff, *Nuc. Instr. and Meth.* 8, 195 (1960).
6. H. E. Gove, *Nuc. Instr. and Meth.* 11, 63 (1961).
7. P. H. Rose, *Nuc. Instr. and Meth.* 11, 49 (1961).
8. P. H. Rose, A. B. Wittkower, R. B. Bastide, and A. J. Gale, *Rev. Sci. Instr.* 32, 568 (1961).
9. H. E. Gove, J. A. Kuehner, A. E. Litherland, E. Almqvist, D. A. Bromley, A. J. Ferguson, P. H. Rose, R. P. Bastide, N. Brooks, and R. J. Connor, *Phys. Rev. Letters* 1, 251 (1958).
10. D. A. Bromley, A. J. Ferguson, H. E. Gove, J. H. Kuehner, A. E. Litherland, E. Almqvist, and R. Batchelor, *Can. J. Phys.* 37, 1514 (1959).
11. R. H. Spear, J. D. Larson, and J. D. Pearson, *Nuc. Phys.* (to be published).
12. A. H. F. Muggleton and F. A. Howe, *Nuc. Instr. and Meth.* 12, 192 (1961).
13. D. A. Vermilyea, *Acta Metallurgica* 1, 282 (1953).
14. A. Charlesby and J. J. Polling, *Pro. Phys. Soc. (London)* 227, 438 (1954-5).
15. R. W. Kavanagh, Ph.D. Thesis, California Institute of Technology (1953).
16. H. Lung, Ph. Panussi, and J. Jänke, *Nuc. Instr. and Meth.* 9, 121 (1960).

17. M. E. Rose, Phys. Rev. 91, 610 (1953).
18. J. Stolzfus, J. Friichtenicht, and E. Nelson, Bull. Am. Phys. Soc. 1, 329 (1956).
19. F. Ajzenberg-Selove and T. Lauritsen, Nuc. Phys. 11, 1 (1959).
20. N. H. Lazar, R. C. Davis, and P. R. Bell, Nucleonics 14 (# 4), 52 (1956)
21. G. W. Grodstein, "X-Ray Attenuation Coefficients from 10 kev to 100 Mev," NBS Circular 583 (1957).
22. W. F. Hornyak and T. Coor, Phys. Rev. 92, 675 (1953).
23. A. T. Nelms, "Graphs of the Compton Energy-Angle Relationship and the Klein-Nishina Formula from 10 kev to 500 Mev," NBS Circular 542 (1953).
24. C. D. Zerby and H. S. Moran, Nuc. Instr. and Metho. 14, 115 (1961); and also, C. D. Zerby and H. S. Moran, Oak Ridge National Laboratory Report, ONRL 3169 (1961).
25. R. L. Heath, IRE Transactions on Nuclear Science NS-9, 294 (1962).
26. J. B. Marion, Revs. Mod. Phys. 33, 139 (1961).
27. F. Everling, L. A. Konig, J. H. E. Mattauch, and A. H. Wapstra, "1960 Nuclear Data Tables, Part 1," Report of the Nuclear Data Project, U. S. Government Printing Office, Washington 25 D. C. (1961).
28. L. C. McDermott, K. W. Jones, H. Smotrich, and R. E. Benenson, Phys. Rev. 118, 175 (1960).
29. R. H. Davis, M. K. Mehta, and W. Hunt, "Annual Progress Report for the Year 1961," Department of Physics, Florida State University Tandem Accelerator Program, page 11; and also, W. F. Hunt, M. K. Mehta, and R. H. Davis, Bull. Am. Phys. Soc. 7, 71 (1962).
30. J. M. Blatt and V. F. Weisskopf, "Theoretical Nuclear Physics," Wiley and Sons, New York (1952); p. 627.
31. L. Radicati, Phys. Rev. 87, 521 (1952); and also, M. Gell-Mann and V. Telegdi, Phys. Rev. 91, 169 (1953).
32. M. A. Clark, H. E. Gove, and A. E. Litherland, Can. J. Phys. 39, 1241 (1961).

33. B. J. Toppel, S. D. Bloom, and D. H. Wilkinson, *Phil. Mag.* 2, 61 (1957).
34. T. W. Bonner, *Pro. Roy. Soc. (London)*, A174, 339 (1940).
35. J. M. Calvert, A. A. Jaffee, and E. E. Maslin, *Proc. Phys. Soc. (London)* 68A, 1017 (1955).
36. T. A. Rabson, W. D. Barfield, D. L. Bernard, T. W. Bonner, and W. W. Givens, *Nuc. Phys.* 21, 43 (1960).
37. J. W. Butler, *Phys. Rev.* 118, 222 (1960).
38. L. C. McDermott, private communication to R. H. Spear.
39. M. E. Rose, *Phys. Rev.* 91, 610 (1953).
40. W. A. Fowler, C. C. Lauritsen, and T. Lauritsen, *Revs. Mod. Phys.* 20, 236 (1948).
41. H. E. Gove, "Nuclear Reactions," Vol. 1 ed. by P. M. Endt and M. Demure, North Holland Pub. Co., Amsterdam (1960).
42. W. Whaling, *Handbuch der Physik* 34, 193 (1958); and also, D. Demirlioglu and W. Whaling, to be published.
43. D. H. Wilkinson, "Nuclear Spectroscopy," V. I., ed. by F. Ajzenberg-Selove, Academic Press, New York (1960).
44. D. H. Wilkinson, "Proceedings of the Rehovoth Conference," ed. by H. J. Lipkin, North Holland Publishing Co., Amsterdam (1958).
45. D. H. Wilkinson, *Phil. Mag.* 1, 127 (1956).
46. S. P. Lloyd, *Phys. Rev.* 81, 161 (1951).
47. H. E. Gove, A. E. Litherland, and M. A. Clark, *Can. J. Phys.* 39, 1243 (1961).
48. J. Orear, University of California Radiation Laboratory Report, UCRL-8417 (1958).
49. D. H. Wilkinson, *Phil. Mag.* 1, 1031 (1956).
50. E. Freiberg and V. Soergel, *Zeit. für Phys.* 162, 114 (1961).
51. F. Boehm, V. Soergel, and B. Stech, *Phys. Rev. Letters* 1, 77 (1958).

52. C. Wong, Phys. Rev. 95, 761 (1954); and also, C. Wong, Ph.D. Thesis, California Institute of Technology (1953).
53. G. Morpurgo, Phys. Rev. 110, 721 (1958).
54. E. K. Warburton, Phys. Rev. 113, 595 (1959).
55. W. E. Burcham, Prog. In Nuclear Phys. 4, 171, (1955).
56. W. T. Sharp, H. E. Gove, and E. B. Paul, "Graphs of Coulomb Wave Functions," 2nd edition, TP 1-70, A. E. C. L. report No. 268 (1955).
57. J. D. Larson and R. H. Spear, Bull. Am. Phys. Soc. 6, 505 (1961).
58. L. Meyer-Schützmeister and S. S. Hanna, Phys. Rev. 108, 1506 (1957).
59. A. E. Litherland, M. A. Clark, and H. E. Gove, Can. J. Phys. 39, 1249 (1961).
60. F. A. El Bedewi, Pro. Phys. Soc. (London) 69A, 221 (1956).
61. J. P. Elliott and A. M. Lane, Handbuch der Physik, 39, 241 (1957). In particular see page 347.
62. H. Reeves and E. E. Saltpeter, Phys. Rev. 116, 1505 (1959).
63. H. E. Gove, A. E. Litherland, and M. A. Clark, Nature 191, 1381 (1961).
64. L. C. Biedeharn and M. E. Rose, Revs. Mod. Phys. 25, 729 (1953).
65. S. Devons and L. J. B. Goldfarb, Handbuch der Physik, 42, 362 (1957).
66. D. H. Wilkinson, "Illustration of Angular Correlation Computations Using the Racah Coefficient Methods," Cavendish Laboratory, 1954.
67. L. C. Biedeharn, "Nuclear Spectroscopy," ed. by F. Ajzenberg-Selove, Academic Press, New York (1960); page 732.
68. H. A. Wiedemüller, Lecture Notes by F. B. Morinigo and Y. R. Cusson, California Institute of Technology (1962).
69. W. T. Sharp, J. M. Kennedy, B. J. Sears, and M. G. Hoyle, "Tables of Coefficients for Angular Distribution Analysis," CRT-556, Atomic Energy of Canada, Limited (1959).

70. Reference 30, page 599.
71. A. J. Ferguson and A. R. Rutledge, "Coefficients for Triple Angular Correlation Analysis in Nuclear Bombardment Experiments," CRP-G15, Atomic Energy of Canada Limited (1957).
72. P. J. Twinn and J. C. Willmott, to be published.
73. A. Bohr, Klg. Danske Videnskab. Selskab., Mat.-fys. Medd. 26, No. 14 (1952).
74. A. Bohr and B. R. Mottleson, Klg. Danske Videnskab. Selskab., Mat.-fys. Medd. 27, No. 16 (1953).
75. S. G. Nilsson, Kug. Danske Videnskab. Selskab., Mat.-fys. Medd. 29, No. 16 (1955).
76. B. R. Mottleson and S. G. Nilsson, Kug. Danske Videnskab. Mat.-fys. Skr. 1, No. 8 (1959).
77. A. K. Kerman, "Nuclear Reactions," Vol. 1, ed. by P. M. Endt and M. Demur, North Holland Pub. Co., Amsterdam (1958).
78. A. K. Kerman, Klg. Danske Videnskab. Selskab., Mat.-fys. Medd. 30, No. 15 (1956).
79. E. B. Paul, Phil. Mag. 2, 311 (1957).
80. B. R. Mottelson, private communication.
81. D. Inglis, Phys. Rev. 103, 1786 (1956); and also reference 77.

Figure 1 is the energy level diagram for Ne^{20} from Lauritsen and Ajzenberg-Selove (19). The gamma-ray yield curve from $\text{O}^{16}(\alpha, \gamma)\text{Ne}^{20}$ is on the left side above the threshold for $\text{O}^{16} + \alpha$. Many resonances found in the $\text{O}^{16}(\alpha, \gamma)\text{Ne}^{20}$ reaction have been also reported in the $\text{O}^{16}(\alpha, \alpha)\text{O}^{16}$ and $\text{F}^{19}(\text{d}, \text{n}\gamma)\text{Ne}^{20}$ reactions.

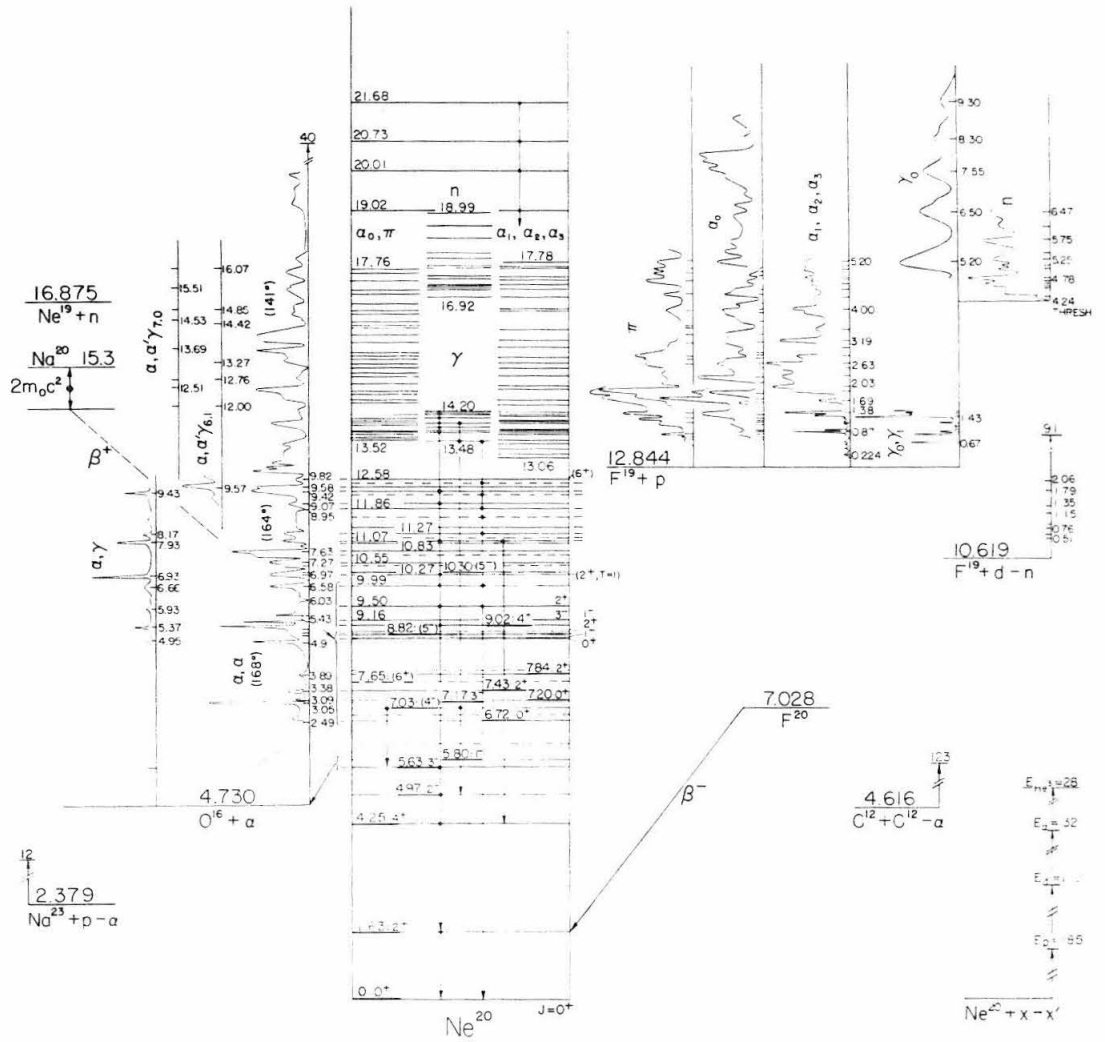


Fig. 1

Figure 2 shows the original target chamber. The labelled parts are: 1) beam direction, 2) slit system (lucite walls) with orthogonal pairs of slits (3), 4) cold trap filled with charcoal (Dewar filled with liquid nitrogen to cool trap not shown), 5) Penning gauge, 6) glass walled target chamber, 7) target rod, 8) target, 9) quartz beam viewers, 10) batteries supplying potentials to suppress secondary electrons. See page 4 for further details.

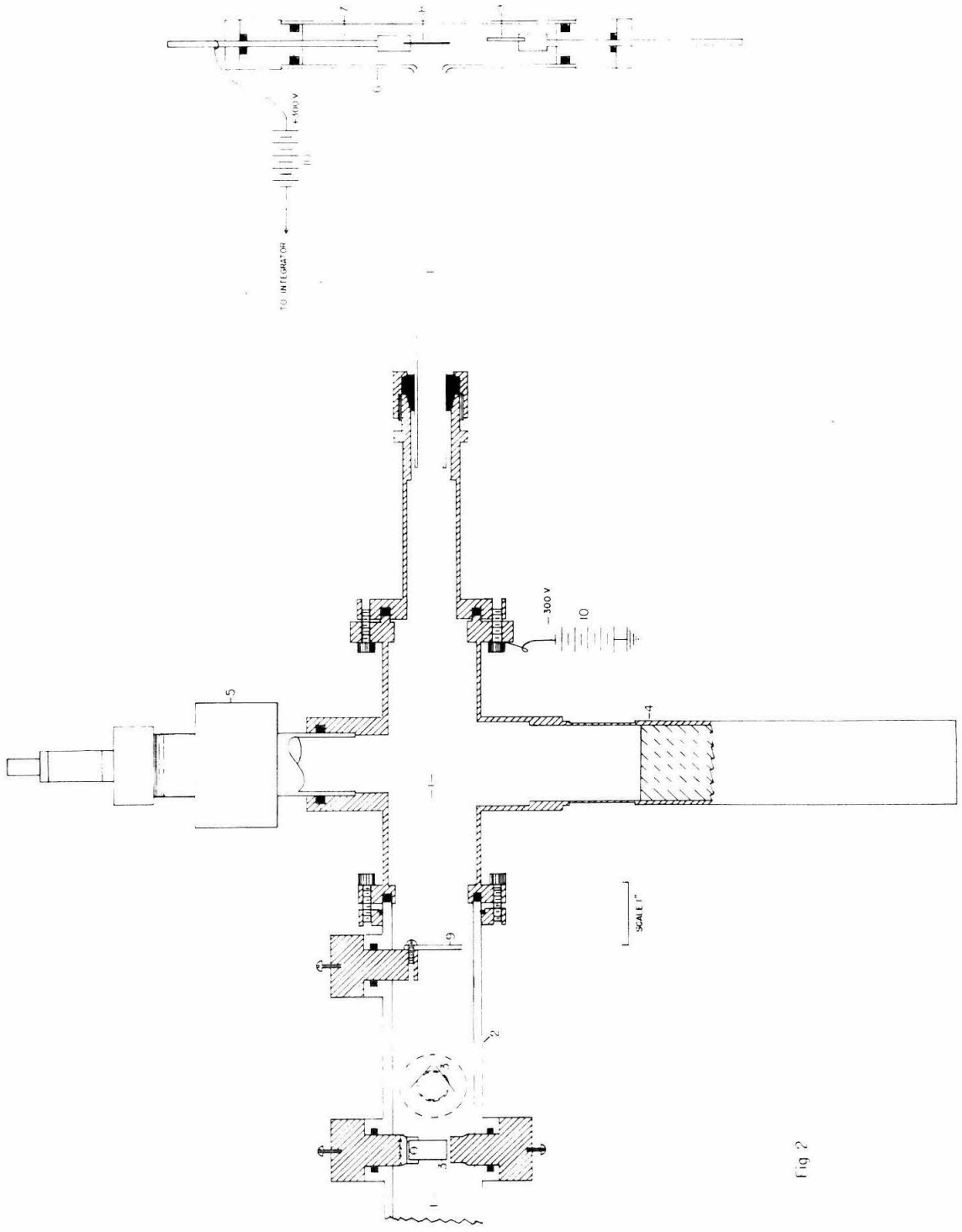


Fig 2

Figure 3 shows the "clean vacuum" system. The labelled parts are: 1) "low vacuum" side, 2) beam axis, 3) stainless steel in-line cold trap, 4) 3/8" diameter beam tube, 5) liquid nitrogen reservoir, 6) "high vacuum" side, 7) 9 ℓ/sec ion pump, 8) alnico magnet, 9) mild steel cans, 10) glass target chamber, 11) viton "O" rings without vacuum grease, 12) glass to kovar seal, 13) quartz viewer, 14) electron suppressor ring and supporting rod, 15) target. See page 6 for further details.

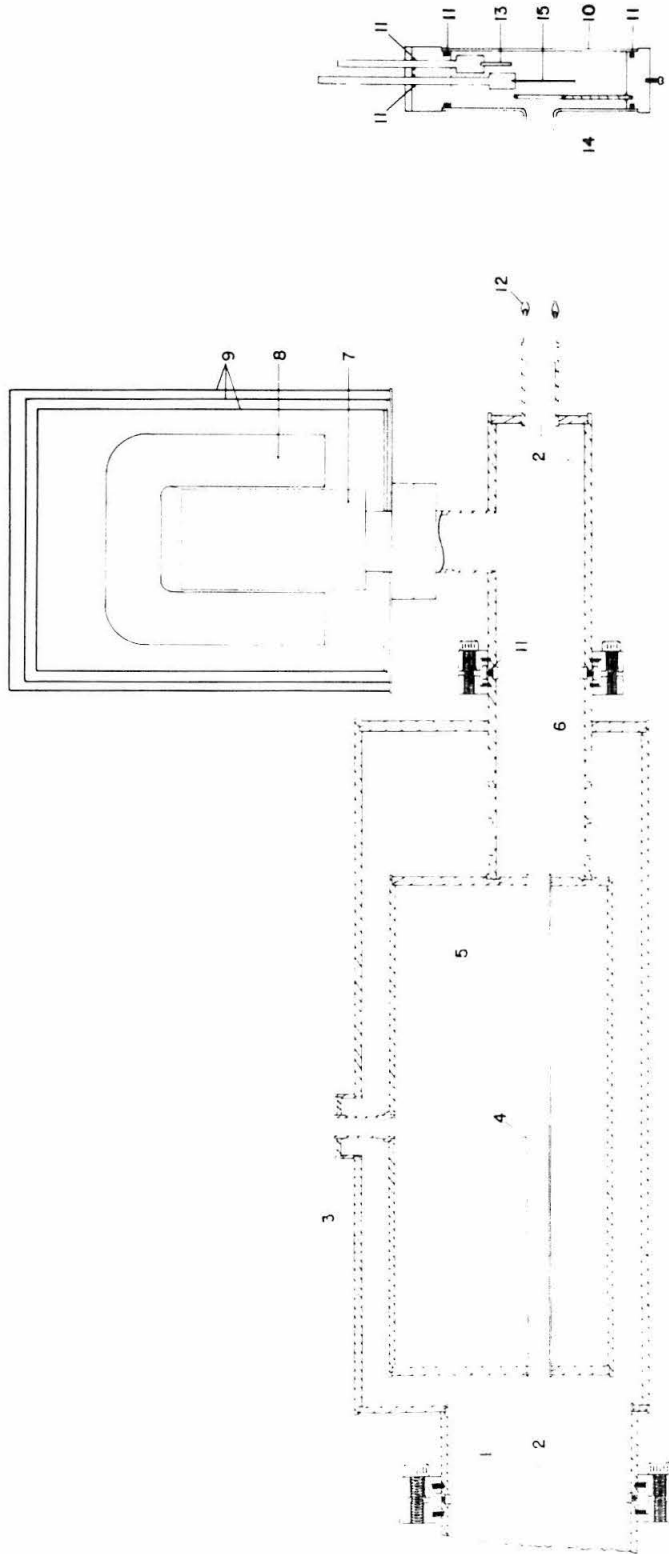


Fig. 3

Figure 4 shows the target chamber used for making and bombarding ice targets. The labelled parts are: 1) beam tube and vacuum system of accelerator, 2) beam axis, 3) vacuum valves shown schematically, 4) auxiliary pump-out, 5) lucite insulator, 6) electron suppressor ring and supporting rod, 7) brass walled target chamber, 8) water level vial of stainless steel, 9) target rod vial of stainless steel (Dewar filled with liquid nitrogen to cool 8 and 9 not shown), 10) 0.375" diameter copper target rod supporting a 0.125" copper disc (11) faced with a 0.020" tantalum disc (12), 13) brass window 0.0625" thick. Further details are given on page 7.

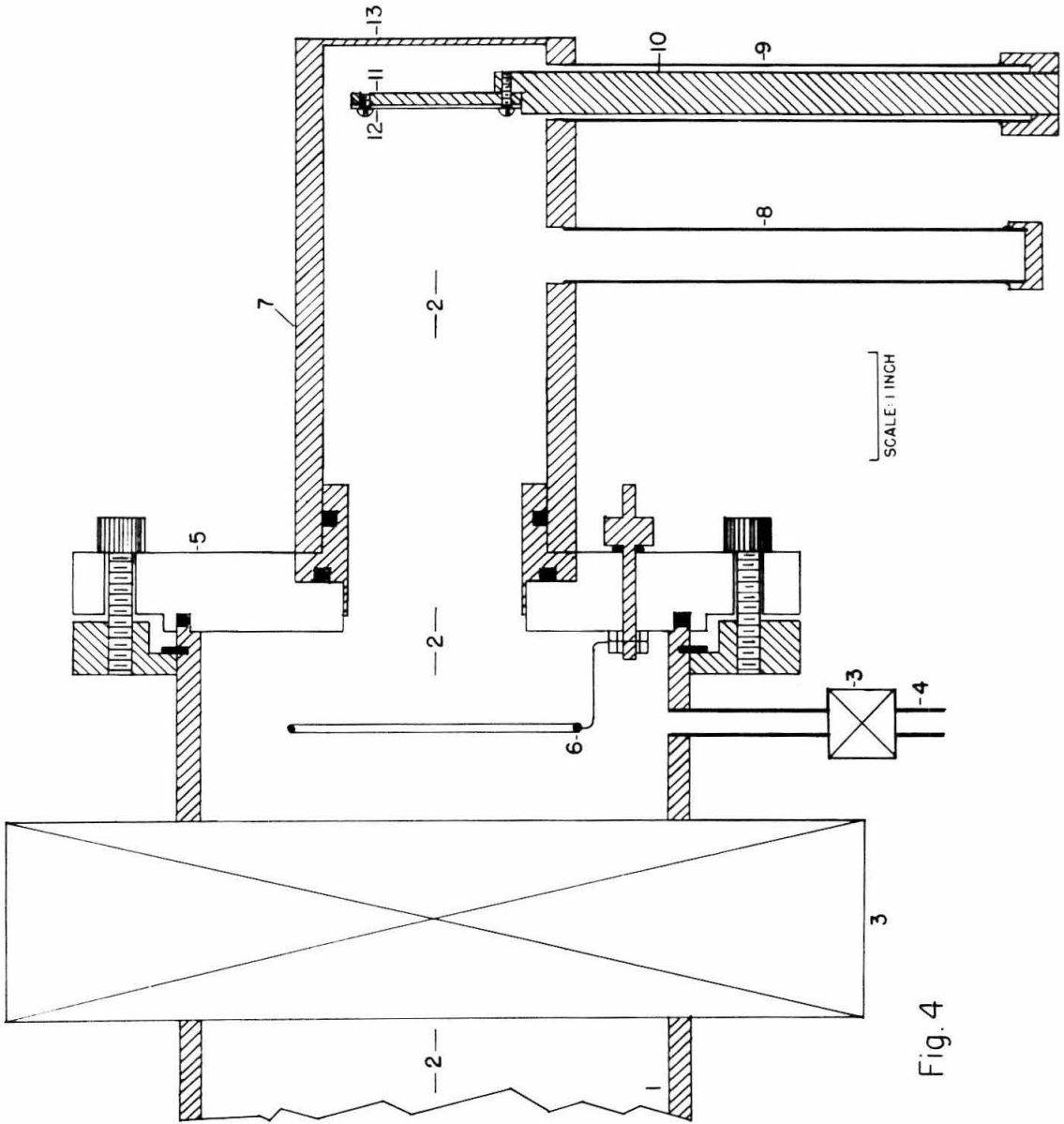


Fig. 4

Figure 5 shows the anodizing apparatus used to make tantalum oxide targets. The voltage drop across the high resistance of the oxide layer, as measured by the vacuum tube voltmeter, may be related to the oxide layer thickness. The targets used in this experiment were anodized to 150 volts at $\sim 0.10 \text{ ma/cm}^2$ giving targets 55 kev thick to 7 Mev alpha particles, or an oxide layer 2240 Å thick. Targets were boiled in distilled water after anodizing to remove the electrolyte. See page 8 for further details.

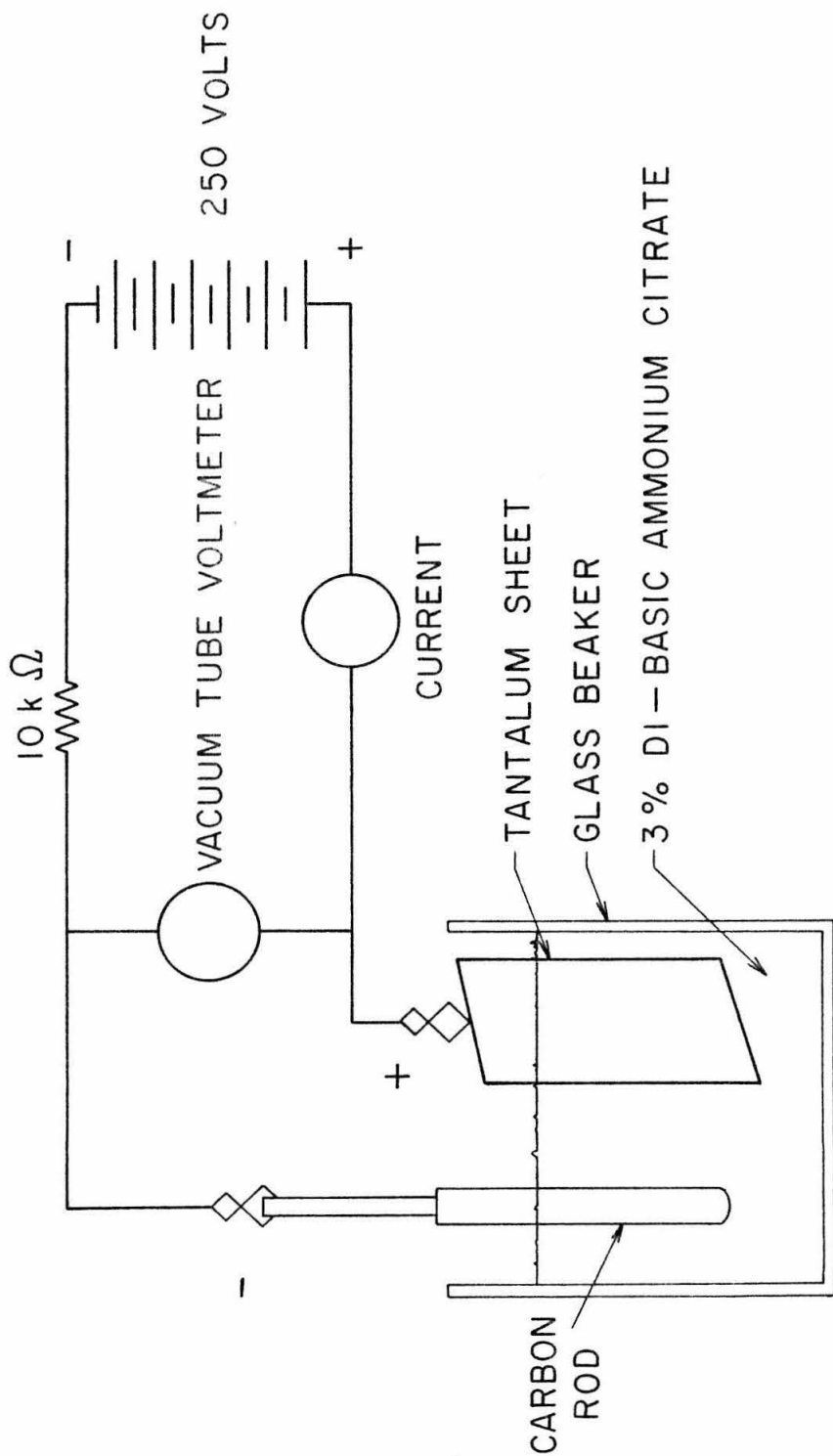


Fig. 5

Figure 6 is the block diagram for the fast-slow coincidence circuit used to investigate gamma-ray cascades and to measure triple angular correlations. Signals, accurately defined in time, were derived from the zero crossing of the pulses from the Hamner amplifiers by the pick-off circuit shown in figure 7. The measured fast coincidence resolving time was about 70 ns; the calculated resolving time from the clipping cable lengths is 50 ns, indicating a time jitter of ± 10 ns in the zero crossing of the pulses from the Hamner amplifiers. Typical counting rates gave calculated real to random ratios of 960 to 1 for the 8.64-1.63-Mev gamma-ray cascade from the 6.93-Mev resonance; measured real to random ratios were in excess of 500 to 1. The slow coincidence mixer has a resolving time of 1.4 μ s. As explained on page 11 in the text, economy in running time was achieved by storing both singles and coincidence pulses from one of the detectors in the 400 channel analyzer.

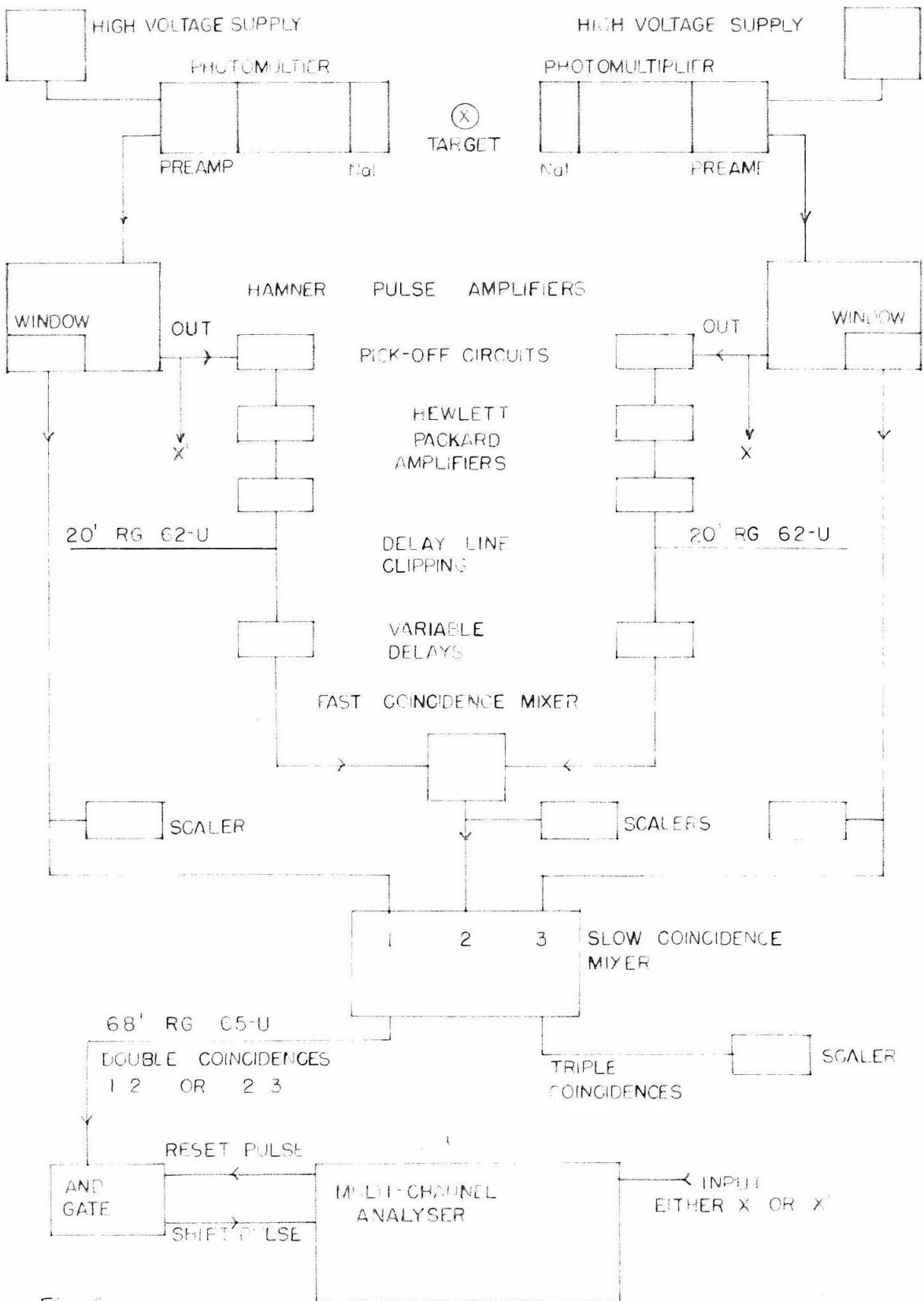


Fig 6

Figure 7 is the schematic of the "pick-off" circuit used to detect the zero crossing of the Hamner amplifier pulse. The operation of this circuit is as follows. The positive-going part of the signal from the Hamner cuts the current off in the second part of the tube, turning the tunnel diode off along path 1 of the operating loop marked on the tunnel diode characteristic curve. As the signal starts to drop towards zero, the current in the tunnel diode rises up the front edge of its characteristic until it reaches 4.7 ma, at which time it flips over to its quiescent point along path 2. As the signal continues negative, the diode between cathodes unhooks the two sections, thus limiting the output pulse to 0.25 volts into RG-114. With delay-line clipping, the wave forms indicated at the bottom of the figure are obtained. The 25 k Ω potentiometer allows adjustment of the quiescent point on the tunnel diode characteristic, and hence a small adjustment in the pick-off voltage. See page 11 for further details.

Figure 8 shows the results of tests made on the angular distribution apparatus.

Figure 8A shows the gain change in channels per 100 induced in the photomultiplier by stray magnetic fields as a function of the detector angle. An error bar shows the accuracy of the measurements. Additional details are given on page 13.

Figure 8B shows the excitation function for the 3.56-Mev gamma rays from $\text{Be}^9(p, \alpha\gamma)\text{Li}^6$. The resonance energy, E_r , marked on the abscissa has been calculated from the data in this figure by assuming a value of $\Gamma = 40$ kev for the total width of the resonance.

Figure 8C shows a representative angular distribution for the isotropic 3.56-Mev gamma rays from $\text{Be}^9(p, \alpha\gamma)\text{Li}^6$. The data has been normalized to unity at 0° . The line through the experimental points is the expected behavior of a point source displaced by 0.044" towards the north (the 90° point) from the center of rotation of the 4" x 4" NaI crystal. Additional information relating to figures 8A and 8B is given on page 15 of the text.

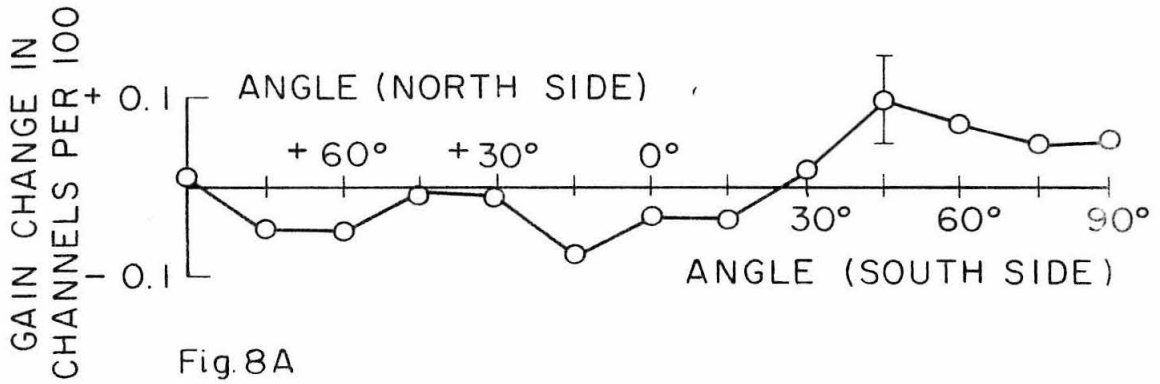


Fig. 8A

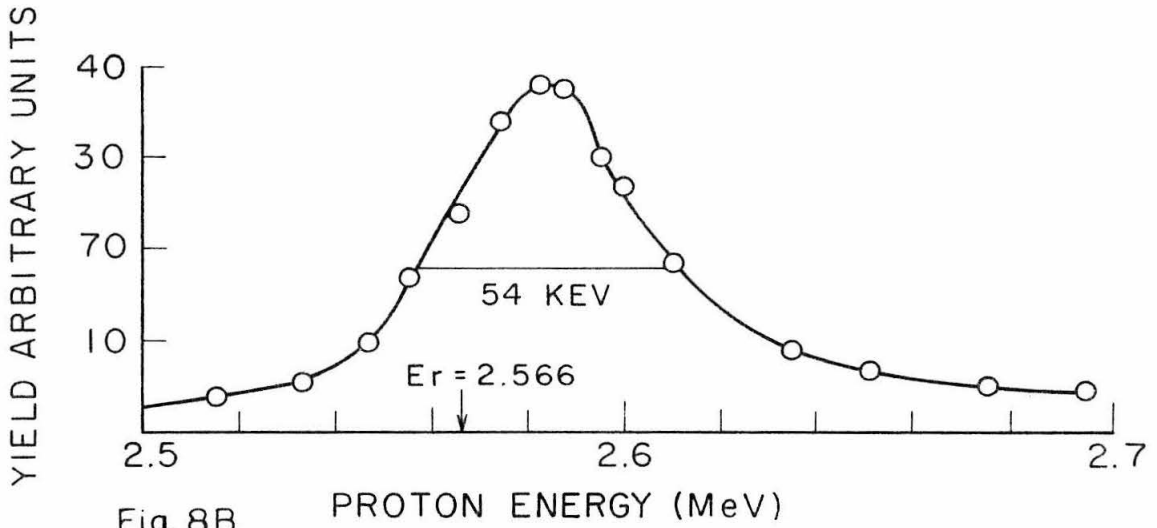


Fig. 8B

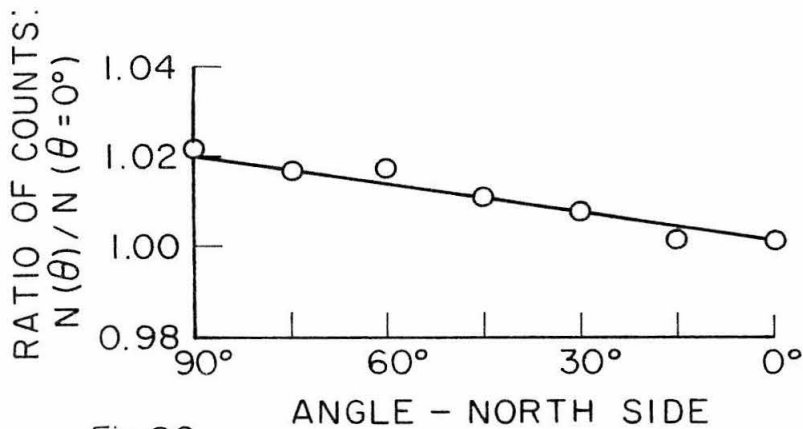


Fig. 8C

Figure 9 shows the 6.13-Mev radiation from the 597 kev resonance in $F^{19}(p, \alpha)O^{16}$. This spectrum was obtained with the 4" x 4" NaI(Tl) detector, without collimator, placed 1" from the target. The lines marked (a) and (b) are, respectively, the horizontal and zero intercept extrapolations of the low energy tail. Additional details are given on page 16.

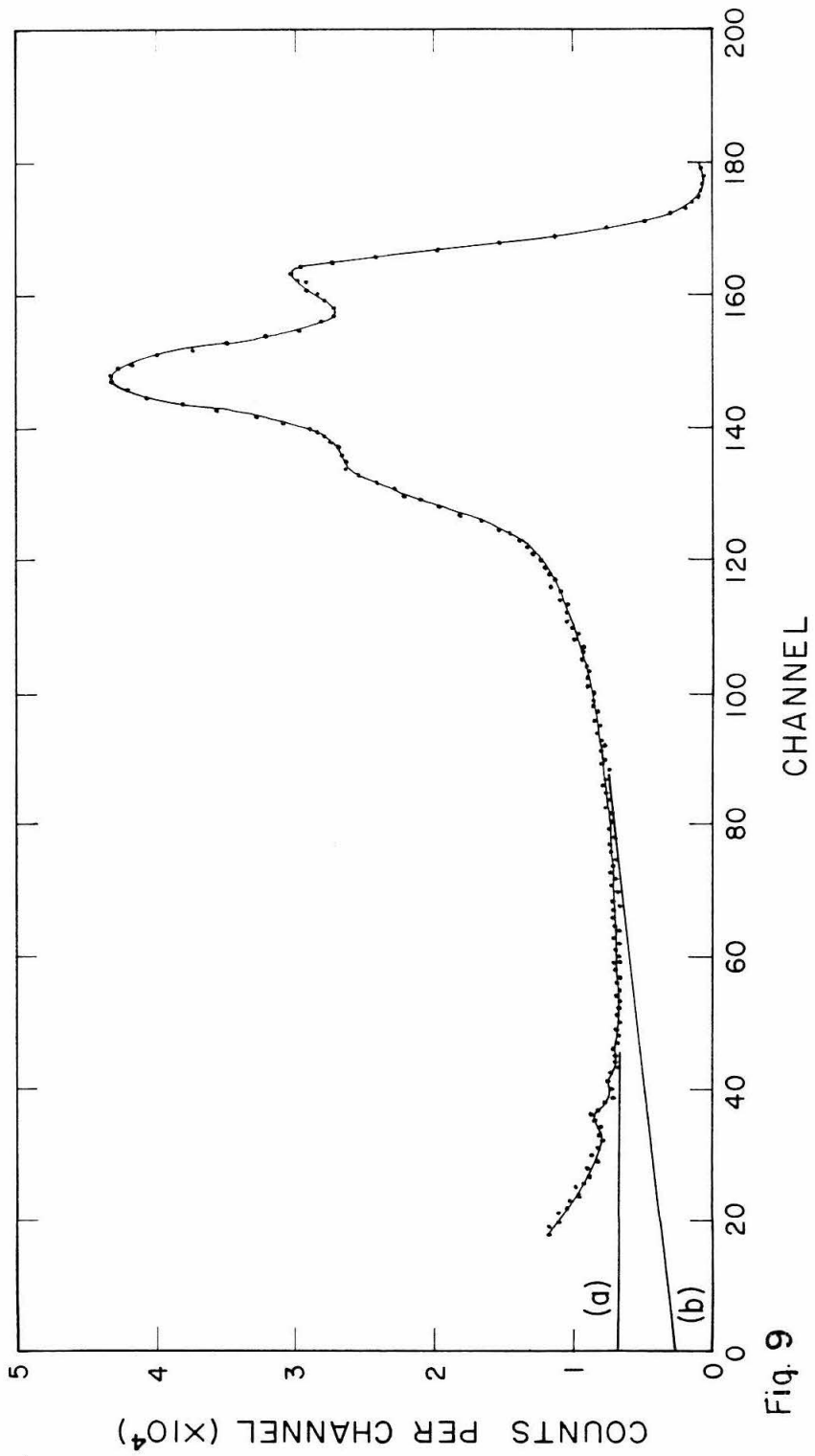


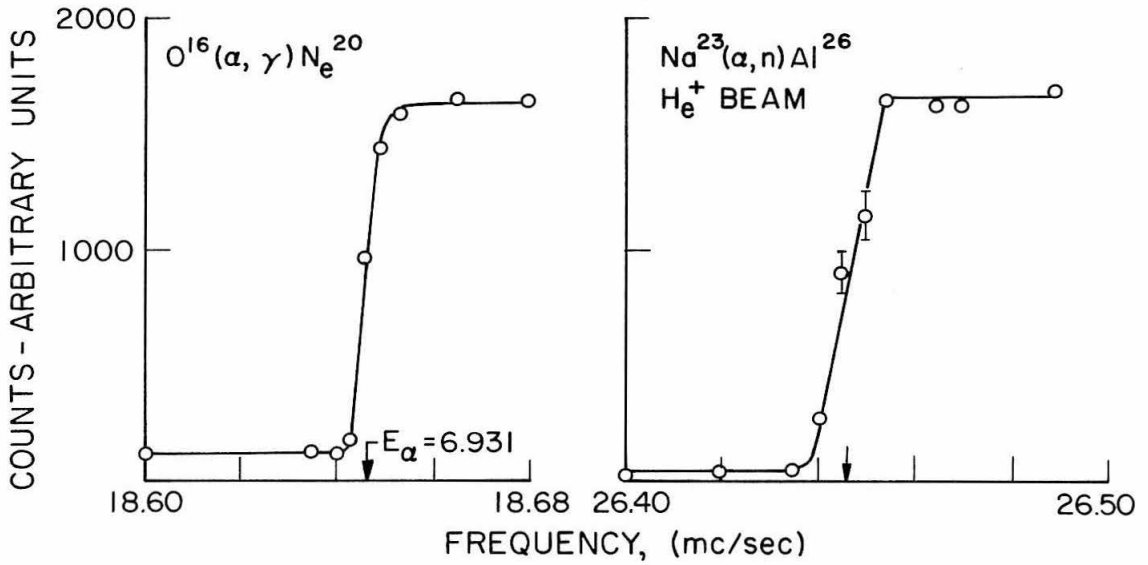
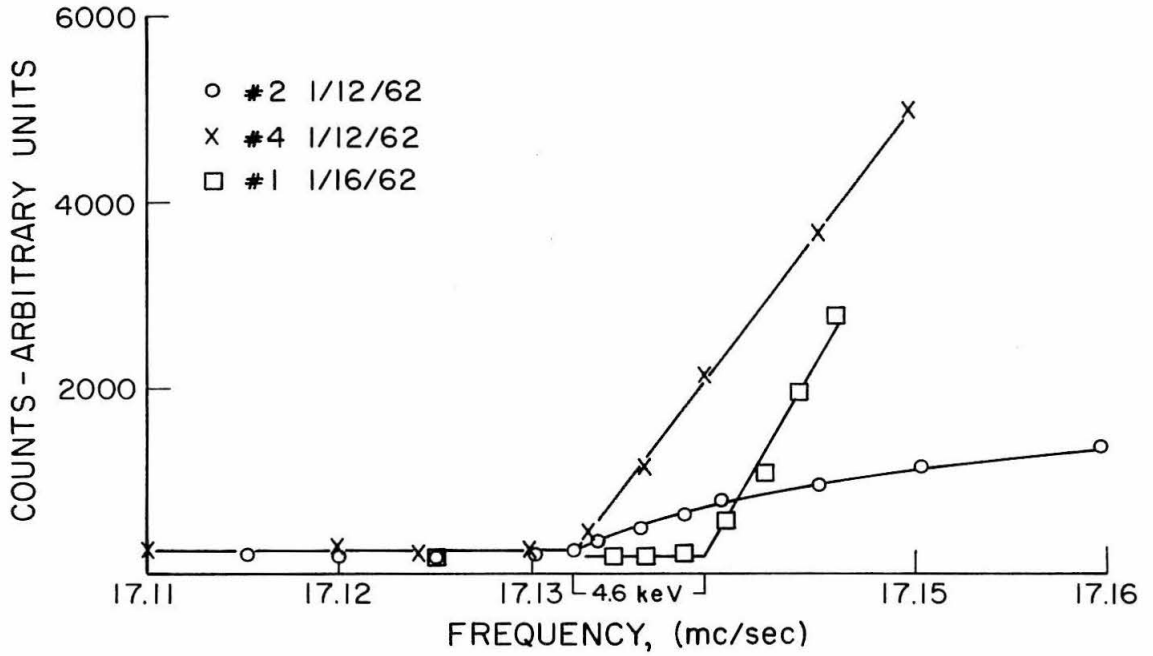
Fig. 9

Figure 10 shows representative data obtained during the calibration runs. Data for the $Al^{27}(p,n)Si^{27}$ threshold at 5798 ± 4 kev are plotted at the top. Three runs are represented in this plot; runs #4 of 1/12/62 and #1 of 1/16/62 were made with a 1" thick moderator in front of the neutron detector, run #2 of 1/12/62 was made without the moderator. A typical excitation curve for neutrons from the $Na^{23}(\alpha,n)Al^{26}$ resonance at 3492 ± 5 kev run with the He^+ beam is shown in the center right of the figure.

A summary of the values obtained from these reactions for the magnet constant defined on page 22 is given at the bottom of the figure. The best value, $1996.8 \pm 3 \times 10^{-5}$, is shown by an arrow on the abscissa.

A typical thick target excitation curve for the $O^{16}(\alpha,\gamma)Ne^{20}$ resonance at 6.93 Mev obtained during the same sequence of runs is shown at the center left. From this run and similar runs, the resonant energy is 6.930 ± 0.010 Mev.

There is a further discussion of the results and procedures used in obtaining this data in the text on page 19.



SUMMARY of RESULTS

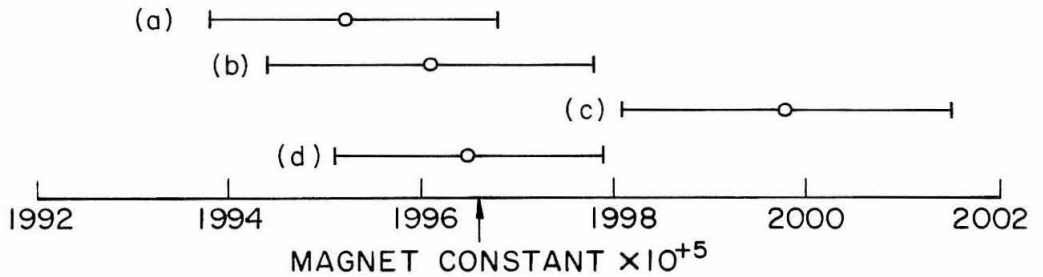


FIG. 10

Figure 11 is the excitation function for the $O^{16}(\alpha, \gamma)Ne^{20}$ reaction for alpha-particle bombarding energies: 4.8 to 7.2 Mev. The number of counts in the variable energy window, $0.86(E_x - 1.63)$ Mev to $1.10 E_x$ Mev, for 300 μ C of He^{++} is plotted against the bombarding energy, E_α , and the excitation energy, E_x , in Ne^{20} . The range covered by the variable energy window is shown on the gamma-ray spectrum in figure 13.

The target used for this excitation function was anodized tantalum with an oxide layer 51 kev thick to 7 Mev alpha particles. The detector was a 4" x 4" NaI crystal placed 1.06" from the target at 0° with respect to the beam direction. See page 23 for further details.

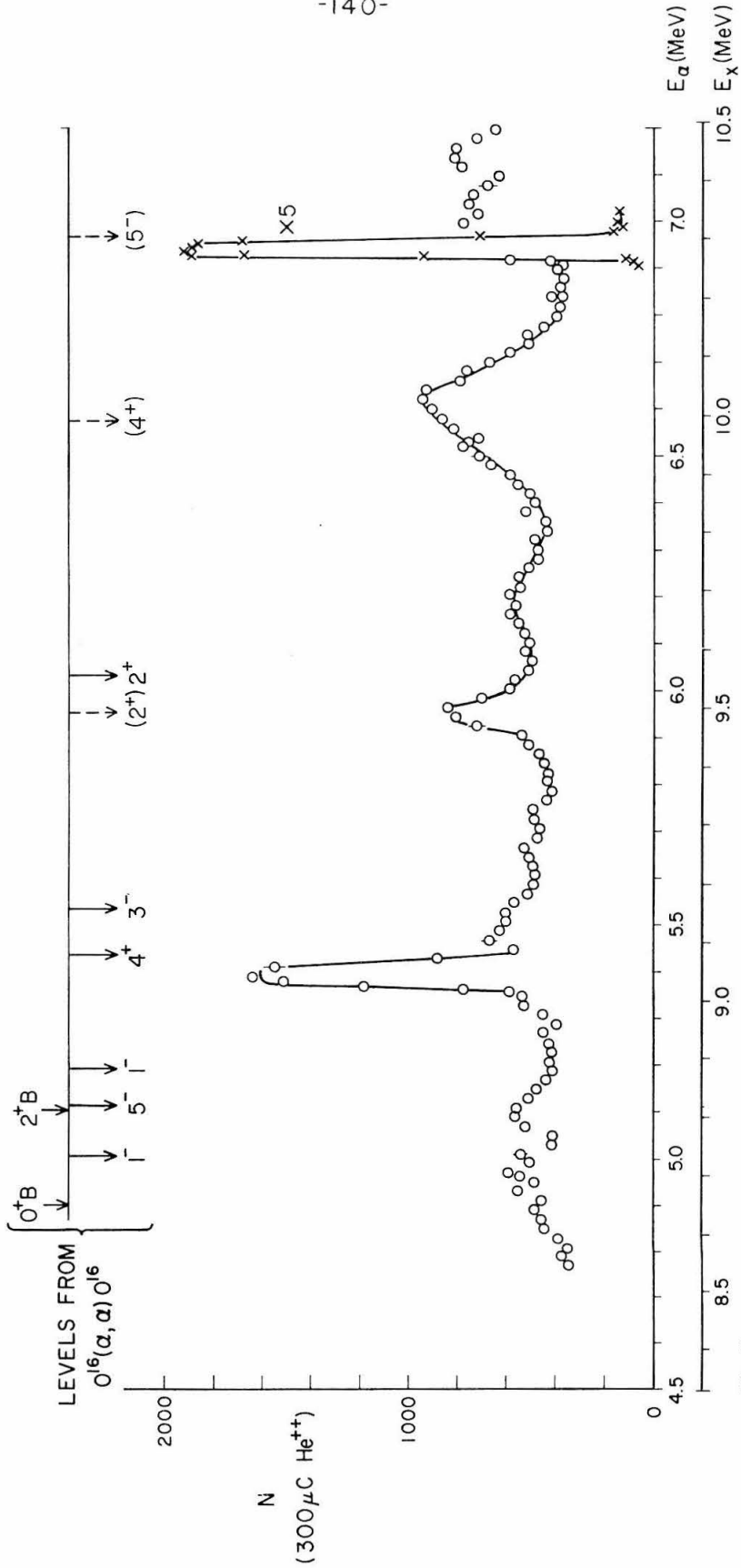


Fig. 11

Figure 12 is the excitation function for the $O^{16}(\alpha, \gamma)Ne^{20}$ reaction for alpha-particle bombarding energies 7.2 to 9.9 Mev. The number of pulses in the energy window $0.86(E_x - 1.63)$ Mev to $1.10 E_x$ Mev for $150 \mu C$ of He^{++} is plotted against the bombarding energy, E_α , and the excitation energy, E_x , in Ne^{20} . The target was oxidized tungsten with an oxide layer 55 kev thick to 7 Mev alpha particles. The detector was a $4'' \times 4''$ NaI crystal placed $1.06''$ from the target at 45° with respect to the beam direction. This excitation function is a continuation of the excitation function in figure 11. Additional details are given on page 26.

Figure 13 shows the 7.40-Mev gamma-ray spectrum from the 5.37-Mev resonance in $O^{16}(\alpha, \gamma)Ne^{20}$. The filled curve was obtained at 5.40 Mev and the dotted curve at 5.30 Mev bombarding energy. The gamma rays were detected in a 4" x 4" NaI crystal placed 0.75" from the target at 45° to the beam direction. The target was an oxidized tungsten blank with an oxide layer 115 kev thick to alpha particles of this energy. Further details are given on page 28.

The variable energy window used to derive the excitation function shown in figures 11 and 12 is illustrated by the bar above the abscissa for the alpha-particle bombarding energy, $E_\alpha = 5.40$ Mev, corresponding to an excitation energy, $E_x = 9.05$ Mev, in Ne^{20} . This window covers the energy range $0.86(E_x - 1.63)$ Mev to $1.10 E_x$ Mev in the gamma ray spectrum. Hence, this window includes the photo-peaks of the gamma-ray spectrum from transitions to the ground state and the full energy peak, first escape peak, and roughly half of the second escape peak of the gamma-ray spectrum from transitions to the first excited state of Ne^{20} . Additional details are given on page 23.

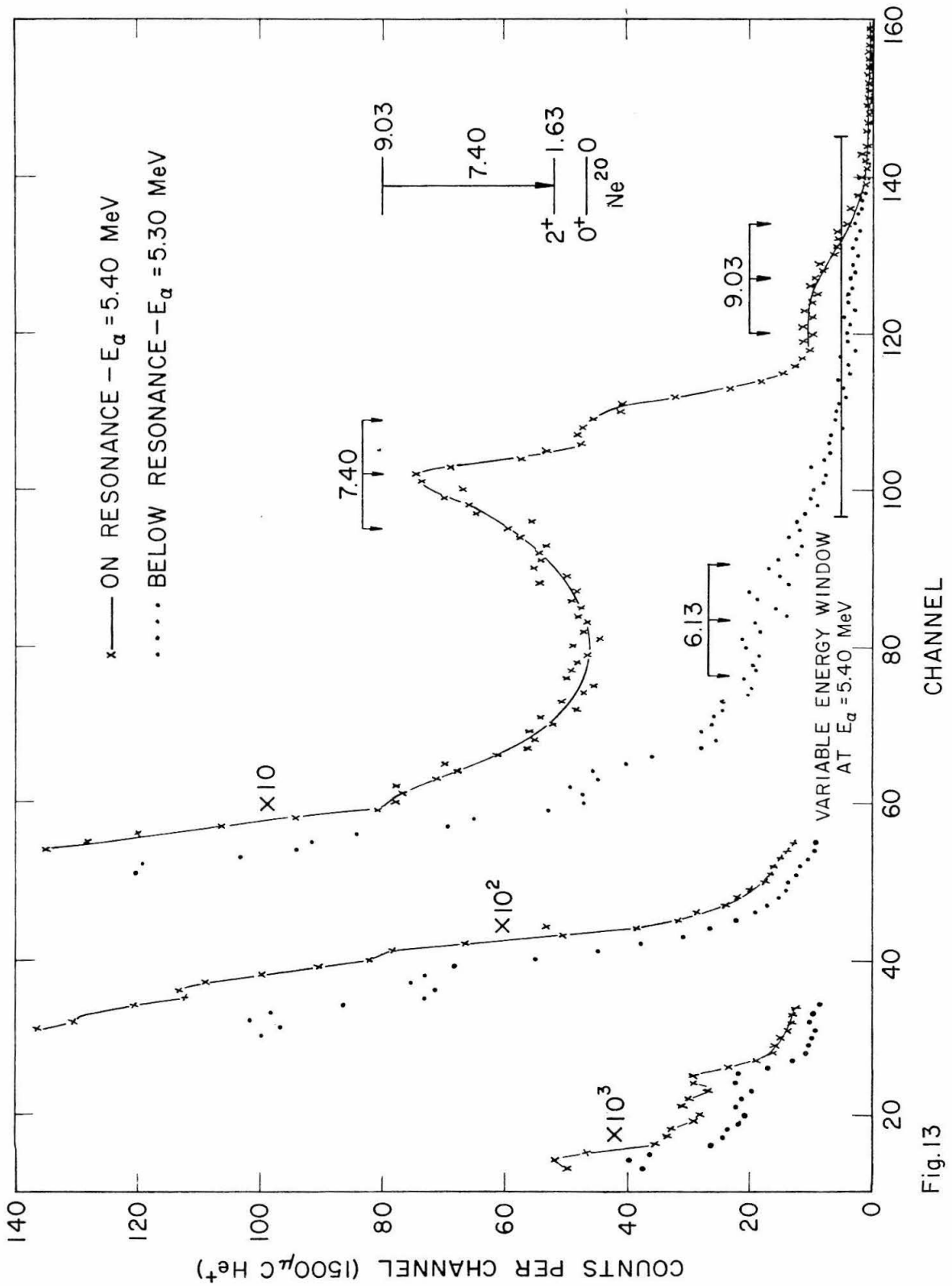


Fig.13

Figure 14 is the excitation function for 7.40-Mev gamma rays from the 5.37-Mev resonance. The ordinate is the number of counts in the energy window 6.56 Mev to 8.58 Mev for 90 μC of integrated beam current. The upper curve was obtained with the He^+ beam, and the lower curve with He^{++} . Values for the resonant energy determined from these excitation functions are indicated on the abscissa. Arrows marked BELOW and ON indicate the energy relationship of angular distribution runs made on and below resonance. Further details are given on pages 29 and 31 in the text.

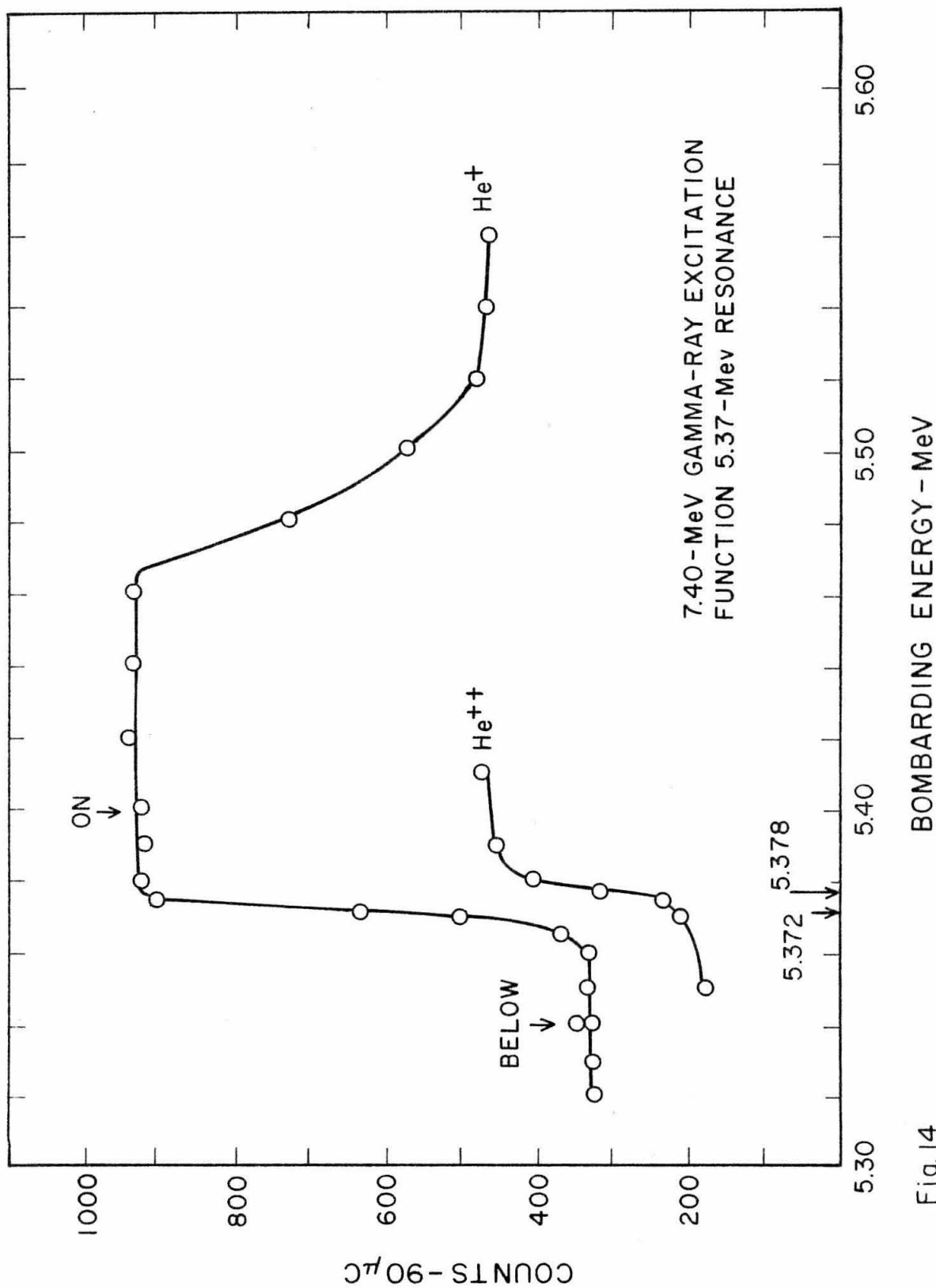


Fig. 14

Figure 15 shows the results of angular distribution measurements on the 7.40-Mev gamma ray from the 5.37-Mev resonance in $O^{16}(\alpha, \gamma)Ne^{20}$, together with the least squares fit. The number of counts in the energy window, 6.56 to 8.58 Mev for 600 μC of He^+ are plotted against the cosine of the angle between the NaI detector and the beam direction. The upper data points are the uncorrected data included to show the ability of the apparatus to resolve a $P_4(\cos \theta)$ term in an angular distribution. The smooth curve through the corrected data points is a least squares fit which is:

$$\begin{aligned} \text{counts} = & 967 \{ 1 + (0.439 \pm 0.052)P_2(\cos \theta) \\ & - (0.243 \pm 0.057)P_4(\cos \theta) \} \end{aligned}$$

Further details are given on page 30.

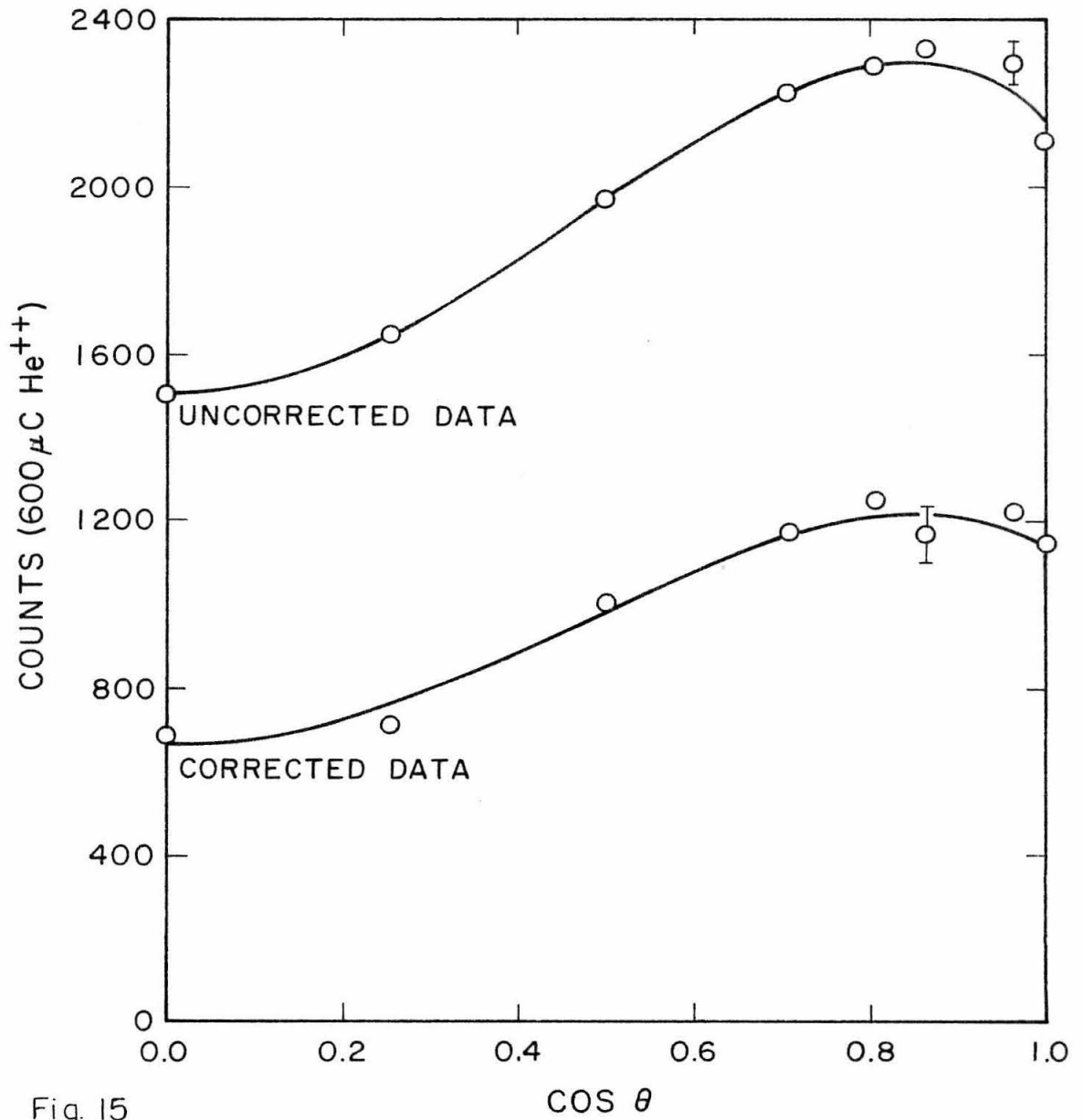


Fig. 15

Figure 16 shows gamma-ray spectra obtained during angular distribution measurements made on the 8.64-Mev gamma ray from the 6.93-Mev resonance in $O^{16}(\alpha, \gamma)Ne^{20}$. The filled curve was made on resonance, and the dotted curve below resonance. The energy relationship of the two runs is shown on the excitation function in figure 17. Additional details are given on page 37 of the text.

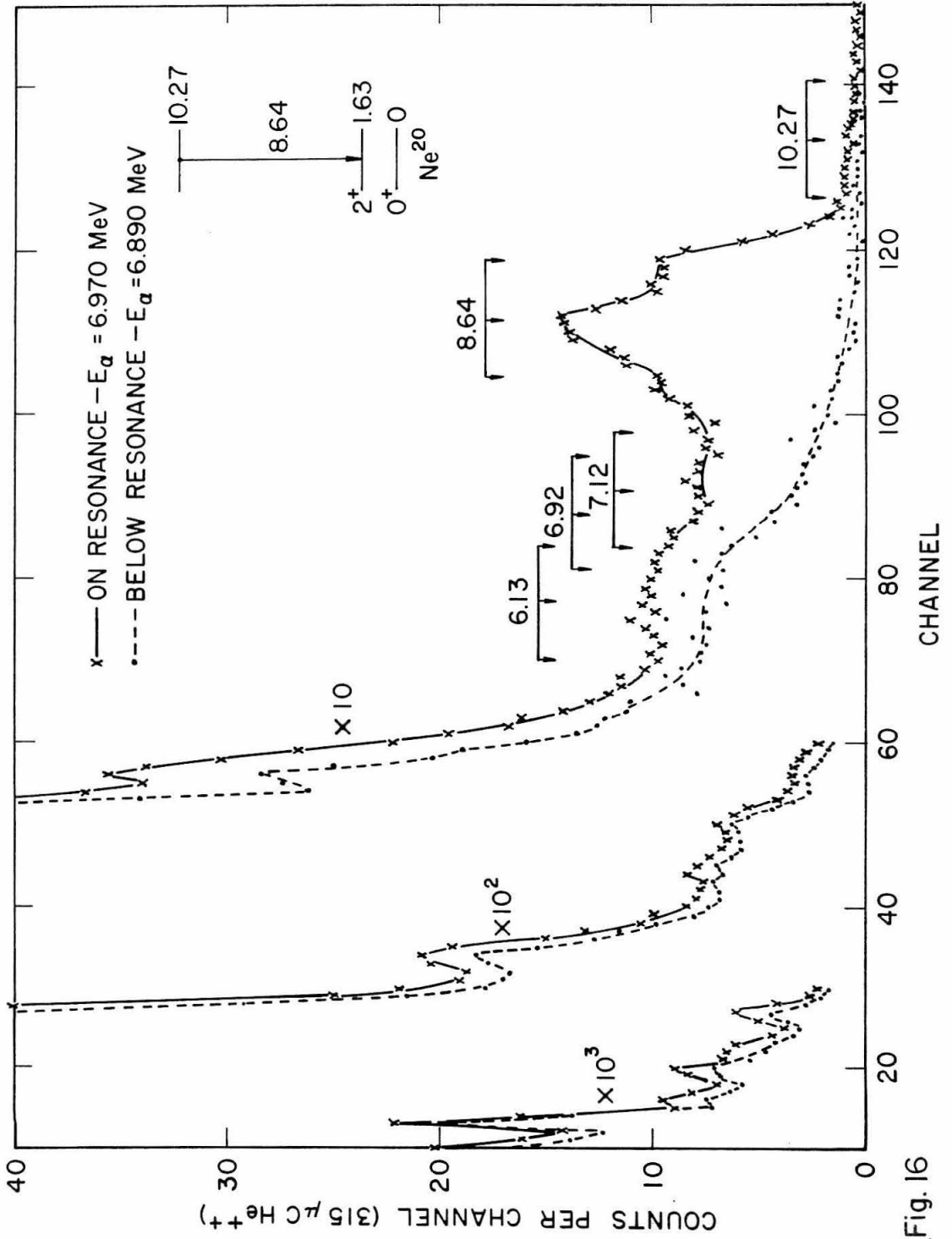


Fig. 16

Figure 17 shows the results of angular distribution measurements on the 8.64-Mev gamma ray from the 6.93-Mev resonance in $O^{16}(\alpha, \gamma)Ne^{20}$, together with the least squares fits. The corrected number of counts in the energy window, 6.90 to 9.07 Mev, for 240 μC of He^{++} are plotted against the cosine of the angle between the NaI detector and the beam direction. The smooth curve through the data points is the result of a least squares analysis which gave:

$$\begin{aligned} \text{counts} = 1648 \{ & 1 + (0.475 \pm 0.025)P_2(\cos \theta) \\ & + (0.004 \pm 0.031)P_4(\cos \theta) \} \end{aligned}$$

The lower curve marked "BACKGROUND" is the estimated background obtained by interpolating between angular distribution measurements made below and above resonance. The energy relationship of the three measurements is shown on the excitation function for the 8.64-Mev gamma ray inserted at the top of the figure. This background has been removed from the corrected data at the top of the figure. Further details are given on page 38.

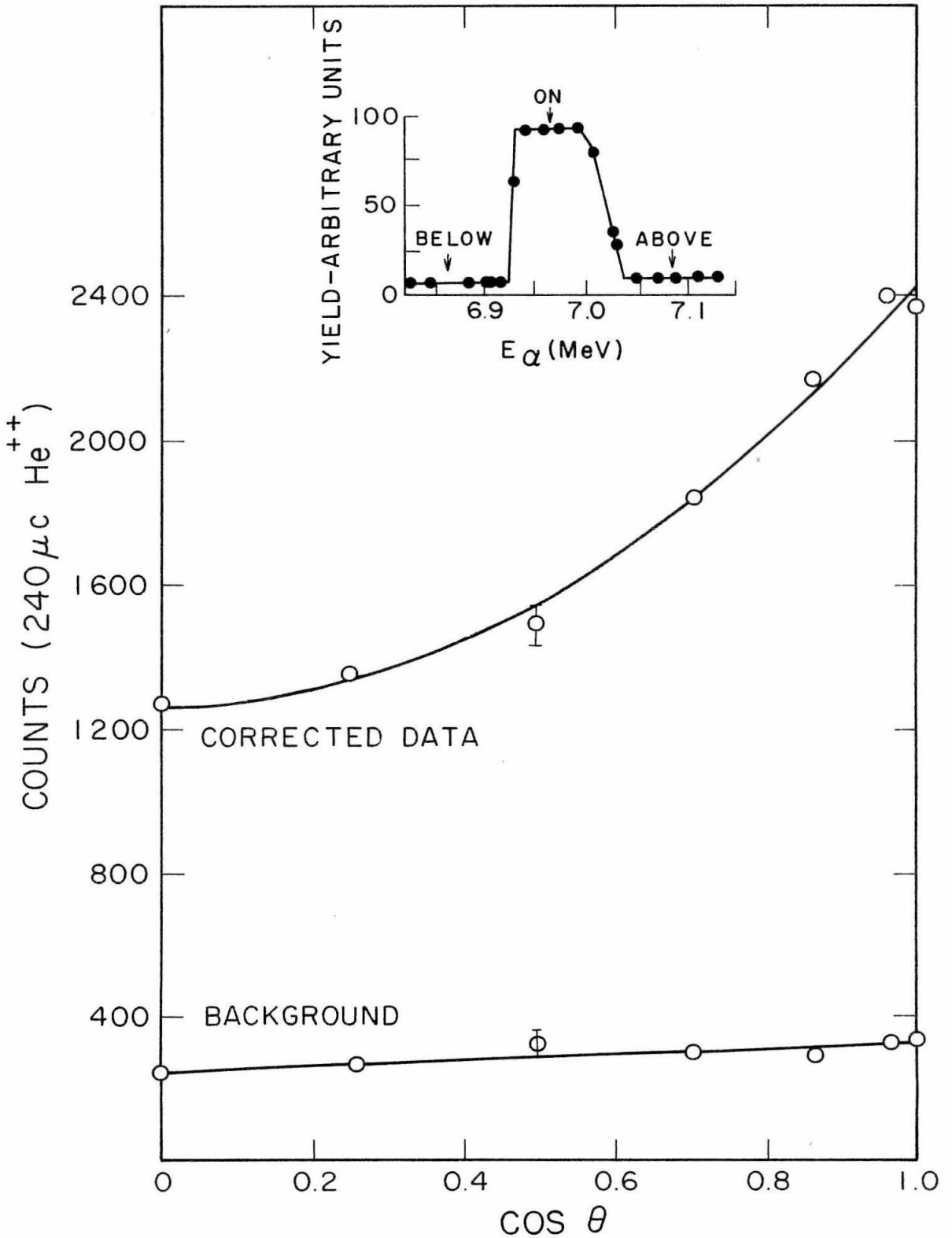


Fig.17

Figure 18 shows experimental and theoretical values for the Legendre polynomials in the expression for the angular distribution for the 8.64-Mev gamma ray:

$$W(\theta) = 1 + a_2/a_0 P_2(\cos \theta) + a_4/a_0 P_4(\cos \theta)$$

from the 6.93-Mev resonance in $O^{16}(\alpha, \gamma)Ne^{20}$. The theoretical values are plotted against the mixing coefficient δ , which is defined as the ratio of the reduced matrix elements for the E2 to M1 operators. The two possible values for the coefficient of the second Legendre polynomial that depend on the sign of δ are marked $\delta > 0$ and $\delta < 0$. The horizontal bands are the experimental values, where the width of the band is the experimental uncertainty. Additional discussion is given on page 39 of the text.

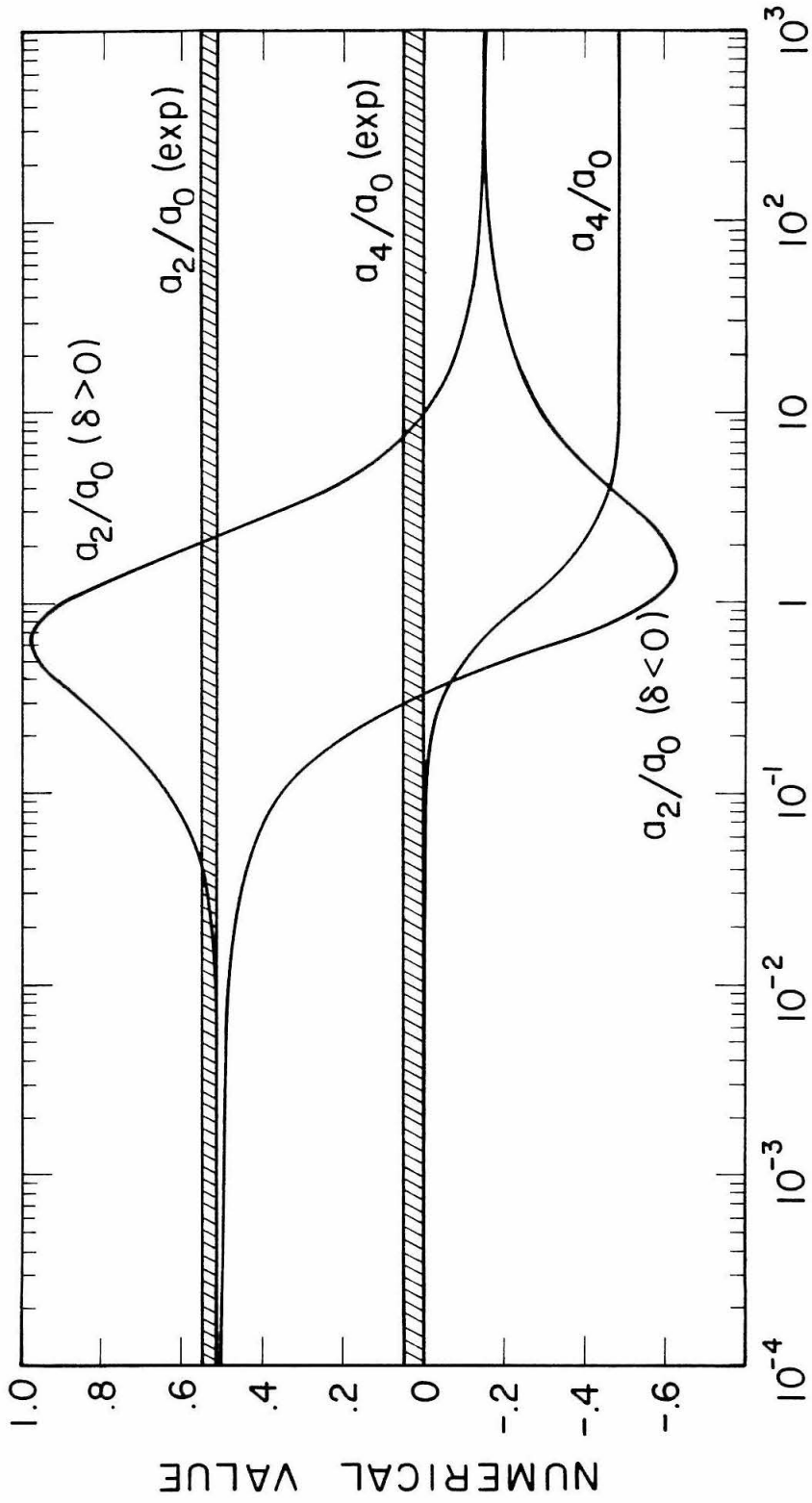


Fig. 18
MIXING COEFFICIENT; δ

Figure 19 shows gamma-ray spectra obtained during coincidence measurements of the radiations from the 6.93-Mev resonance in $O^{16}(\alpha, \gamma)Ne^{20}$. Shown in A is the singles spectrum for the high energy gamma rays detected in a 3" x 3" NaI crystal; shown in B is the singles spectrum for the low energy gamma rays detected in a 4" x 4" NaI crystal. The spectrum in C was shifted out of A on the condition that there was a fast coincidence with a low energy gamma ray in the window shown in B. Likewise, spectrum D was shifted out of B on the condition that there was a coincidence with a high energy gamma ray above 3.85 Mev. The main features of the coincidence spectra are the 8.63 - 1.63-Mev cascade from the 10.27-Mev level in Ne^{20} . More complicated cascades starting at the 10.27-Mev level and going through the 1.63-Mev first excited state do not show up clearly in the high energy coincidence spectrum shown in C. The transitions discussed on page 44 of the text are the 6.02-Mev, E2 transition to the 4^+ second excited state (see figure 1) that is expected to have a full-energy peak in channel 78, and the 5.30-Mev, E1 transition to the 2^- , third excited state that is expected to have a full-energy peak in channel 69. Probable sources for some of the low energy gamma rays have been noted on B. Additional details are given on pages 43 to 47 of the text.

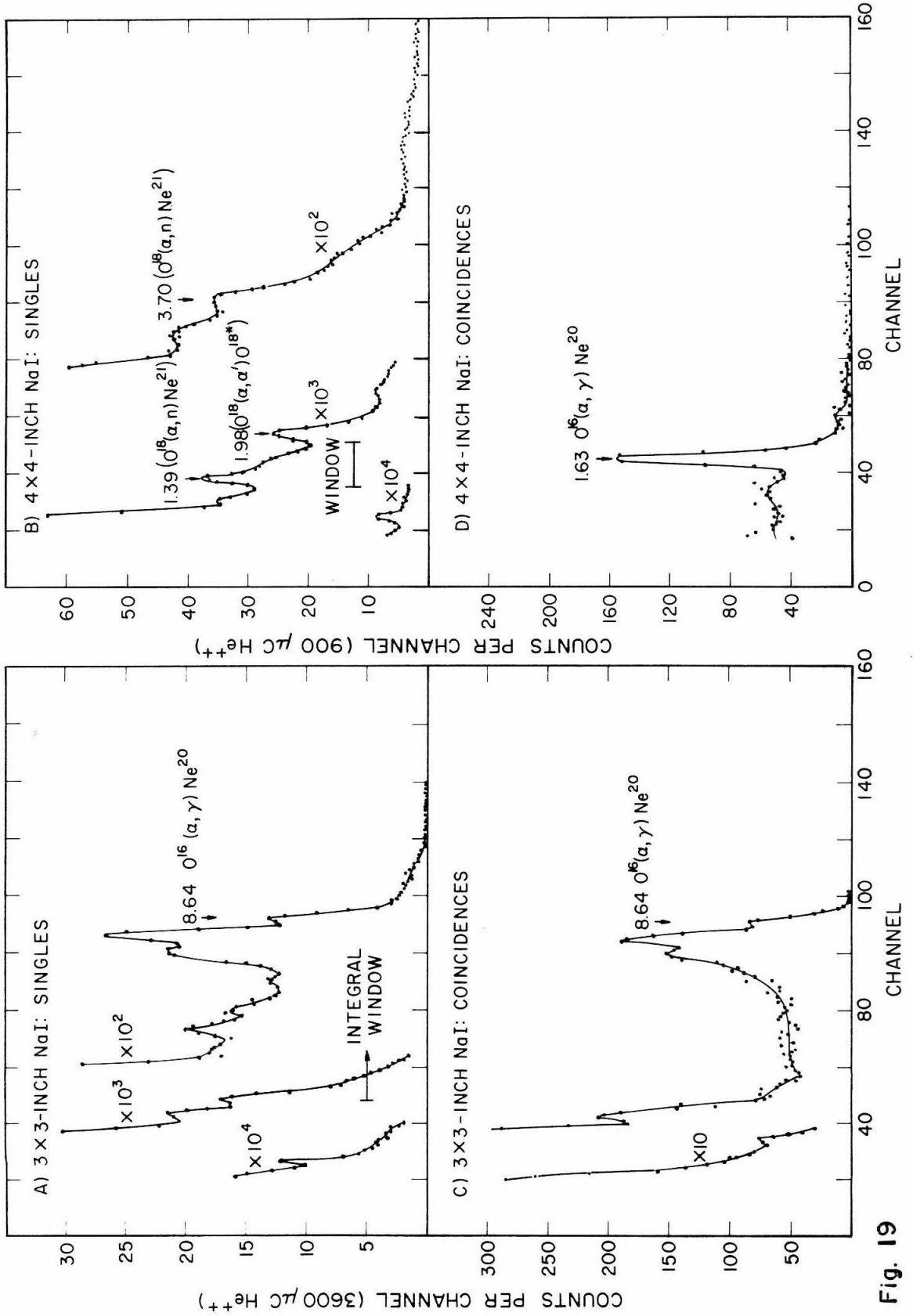


Fig. 19

Figure 20 shows the results of α - γ - γ triple angular correlation measurements made at the 6.93-Mev resonance in the $O^{16}(\alpha, \gamma)Ne^{20}$ reaction. A sketch of the experimental arrangement is shown at the top of the figure. The coincidence circuit biases were arranged so that the 8.64-Mev gamma rays were detected in the 4" x 4" NaI crystal, and the 1.63-Mev gamma rays were detected in the 2" x 2" NaI crystal. Plotted are the number of coincidence counts as a function of the cosine of the angle between the 4" crystal and the beam direction. The smooth curves are the calculated patterns for various spin and gamma-ray multipolarities for the specific geometry of the counters. These curves have been adjusted in amplitude by least squares to the data points. The quality of the fit has been judged by the χ^2 test, and the results are:

<u>Pattern</u>	<u>Transition</u>	<u>χ^2</u>	<u>Probability</u>
1	$0^+(E2)2^+(E2)0^+$	90.0	$\ll 1\%$
2	$1^-(E1)2^+(E2)0^+$	60.6	$\ll 1$
3	$2^+(M1)2^+(E2)0^+$	1.57	96
4	$2^+(E2)2^+(E2)0^+$	91.2	$\ll 1$
5	$3^-(E1)2^+(E2)0^+$	175.	$\ll 1$
6	$4^+(E2)2^+(E2)0^+$	6.76	33

Additional discussions are given on page 47 of the text and in Appendix A.

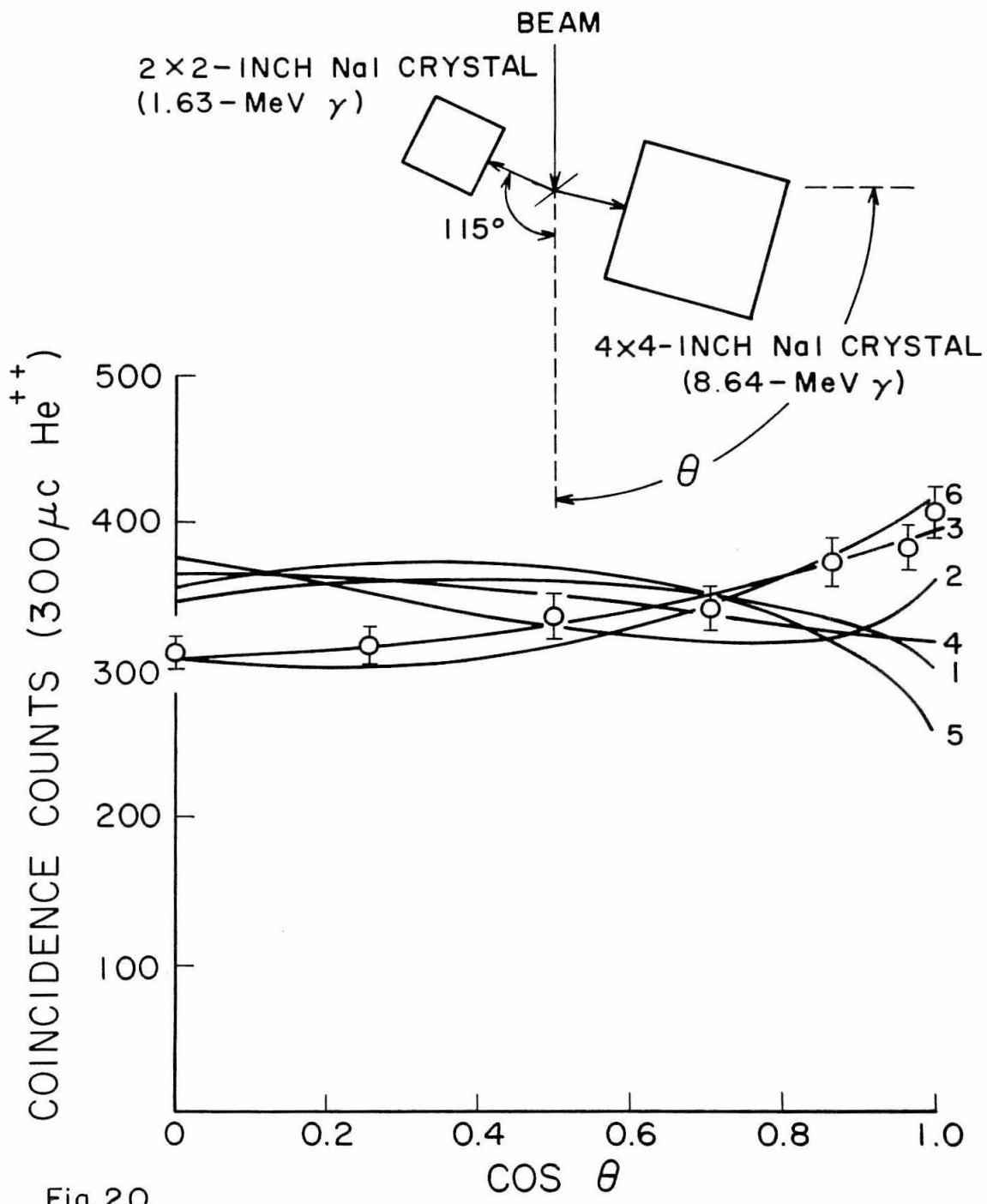


Fig. 20

Figure 21 shows gamma-ray spectra obtained above, on, and below the 7.94-Mev resonance in $O^{16}(\alpha, \gamma)Ne^{20}$. The energies were 8.027-, 7.953-, and 7.910-Mev bombarding energy. These three energies are indicated by arrows on the excitation function for the 6.83-Mev gamma ray shown in figure 22A. These spectra were obtained during angular distribution measurements on the 6.83-Mev gamma ray; the NaI crystal was equipped with a collimator. The small energy level diagram shows the cascade in Ne^{20} that gives rise to the 6.83-Mev gamma ray. See the discussion on page 54 for further details.

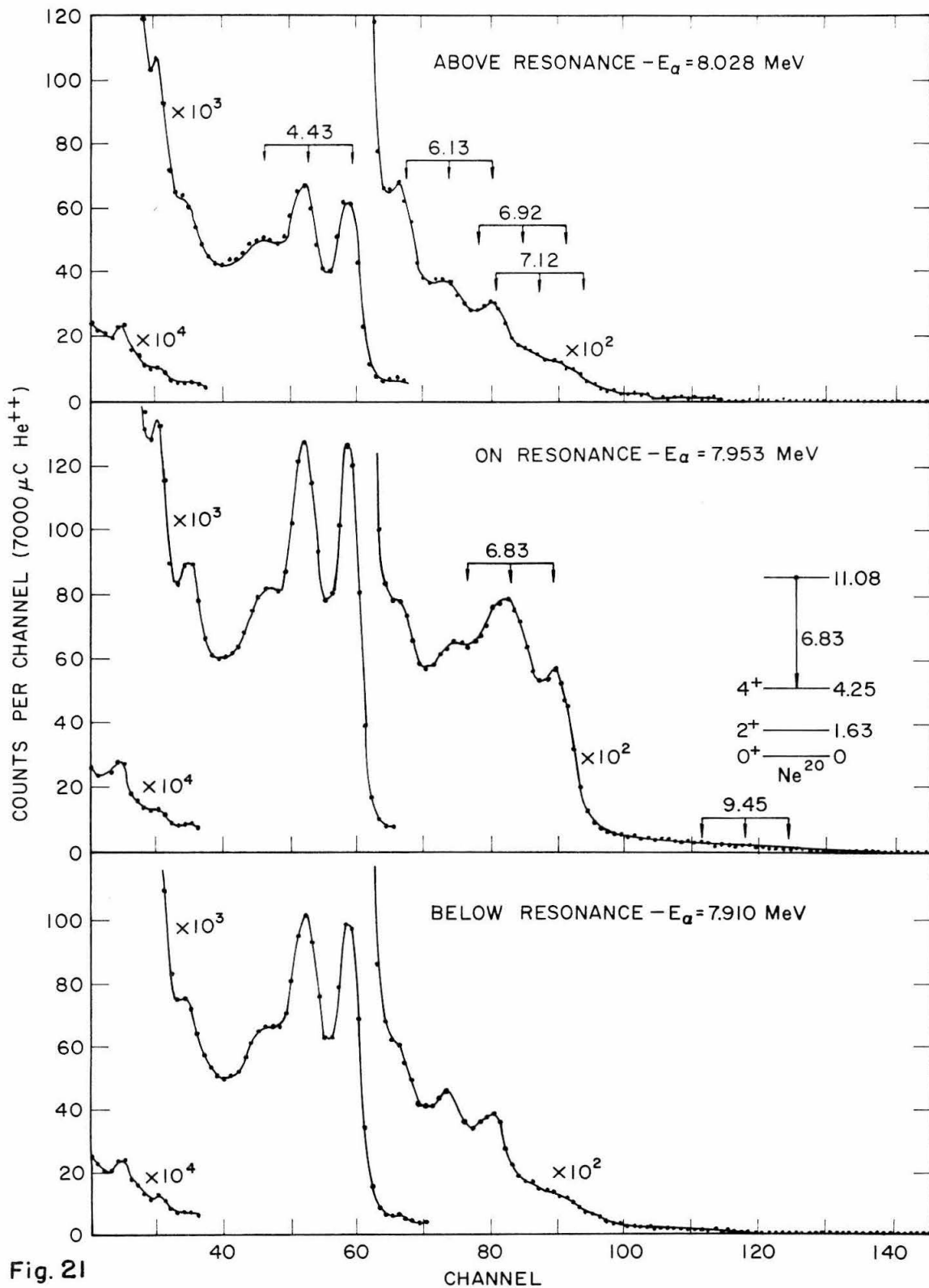


Fig. 21

Figure 22 shows two excitation functions for the 6.83-Mev radiation from the 7.94-Mev resonance in $O^{16}(\alpha, \gamma)Ne^{20}$. Figure 22A is an excitation function obtained with the 4" x 4" NaI crystal by summing the counts in the gamma-ray spectra falling in the energy window, 6.29 to 7.40 Mev. The resonance energy indicated by the half-way point on the low energy side is shown by an arrow on the abscissa. This excitation function was obtained prior to angular distribution measurements discussed on page 56. These measurements were made below, on and above resonance at energies indicated on the excitation function by arrows.

The excitation function shown in figure 22B was an attempt to determine the resonance energy and find the total width of the 7.94-Mev resonance. The resonance energy is marked on the abscissa; the 1/4 to 3/4 rise of this excitation function is 3.2 kev. The data was obtained with a 3" x 3" NaI crystal, and is the number of counts in the energy window 6.29 to 7.20 Mev.

Additional details relating to figures 22A and B are given on page 55 of the text.

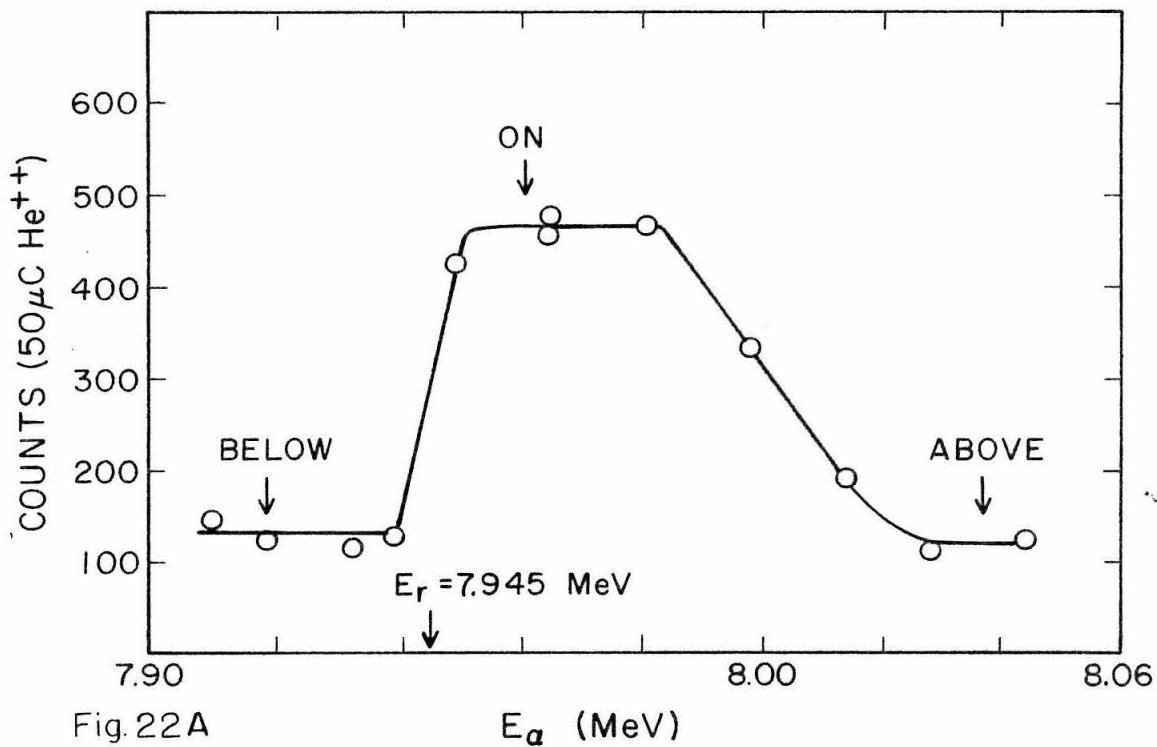


Fig. 22A

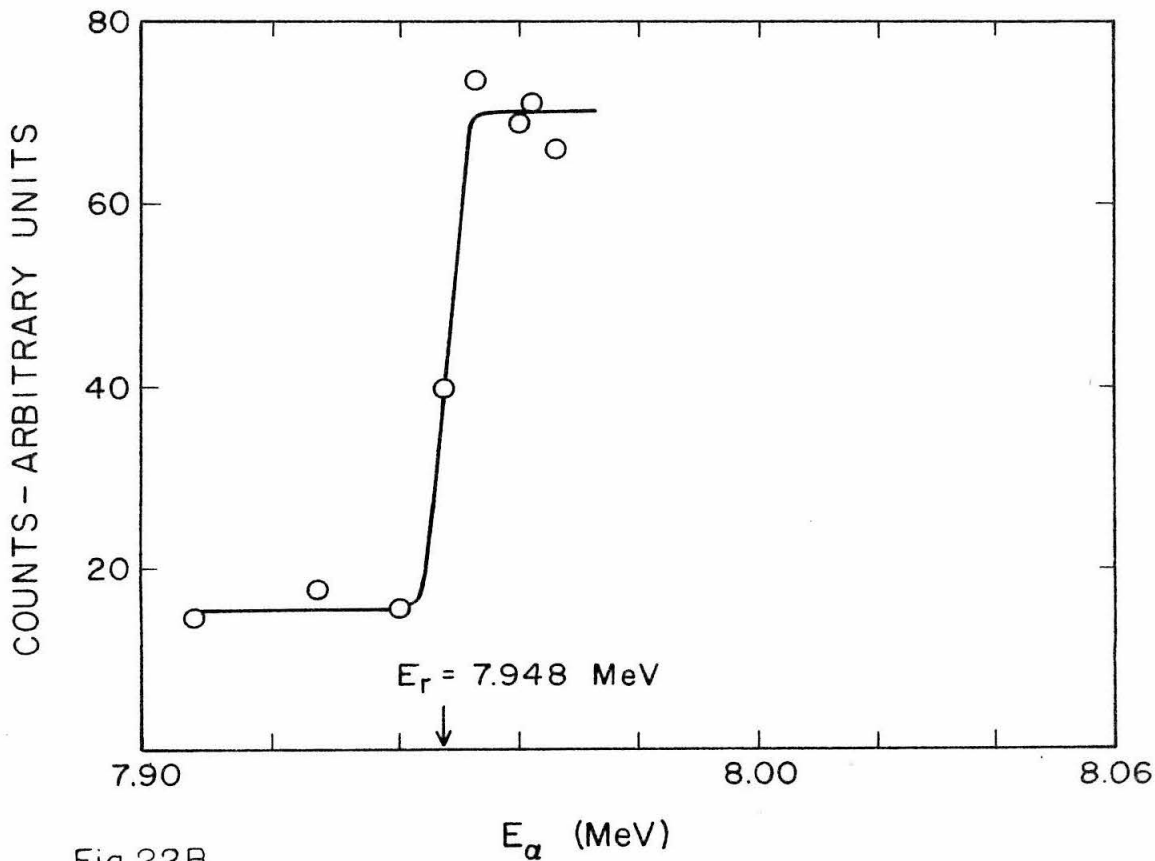


Fig. 22B

Figure 23 shows the results of angular distribution measurements on the 6.83-Mev gamma ray from the 7.94-Mev resonance in $O^{16}(\alpha, \gamma)Ne^{20}$, together with the least squares fits. The corrected number of counts in the energy window 5.72 to 7.40 Mev for 500 μC of He^{++} are plotted against the cosine of the angle between the NaI detector and the beam direction. The smooth curve through the data points is the result of a least squares analysis which gave:

$$\begin{aligned} \text{counts} = 4989 \{ & 1 + (0.252 \pm 0.019)P_2(\cos \theta) \\ & - (0.033 \pm 0.024)P_4(\cos \theta) \} \end{aligned}$$

The lower curve marked "BACKGROUND" is the estimated background obtained by interpolating between angular distribution measurements made below and above resonance. The energy relationship of the three measurements is shown on the excitation function for the 6.83-Mev gamma ray given in figure 22A. This background has been removed from the corrected data at the top of the figure. Further details are given on page 56.

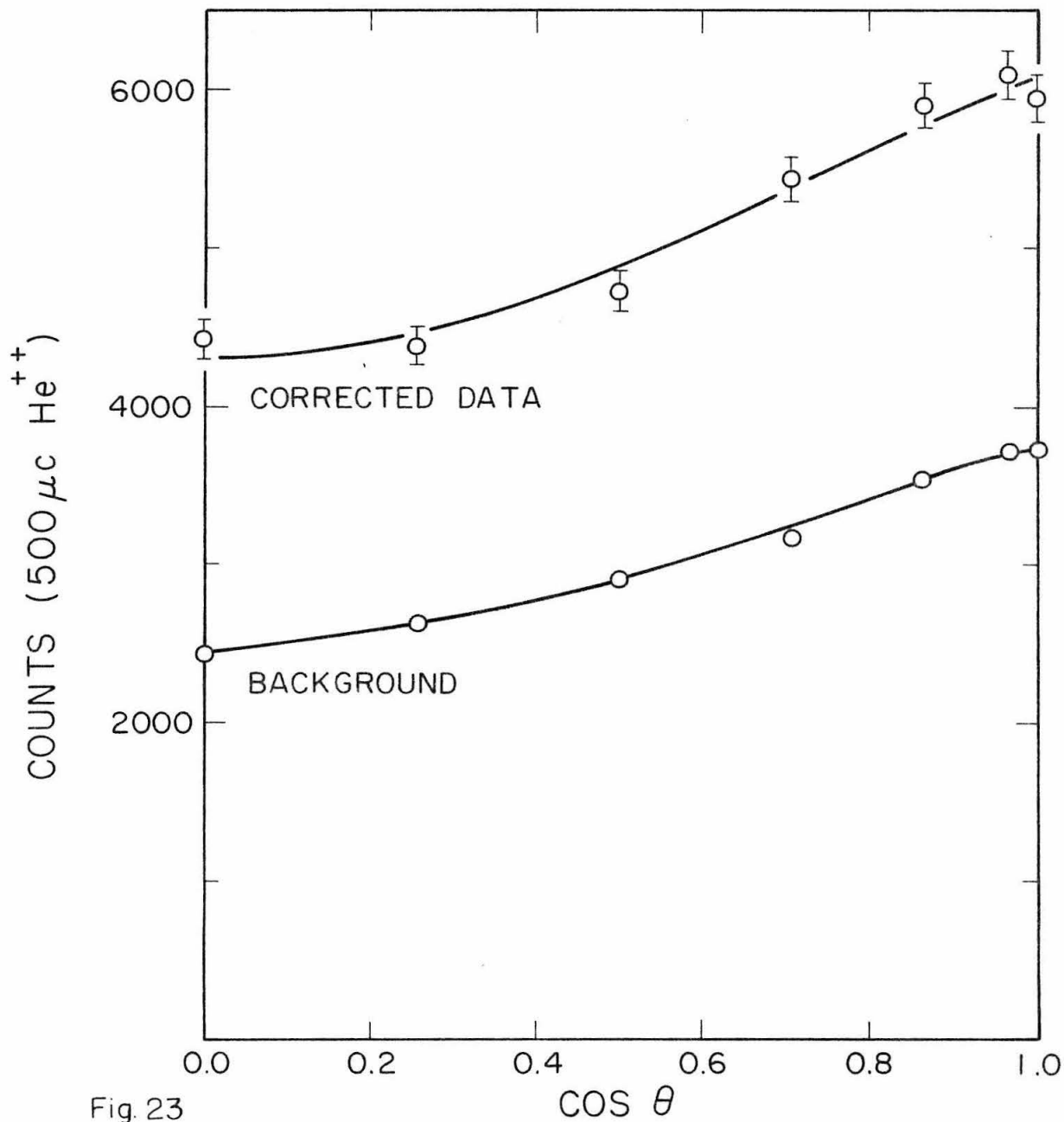


Fig. 23

Figure 24 shows the experimental and theoretical values for the Legendre polynomials in the expression for the angular distribution for the 6.83-Mev gamma ray:

$$W(\theta) = 1 + a_2/a_0 P_2(\cos \theta) + a_4/a_0 P_4(\cos \theta)$$

for the 7.94-Mev resonance in $O^{16}(\alpha, \gamma)Ne^{20}$. The theoretical values are plotted against the mixing coefficient δ , which is defined as the ratio of the reduced matrix elements for the E2 to M1 operators. The two possible values for the coefficient of the second Legendre polynomial that depend on the sign of δ are marked $\delta > 0$ and $\delta < 0$. The horizontal bands are the experimental values, where the width of the band is the experimental uncertainty. Additional discussion is given on page 58 of the text.

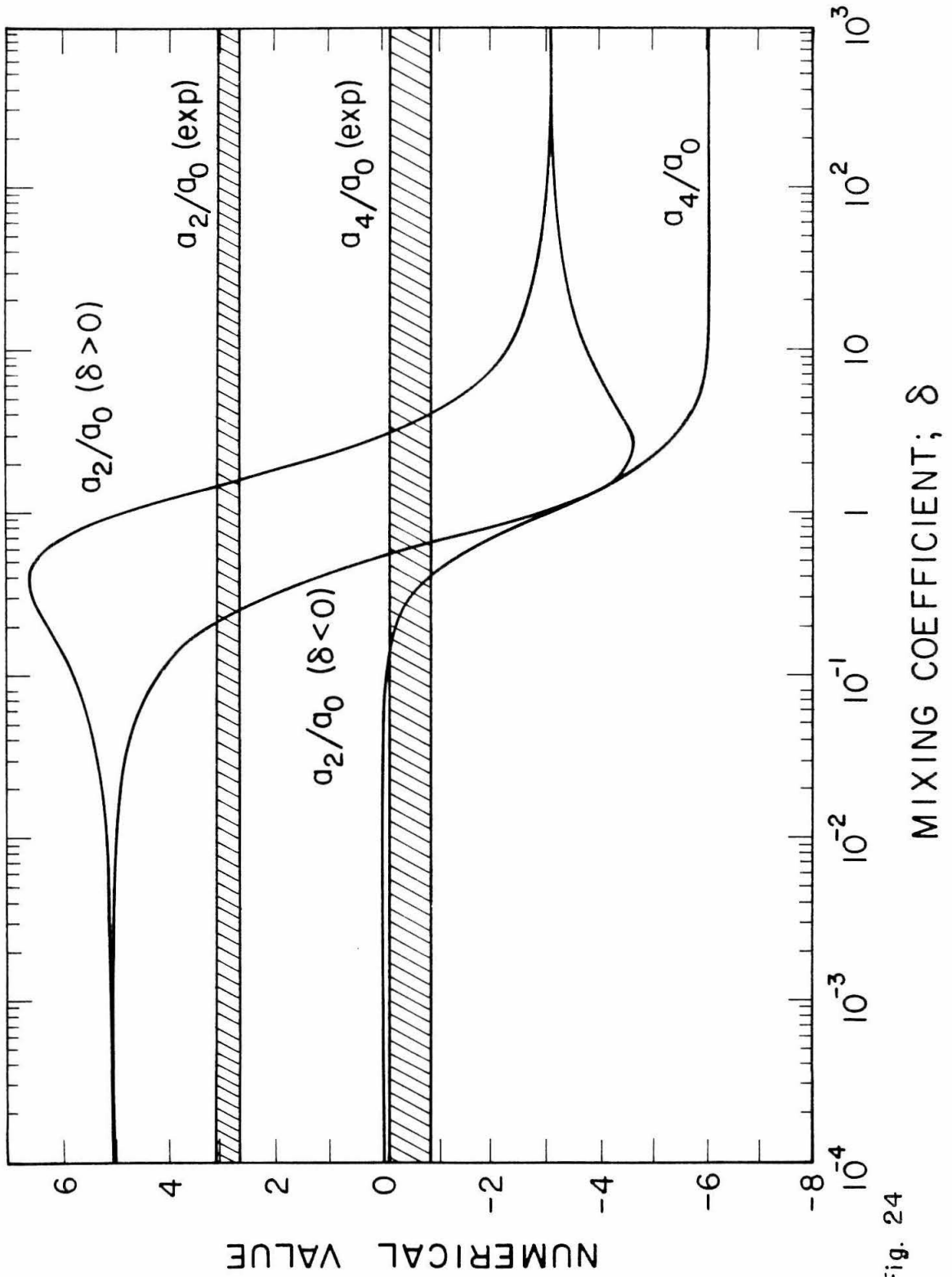


Fig. 24

Figure 25 shows the results of α - γ - γ triple angular correlation measurements made at the 7.94-Mev resonance in the $O^{16}(\alpha, \gamma)Ne^{20}$ reaction. A sketch of the experimental arrangement is shown at the top of the figure. The coincidence circuit biases were arranged so that the 6.83-Mev gamma rays were detected in the 4" x 4" NaI crystal, and the 2.62-Mev gamma rays were detected in the 2" x 2" NaI crystal. Plotted are the number of coincidence counts as a function of the cosine of the angle between the 4" crystal and the beam direction. The smooth curves are the calculated patterns for various spin and gamma-ray multipolarities for the specific geometry of the counters. These curves have been adjusted in amplitude by least squares to the data points. The quality of the fit has been judged by the χ^2 test, and the results are:

<u>Pattern</u>	<u>Transition</u>	<u>χ^2</u>	<u>Probability</u>
1	$4^+ \begin{matrix} M1 \\ E2 \end{matrix} 4^+ (E2) 2^+$	3.46	74%
2	$6^+ (E2) 4^+ (E2) 2^+$	2.02	92
3	$2^+ (E2) 4^+ (E2) 2^+$	3.05	81
4	$3^- (E1) 4^+ (E2) 2^+$	6.90	33
5	$5^- (E1) 4^+ (E2) 2^+$	13.0	4

The mixing coefficient used in calculating pattern 1 was the value determined from the angular distribution measurements on the 6.83-Mev gamma ray that are discussed on pages 56 to 58 of the text. Additional discussions of the triple angular correlation measurement are given on page 59, and in Appendix B.

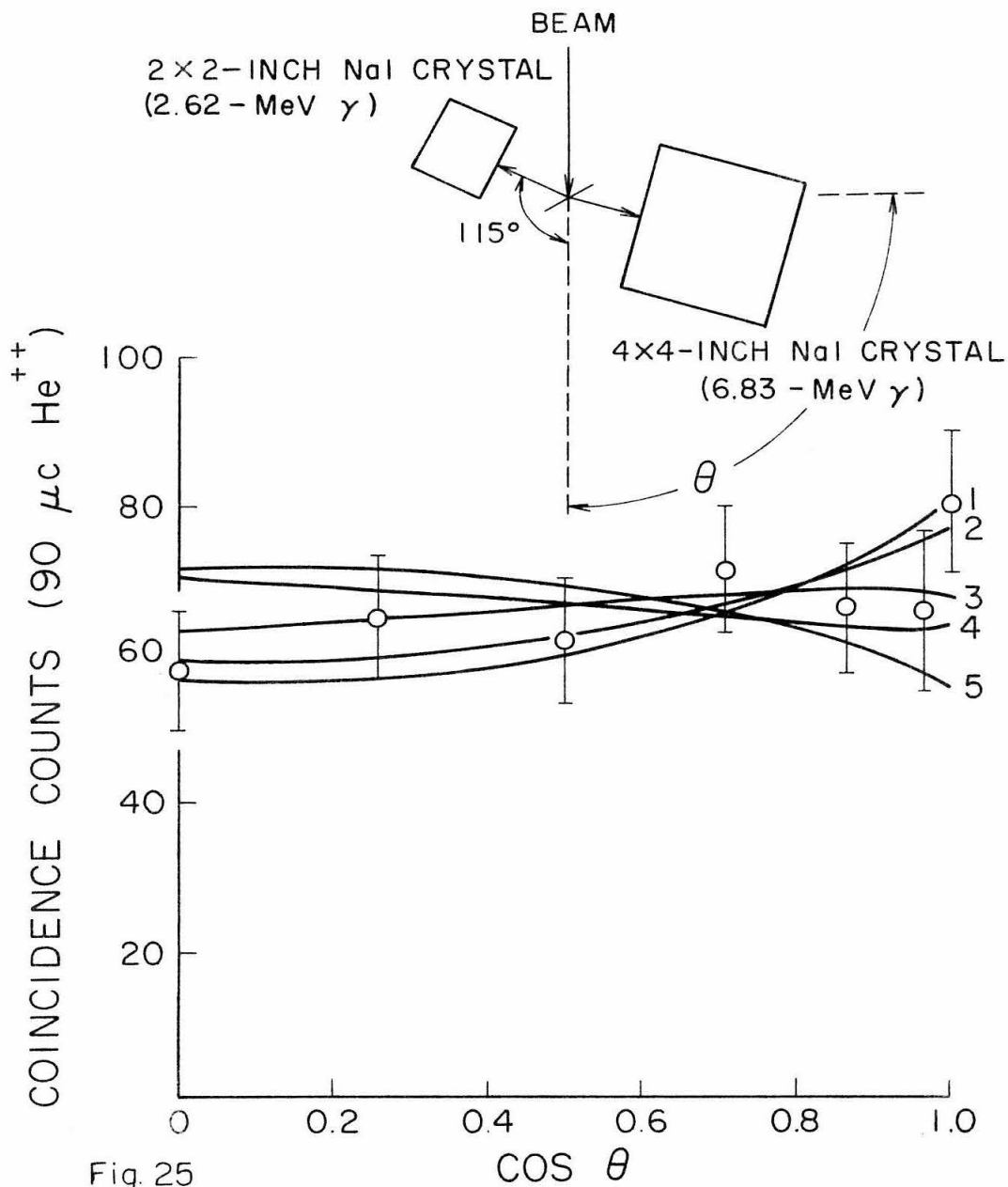


Fig. 25

Figure 26 is the excitation function for the 6.13-Mev radiation from $O^{16}(\alpha, \alpha'\gamma)O^{16}$. The ordinate N is the number of counts in the energy window, 4.91 to 6.56 Mev, for $150 \mu C$ of He^{++} . The crosses are an upper limit estimate for the contribution to the 6.13-Mev radiation from the $C^{13}(\alpha, n\gamma)O^{16}$ reaction. Additional details are given on page 75.

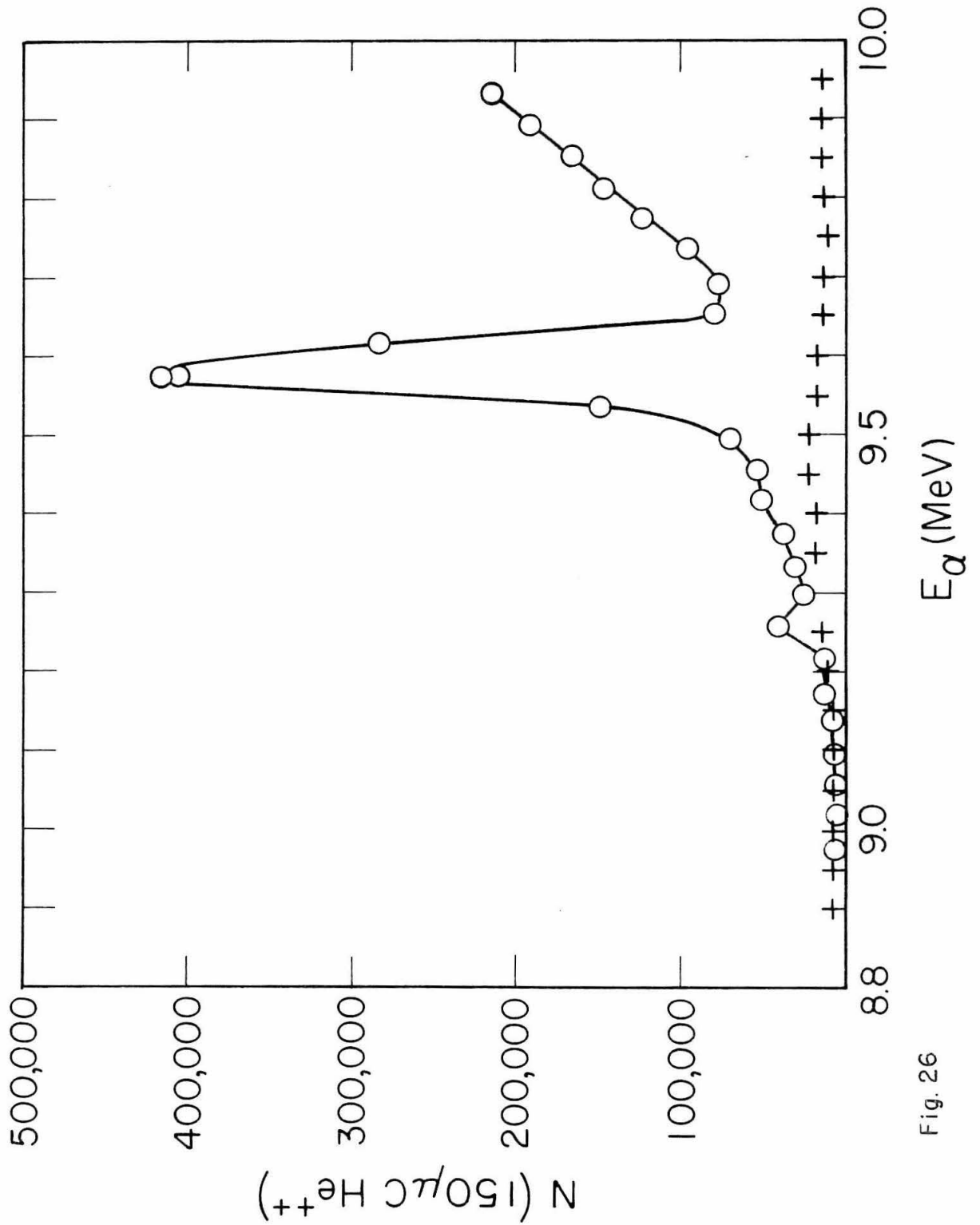


Fig. 26

Figure 27 is a comparison of the energy levels in Ne^{20} found in this experiment and the energy levels of F^{20} (19). The vertical scales, excitation energies in Mev, have been adjusted so the 10.27-Mev level in Ne^{20} and the ground state of F^{20} have the same height. Additional discussion is given on page 79 of the text.

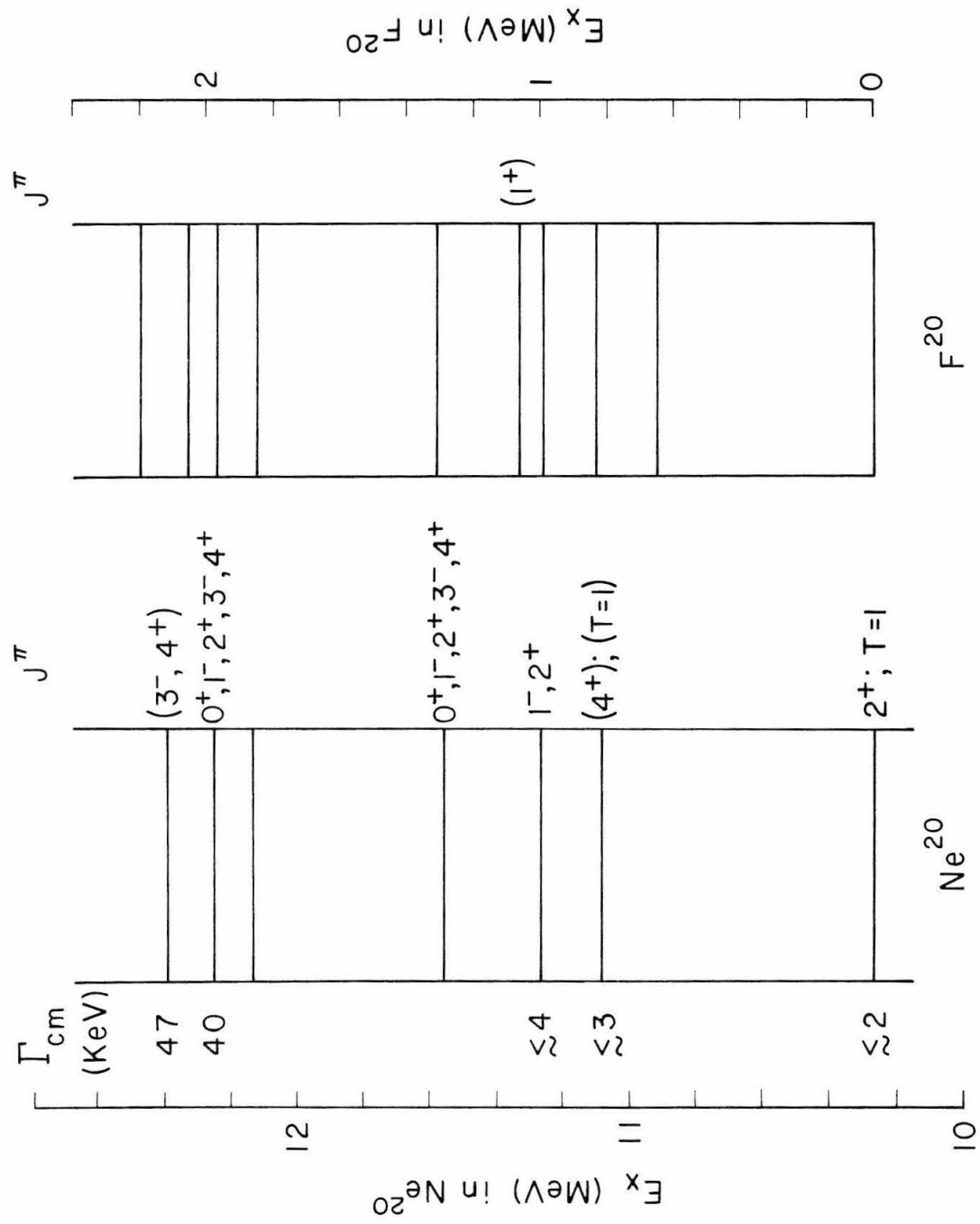


Fig. 27

Figure 28 is a section drawing of the detector geometry used for angular distribution measurements. The labelled parts are: A) beam path, B) glass walled target chamber of the clean vacuum system (top view), C) target placed at 135° with respect to the beam, D) Faraday guard ring, E) lead collimator, F) $4'' \times 4''$ NaI(Tl) crystal. Not shown are the aluminum housing for the NaI crystal, the photomultiplier, or the cylindrical lead shielding around the crystal. The scale is 1:1.

For gamma rays with energies of 8 Mev, the detection probability along path (1) is 73%, and along path (2) it is 12%, where the attenuation of 0.29 has been included for the distance travelled in the lead. This figure is discussed in Appendix A on page 92.

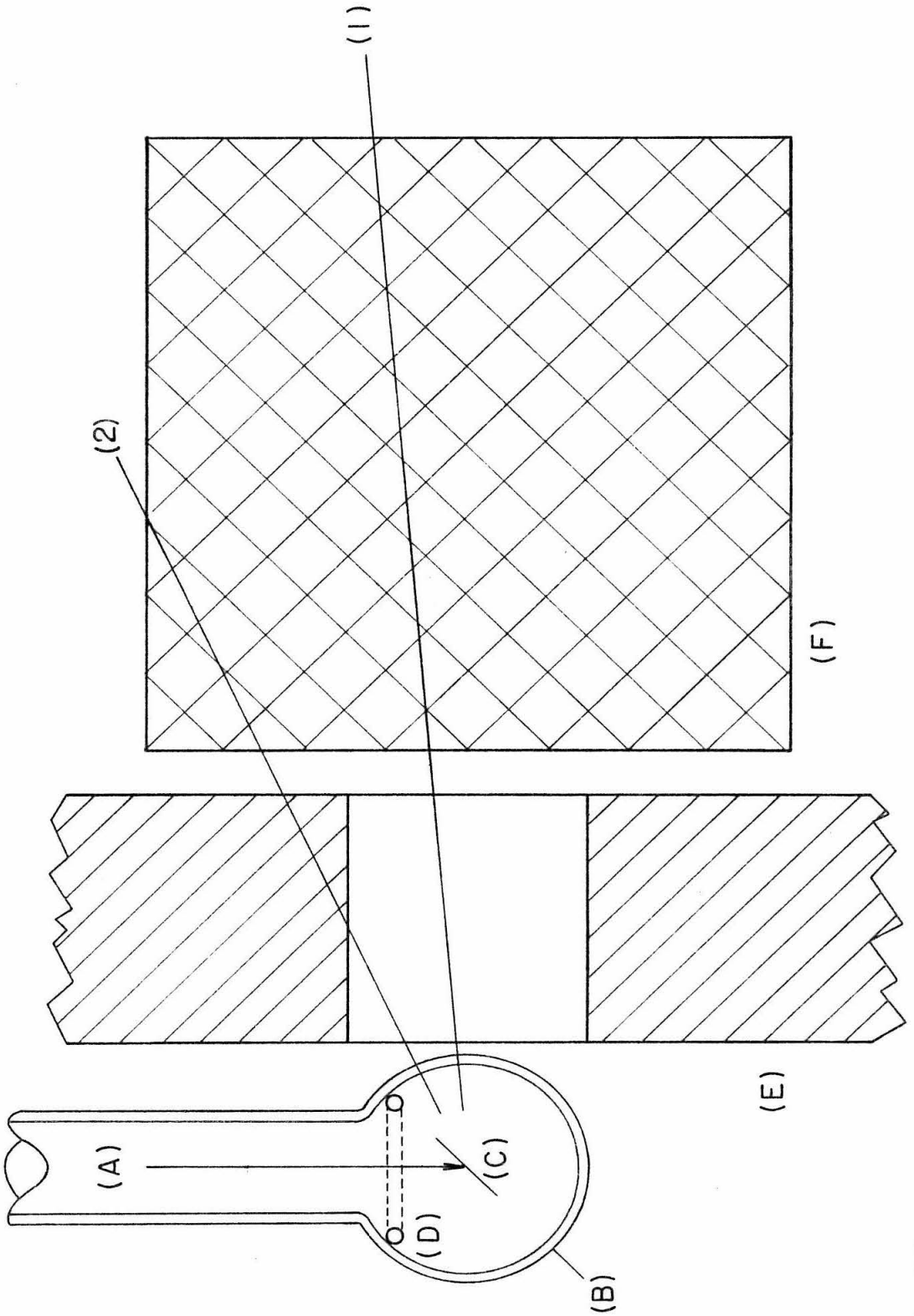


Fig. 28

Figure 29 shows the numerical results of the unified model calculation discussed in Appendix B that compares the properties of the 10.27-Mev level in Ne^{20} and the F^{20} ground state beta decay. Plotted in a, b, and c for deformation parameters $\eta = 6, 4, \text{ and } 2$, respectively, are the experimental values for the beta decay of the F^{20} ground state (β), and the M1 and E2 decay of the 10.27-Mev level of Ne^{20} . The three M1 lines, from top to bottom, are the upper limit, best value and lower limit of the experimental values. The corresponding lines for the E2 decay are marked. The ordinate, θ_i , in these plots is related to the mixture of $K = 1$ and $K = 2$ bands in the initial state (either the F^{20} ground state or the 10.27-Mev level in Ne^{20}), where $\theta_i = 0^\circ$ makes the initial state a pure $K = 2$ band, and $\theta_i = 45^\circ$ makes a 50% mixture in intensity. Similarly, the abscissa, θ_f , is related to the mixture of $K = 0$ and $K = 1$ bands in the final state (the 1.63-Mev level in Ne^{20}), where $\theta_f = 0^\circ$ makes the initial state a pure $K = 0$ band.

Figure 29d shows the level order associated with the $K = 1$ and $K = 2$ bands assumed in the initial state of Ne^{20} (or F^{20} by subtracting 10.27 Mev from the ordinate) as a function of θ_i . There are two solutions shown in this plot. For $E_{K=1}(I) < E_{K=2}(I)$, the dotted $I = 1$ solution is to be used; for $E_{K=1}(I) > E_{K=2}(I)$, the solid continuation of this line is to be used. The energy scale has been adjusted to make the lower $I = 2$ level correspond to the 10.27-Mev level.

